

A Novel Propeller Design for Micro-Swimming robot

Fei YUAN

Supervised by Dr. Mohammad S. Hasan
Staffordshire University

A thesis submitted to the Department of Computing, School of Computing
and Digital Technologies, Staffordshire University, in fulfilment of the
requirement for the degree of Doctor of Philosophy in Computing Science

Doctor of Philosophy

May 2020

I would like to dedicate this thesis to my beloved parents and my wife.

Declaration

I hereby declare that except where specific reference is made to the work of others, the work presented in this thesis is, to the best of my knowledge and belief, original and have not been submitted in whole or in part for consideration for any other degree or qualification in this, or any other university. This dissertation is my own work and contains nothing which is the outcome of work done in collaboration with others, except as specified in the text and Acknowledgement.

Fei YUAN
May 2020

Acknowledgements

I would like to convey my gratitude to the following individuals for providing me with the inspiration to embark on my PhD candidature. I was very fortunate to have three extremely good main supervisors all through my candidature. The first is Prof. Hongnian Yu, who indicates the direction of my study with his rich experiences and wisely vision. My second main supervisor is Prof. Brian Burrow, who has a deep knowledge of mathematics and give me many key advances. My third main supervisor is Dr.Mohammad Hasan, who shepherded me through the bulk of the thesis, his kind but rigorous and constant guidance gave me the motivation to perform to my maximum ability. Special gratitude goes to Dr Clare Stanier, Mr. Cathal Rogers, Mrs Tracy Windridge, for their help and precious advice.

I would like to extend my appreciation to the Staffordshire University for its generosity for granting me the ERASMUS scholarship from 2011 to 2014. I wish to express my deepest gratitude to those who support me and give me the chance to complete the thesis.

Special thanks should go to my employer, Chengdu University, and many staffs for their help and encouragement. My family members, my mother, my wonderful wife Xuelian, are mentioned last to emphasise the special nature of their tremendous encouragement, support and patience all through my candidature.

Abstract

The applications of a micro-swimming robot such as minimally invasive surgery, liquid pipeline robot etc. are widespread in recent years. The potential application fields are so inspiring, and it is becoming more and more achievable with the development of microbiology and Micro-Electro-Mechanical Systems (MEMS). The aim of this study is to improve the performance of micro-swimming robot through redesign the structure.

To achieve the aim, this study reviewed all of the modelling methods of low Reynolds number flow including Resistive-force Theory (RFT), Slender Body Theory (SBT), and Immersed Boundary Method (IBM) etc. The swimming model with these methods has been analysed. Various aspects e.g. hydrodynamic interaction, design, development, optimisation and numerical methods from the previous researches have been studied.

Based on the previous design of helix propeller for micro-swimmer, this study has proposed a novel propeller design for a micro-swimming robot which can improve the velocity with simplified propulsion structure. This design has adapted the coaxial symmetric double helix to improve the performance of propulsion and to increase stability. The central lines of two helical tails overlap completely to form a double helix structure, and its tail radial force is balanced with the same direction and can produce a stable axial motion.

The verification of this design is conducted using two case studies. The first one is a pipe inspection robot which is in mm scale and swims in high viscosity flow that satisfies the low Reynolds number flow condition. Both simulation and experiment analysis are conducted for this case study. A cross-development method is adopted for the simulation analysis and prototype development. The experiment conditions are set up based on the simulation conditions. The conclusion from the analysis of simulation results gives suggestions to improve design and fabrication for the prototype. Some five revisions of simulation and four revisions of the prototype have been completed. The second case study is the human blood vessel robot. For the limitations of fabrication technology, only simulation is conducted, and the result is compared with previous researches. The results show that the proposed propeller design can improve velocity performance significantly.

The main outcomes of this study are the design of a micro-swimming robot with higher velocity performance and the validation from both simulation and experiment.

Keywords: low Reynolds number flow, pipe inspection robot, hydrodynamic simulation, micro swimming-robot, symmetric double helix

List of publications in the thesis

- Patent authorised: The propeller for micro-swimming robot, ID: CN105193507A,
- F. Yuan, M. S. Hasan, and H. Yu, Design and Modelling of a Micro Swimming Robot, in the International Conference on Advanced Mechatronic Systems (ICAMechS2019), Kusatsu, Shiga, Japan, 2019, pp. 384389
- Tang, Jinfang, Shih-sen Chang, and Fei Yuan. "A strong convergence theorem for equilibrium problems and split feasibility problems in Hilbert spaces." *Fixed Point Theory and Applications* 2014.1 (2014): 1-16.
- F.Yuan, H. Yu and B. Burrows, "A review of methods for hydrodynamic analysis of helical swimming flagella," 18th International Conference on Automation and Computing (ICAC), Loughborough, 2012, pp. 1-8.

Table of contents

List of publications in the thesis	xi
List of figures	xvii
List of tables	xxi
1 Introduction	1
1.1 Background	2
1.1.1 Key issues in micro-swimming robot development	4
1.1.2 Theory Background	5
1.2 Motivation	7
1.3 Research aim and Objective	10
1.3.1 Problem statement	10
1.3.2 Research aim	10
1.3.3 Research objectives	11
1.4 Resources	11
1.4.1 Hardware	11
1.4.2 Software	11
1.4.3 Experiment facilities	12
1.4.4 Library access	12
1.5 Research contribution & Deliverables	12
1.6 Project Plan	13
1.7 Structure of the Thesis	13
2 Literature Review	17
2.1 Introduction	17
2.2 Classical Works	17
2.3 Modelling methods of low Reynolds number flow	19
2.3.1 Rigid body motion)	20
2.3.2 Singular point force solution	20

2.3.3	Resistive-Force Theory (RFT)	21
2.3.4	Slender-body Theory (SBT)	22
2.3.5	Immersed Boundary Method (IBM)	22
2.3.6	Boundary Element Method (BEM)	23
2.3.7	Method of Regularised Stokeslets (MRS)	24
2.4	Swimming model in low Reynolds number	26
2.4.1	Helical flagellum micro-swimmer model with RFT	27
2.4.2	Helical flagellum micro-swimmer model with RSM	28
2.4.3	Helical flagellum micro-swimmer model with IBM	29
2.5	Hydrodynamic interaction in low Reynolds number flow	30
2.5.1	Interactions between micro-swimmers and flagella	30
2.5.2	Interactions between swimmers and boundaries	31
2.6	Micro swimmer analysis, design and optimisation	32
2.6.1	Analysis	32
2.6.2	Design and optimisation	33
2.7	Development of swimming micro-robots	36
2.7.1	Shape memory alloy drive swimming robot	36
2.7.2	Giant magnetostrictive material driven vibrating swimming robot	37
2.7.3	Ferromagnetic polymer driven swimming robot	38
2.7.4	Piezoelectric material components drive swimming robots	38
2.7.5	Ionic polymer metal composites (IPMC)	40
2.7.6	Other types of swimming robots	41
2.8	Numerical methods	41
2.8.1	Computational Fluid Dynamic (CFD)	42
2.8.2	Components of CFD software	45
2.9	Summary	46
3	Design and Modelling of Artificial Micro-Swimmer	47
3.1	Introduction	47
3.2	Design and Modelling of a Rigid Flagellum	47
3.2.1	Design of a rigid flagellum	47
3.2.2	Modelling of a rigid flagellum	48
3.3	Design and Modelling of a Single Rigid Flagellum with a body	49
3.3.1	Design of a single rigid flagellum with a body	49
3.3.2	Modelling of a single rigid flagellum with a body	50
3.4	Design and Modelling of Double rigid Flagella with a body	52
3.4.1	Design of double rigid flagella with a body	52
3.4.2	Modelling of double rigid flagella with a body	52

3.5	Shape Optimisation	53
3.5.1	Flagellum Shape optimisation	53
3.5.2	Body Shape Optimisation	57
3.6	Summary	60
4	Simulation and Analysis	61
4.1	Introduction	61
4.2	Simulation Case 1-Pipe Inspection Robot	63
4.2.1	Problem Identification	64
4.2.2	Pre-processing	66
4.2.3	Solve	69
4.2.4	Post processing	72
4.2.5	Results and analysis	76
4.2.6	Optimisation Based on Simulation Results	78
4.3	Simulation case 2-human blood vessel robot	83
4.3.1	Hydrodynamic analysis of blood vessels	83
4.3.2	Problem Identification	86
4.3.3	Pre-processing	87
4.3.4	Solve	88
4.3.5	Post processing	90
4.3.6	Analysis	93
4.4	Summary	96
5	Experiments and Analysis	97
5.1	Introduction	97
5.2	Prototype design and fabrication	98
5.2.1	Prototype Design	98
5.2.2	Prototype fabrication	98
5.3	Experiment Facilities	102
5.3.1	Experiment Platform	102
5.3.2	Measuring Device	103
5.4	Experiment scheme, results and analysis	106
5.4.1	Experiment scheme	106
5.4.2	Experiment results	108
5.4.3	Experiment results comparison with numerical simulation	109
5.5	Summary	112

6 Conclusion and Future Work	113
6.1 Main work of this thesis	113
6.2 Future Works	114
References	117
Appendix A Physical properties of prototype's material	135
A.1 DSM Somos Resin Properties	135
A.1.1 Description	135
A.1.2 Applications	135

List of figures

1.1	Micro Swimmers Brennen and Winet (1977)	8
1.2	Biomedical microrobotics applications Nelson et al. (2010)	9
1.3	Research Framework for the thesis	14
2.1	Swimming model Categories	26
2.2	Swimming model with RFT Behkam and Sitti (2006)	27
2.3	Swimming model with RSM Flores et al. (2005)	29
2.4	Swimming model with IBM Hsu and Dillon (2009)	30
2.5	Purcell's three-link swimmer Purcell (1997)	33
2.6	travelling waves swimmer Kósa et al. (2006)	35
2.7	Shape memory alloy propeller Webb et al. (2000)	37
2.8	Giant magnetostrictive robot Ishiyama et al. (2002)	38
2.9	Micro-swimming robot with Ferromagnetic polymer propeller Ogrin et al. (2008)	39
2.10	Piezoelectric material propeller Sayar and Farouk (2011)	39
2.11	Fish-like robot use IPMC propeller Guo et al. (2006)	40
2.12	IPMC swimmer	41
2.13	Helical head driven by external magnetic field Okada et al. (2011)	41
3.1	Rigid Tail model	48
3.2	Tail model with body	50
3.3	Design 3 Double-tails with body	52
3.4	Junction part structure design	53
3.5	Flagellum shape	54
3.6	Relationship between velocity and filament radius	55
3.7	Relationship between velocity and helix amplitude	56
3.8	Relationship between velocity and wave number	56
3.9	Relationship between velocity and wave length	57
3.10	Changing of viscous resistance force coefficients depend on short axis	59
3.11	Changing of viscous resistance torque coefficients depend on short axis	59

4.1	The framework of FSI method using ANSYS	62
4.2	Cross Development method for FSI using ANSYS	64
4.3	Case1-Domain identification	66
4.4	Case1-Geometry of robot	67
4.5	Case1-Meshing	68
4.6	Case1-Meshing of Body	68
4.7	Case1-Meshing of tails	69
4.8	Case1-Contours of Pressure	72
4.9	Case1-Contours of Density	73
4.10	Case1-Contours of Kinetic Energy	73
4.11	Case1-Velocity Vector 1	74
4.12	Case1-Velocity Vector 2	75
4.13	Case1-Velocity Vector 3	75
4.14	Case1-Velocity Vector 4	76
4.15	The relationship between velocity and density	77
4.16	The relationship between velocity and viscosity	77
4.17	The relationship between velocity and Body-size	78
4.18	optimised Model	79
4.19	The right-side view of the optimised Model	80
4.20	The proportion of the optimised model and Pipe	80
4.21	The optimised Mesh in Pipe	80
4.22	v-t curve for the optimised model	82
4.23	The relationship between velocity and rotation speed for optimised model	82
4.24	Human blood circulation system	83
4.25	Human Heart Diagram	85
4.26	schematic diagram of inlet length	86
4.27	Physical appearance and meshing	88
4.28	Case2- velocity vector	91
4.29	Flow lines around the swimmer	91
4.30	Flow field vectors around body	92
4.31	Flow field vectors around flagella	92
4.32	thrust force vs. tails diameter	94
4.33	thrust force vs. tails diameter Comparison	94
4.34	relationship between parasitic drag and wet surface area	95
5.1	Prototype structure	98
5.2	The Optimised structure	98
5.3	The length of the DC Motor	99

5.4	The Diameter of the DC Motor	99
5.5	Wireless control chip compare to coin	100
5.6	The length of the original tails	101
5.7	The diameter of the original tails	101
5.8	The oil tank for the experiment	102
5.9	The PMMA pipe	103
5.10	Infrared radiation device	104
5.11	Measurement device structure	105
5.12	The single tail robot	106
5.13	The structure of double tails optimised	107
5.14	The experimental set-up	107
5.15	v-t curve of double tails original, optimised and single tail robot	108
5.16	The robot velocity change with tail rotative velocity	109
5.17	V-t curve comparison between simulation and experiment for the double tail optimised robot	110
5.18	Velocity to rotative velocity comparison between simulation and experiment	111

List of tables

2.1	Previous works	19
2.2	Softwares & tools	44
3.1	Parameters in Rigid Flagellum Design	48
4.1	Case1-Silicon Oil selection	71
4.2	The reference of human vessel diameter and cross section area	84
4.3	The relation of this research to existing work on human blood-vessel robots	96
5.1	Key features of the chosen motor	100
5.2	Tails Dimensions	102
5.3	Experiment results of different tail design	109
A.1	Physical properties of DSM Somos	136
A.2	Mechanical Properties of DSM Somos	136

Chapter 1

Introduction

Since the invention of industrial robots, the types of robots have been increasing, performance has been improved, and the fields of work have been expanding. The applications of the robot spread from the deep sea to the universe; especially in a variety of extreme environments where a human cannot access.

In the recent several decades, robotics research has begun to enter new fields of developments: giant systems (such as fully autonomous control of high artificial intelligence unmanned aerospace station) and micro-systems. Micro-robot generally refers to the small size of the robot, as well as small workload of the robot. With the development of Micro-Electro-Mechanical Systems (MEMS) science and technology, micro-robot research has a wide range of application prospects and social needs, including in biomedical([Fusco et al. \(2015\)](#)), aerospace([Yang et al. \(2015\)](#)), defence, industry([Terzopoulou et al. \(2019\)](#)), agriculture([Burri et al. \(2019\)](#),[Läubli et al. \(2019\)](#)), medical care([Lee et al. \(2018\)](#)) etc. One kind of micro-robot is micro-swimming robot. A micro-swimming robot is a microrobot that is propelled by swimming to move in a liquid environment. This kind of mobile micro-robot can enter a variety of liquid and space which is too small to work and explore for human beings. Other application includes micro-satellite, micro-inertial navigation device, micro-instrument, distributed battlefield sensor network, the robot under narrow space and special operating conditions, car driving and security systems, agricultural genetic engineering, biochemical sensors and so on.

The pipeline micro-robot has become a popular research topic in research of micro-robot based on swimming mode. This kind of micro-robots includes industrial piping micro-robots and medical human micro-robots.

Industrial piping micro-robots carry sensors and manipulators, go into the hazardous areas of non-removable piping systems, such as space shuttles, missiles, nuclear power plants, or industrial micro-channels of other complex systems, to perform an inspection, repair tasks for cable routing and micro-cracks etc.

With the micro-robot further miniaturisation, it can also be applied to the human body organs and blood vessels, such as [Özkale et al. \(2019\)](#), for detection of lesions, clear blood vessels, drug delivery([Hassanzadeh et al. \(2019\)](#)), even some surgery. There are two conditions need to be satisfied to fabricate a realistic swimming micro-robot. Firstly, energy should be transferred into a mechanical body to propel the robot. Secondly, the propeller should not perform a time-reversible motion. Viscosity dominates the fluid dynamics at the micrometre scale. This fact is discovered by the 'Scallop theory condition', it can only get a back and forward movement and always stay in original place whatever the oar is moving fast or slow, the flow is time-reversible. This described by [Purcell \(1977\)](#) as the scallop theorem. Although [Qiu et al. \(2014\)](#) found a swimmer can swimming by reciprocal motion, the scallop theorem still plays as an important role in low Reynolds number swimming.

Many people like [Wu \(1977\)](#) [Pedley \(1992\)](#) [Swan et al. \(2011\)](#) discussed the hydrodynamic at low Reynolds number.

1.1 Background

At the current stage, the typical micro-swimming robot application includes minimally invasive surgery robot and liquid pipeline robot.

Minimally invasive surgery currently includes endoscopic surgery and intervention. Endoscopy is an optical instrument, through the human body's natural cavity to check ([Edelmann et al. \(2018\)](#)), endoscopic surgery that is under the endoscope imaging through the minimally invasive channel into the human body([Park et al. \(2007\)](#)). Interventional surgery is not open the case of exposure to the lesion in the blood vessels, the skin of few millimetres diameter of the tiny channel, or by the original body of the pipeline, in the imaging equipment (angiography machine, perspective machine, Computer Tomography (CT), Magnetic Resonance (MR) etc. under the guidance of the local surgery on the lesion([Ullrich et al. \(2018\)](#)). When compared with traditional "open" surgery, minimally invasive surgery offers less trauma, rapid postoperative recovery, safety and fewer complications.

For conventional endoscope systems, endoscopic catheters rely on the insertion of a human hand, making the catheter susceptible to damage to the soft tissue of the human body, causing great pain to the patient, especially when the catheter is effectively inserted for a long time or in a complicated shape. Moreover, it is difficult for an endoscope to penetrate a closed space in the body, so it is often difficult to achieve effective diagnosis and treatment([Eckl et al. \(2010\)](#)).

Interventional surgery is divided into non-vascular intervention and vascular intervention surgery. There are some drawbacks to the intervention: doctors have long exposures to X-ray environments, the body experiences damages; the existing intervention surgery methods and skills are demanding and it has a high risk, the surgeon needs a long time training to limit the rapid and extensive application of the technology. At the same time, involved in the operation of the complex process, doctors fatigue, instability and other factors will affect the quality of surgery, thus affecting the quality of life of patients(Daneshmand et al. (2017)).

Medical micro-pipe robot technology is a new type of cross-research field integrating medicine, mechanics, electrical science, mechanics, materials science, computer science, mathematical analysis and so on. Therefore, it has important research value and has wide application prospects.

The design of a micro-pipe robot used in industrial fine pipelines and human luminal tubing must first be considered: the maximum diameter of the robot should be less than the minimum diameter of the operating environment. In general, the diameter of the small intestine is 15mm-40mm, the diameter of the urethra is 5mm-7mm, the diameter of the aorta is 15mm, the diameter of the vein is 5mm, etc.

The working stroke of the micro-pipe robot system must ensure that the farthest working position. For example, a robot working in the urethra is required to reach more than 22cm in the working process. The robot working in a small intestine must reach more than 5m. In the blood vessels, the work of the trip will take longer. The working stroke of the robot system directly affects the design and selection of the micro-pipe robot system energy supply scheme.

The liquid in industrial small pipelines and human lumen pipeline are also issues that must be considered in the design process of micro-pipe robots. The medium in the heat exchanger tube of a nuclear power plant is a radioactive coolant, and there is usually a certain amount of mucus in the human lumen. For example, there is a certain amount of intestinal fluid in the intestine, which is small and has no significant flow. In the arteries, blood flows faster and in the vein, blood flow is more stable and slower. This will affect the design and selection of the pipeline robot driver program.

Besides, the bio-compatibility of the outer material of the robotic system must meet the requirements of clinical application because the medical micro-duct robots used in the examination or treatment of human luminal vessels should be in contact with the human lumen wall. At the same time due to disinfection and other processes on the internal components of the robot system, the robot structure design must consider the sealing performance requirements.

1.1.1 Key issues in micro-swimming robot development

The definition of a micro-swimming robot contains at least two levels of connotation: Firstly, the size of such robots is at the micrometre level. Therefore, the swimming environment of the robot is a low Reynolds number fluid. If a scale-up study is required, the environment needs to be set to a corresponding viscous fluid to meet the conditions of a low Reynolds number fluid. Secondly, this type of robot is to work in a liquid environment, and the propulsion method is swimming propulsion instead of crawling, creeping, etc.

Energy supply

Robot energy supply is divided into two ways: wired and wireless supply. For wired or cable, power and control are more convenient, but seriously affect the flexibility of its movement, and even some locations cannot be reached, while the robot carrying the cable is also easy to damage the work of the pipeline wall. Therefore, development of a wireless robot is the main direction of current and future requirements. The wireless approach relies on carrying micro-batteries or external magnetic fields, microwave and other transmission energy(Rosen et al. (2011)). Therefore, the future development of large-capacity micro-battery is very important for micro-robots to meet the energy supply and wireless control.

Drive mode and miniaturisation

The robot's drive can be divided into the motor drive, air pressure drive, Shape Memory Alloy (SMA) drive(Wang et al. (2008)), Ionic polymer-metal composites (IPMC) drive(Ye et al. (2009)), piezoelectric drive, microwave drive, electromagnetic drive, phase change drive. Developed a large output, fast response, non-contact drive and easy the miniaturisation of the drive is the future direction of development.

Movement mode

Many micro-robot relies on legs, wheel and other structures for movement(Shi et al. (2013)). However, these components can cause damage to the inner wall if they work in a pipeline. Swimming mode and spiral way make the robot body stay uncontacted with the pipe wall and is the ideal way of movement.

Precise positioning and intelligent control

It is very difficult to realise the real-time detection of the robot in the dynamic and closed environment of the human body. It is very important to develop the micro-vision system,

improve the image processing speed, provide the detection technology and establish the microscopic liquid model to realise the intelligent control and precise positioning of the robot(Baranes and Oudeyer (2013)).

Security and noninvasive

As the robot is working in the human body, its reliability, safety and noninvasive nature are very important. It must avoid situations where it is stuck in a narrow cavity, the robot shell material is leaking inside of a patient, the robot causing human cavity wall injury etc(Tottori and Nelson (2018)).

The functions

A micro-pipe robot used in the field of industry not only has the function of detection but also can clean up the working pipeline. The micro-robot which is mainly applied in the medical field has the function of inspection inside a human body. To satisfy the future non-invasive or minimally invasive surgery needs, the development of a multi-functional robot, such as fixed-point administration, clear cleaning, sampling and implementation of surgery and other functions are needed(Menciassi et al. (2011)).

1.1.2 Theory Background

In this section, the basic rule at low Reynolds number flow is discussed in detail. Based on the discussion, the modelling approaches are discussed in Chapter 3.

Firstly, Navier-Stokes equation (N-S equation) for incompressible Newtonian fluids ($\nabla \cdot u = 0$) is given by Eq. (1.1)

$$\nabla p = \mu \nabla^2 u - \rho \left(\frac{\partial u}{\partial t} + (u \cdot \nabla) u \right) \quad (1.1)$$

where p is the fluid pressure, μ is the fluid viscosity, ρ is the fluid density (inertial force multiplier) and u is the velocity of the flow. To solve the force distribution on an object, it needs to solve for the flow field velocity u and pressure p in the surrounding fluid.

It is necessary to introduce a new intuition about the forces and effects of physics at the micro-scale. In the field of fluid mechanics, the dimensionless Reynolds number plays an important role in characterising the flow regime. It is used to define the transition from one flow regime to the other. The general attributions of flow at low Reynolds numbers can

be found in [Sleigh et al. \(1988\)](#) [Kim \(1991\)](#) [Leal \(2007\)](#) [Pozrikidis \(2011\)](#). The Reynolds number can make Navier-Stokes equation dimensionless, which is defined by Eq. (1.2)

$$Re = \frac{\rho LU}{\mu} \sim \frac{\text{inertial forces}}{\text{viscous forces}} \quad (1.2)$$

where L and U represent the characteristic length and velocity, respectively, for a given problem. For micro-robots or microorganisms, the characteristic lengths and velocities are very small, meaning that the inertial term in the Navier-Stokes equation becomes negligible. The resulting equation governing low Reynolds number flow becomes Eq. (1.3) and Eq. (1.4).

$$\nabla p = \mu \nabla^2 u + f \quad (1.3)$$

$$\nabla \cdot u = 0 \quad (1.4)$$

where u is the velocity vector field, p is the pressure scalar field, μ is the dynamic viscosity, and f is the body forces acting on the fluid. This is, known as the *Stokes equation*, a simplification of the Navier-Stokes equation and is correct only for $Re = 0$. The condition is hard to achieve but fortunately, the Stokes equation can be used as an approximate solution for $Re \ll 1$. This kind of fluid is known as *Stokes flow*, other names for this kind of flow include *creeping flow* and *low Reynolds number flow*. To swimming in this kind of flow, a system must utilise multiple degrees of freedom. It is caused by three important properties of Stokes flow.

The first property is the fact that inertia is negligibly explained by [Davies \(1975\)](#). The acceleration and deceleration times of a microswimmer in Stokes flow are very short and are also generally considered negligible. Therefore, the swimmer reaches the steady-state motion almost instantaneously.

The second property is the *time reversibility*, which is illustrated in a famous experiment conducted by [Taylor \(1951\)](#). From the Stokes equation, it can be noticed that there is no time-related variable of the flow field. At high Reynolds number flow, a swimmer can generate thrust with only one degree of freedom, for example, scallop moves forward by opening and closing its shell in different speeds. The water's different momentum is based on different moving velocity. In contrast, a swimmer cannot yield net propulsion with one degree of freedom in viscous flow condition, it can only get a simple back and forward movement because the flow is time-reversible. This described by [Purcell \(1977\)](#) as the scallop theorem.

The third property is the linearity of the Stokes equations explained by [Davies \(1975\)](#), which is very important in the modelling of fluid mechanics. The superposition of sin-

gularity solutions is allowable which is the basis for most means of solving the Stokes equations.

The discussion about the hydrodynamic at low Reynolds number can also be found in many other papers by [Wu \(1977\)](#), [Pedley \(1992\)](#), [Swan et al. \(2011\)](#).

The related research of reciprocal locomotion of dense swimmers in Stokes flow show that even in the absence of fluid inertia, certain dense bodies undergoing reciprocal motion can swim, details can be found in [Gonzalez-Rodriguez and Lauga \(2009\)](#). This result demonstrating a continuous breakdown of the scallop theorem with body inertia. Reciprocal actuation does therefore lead to a significant advantage over non-motile behaviour for small organisms ([Lauga \(2011\)](#)).

Another discussion of hydrodynamic of Stokes flow is about the geometric transition in friction for flow over a bubble mattress discovered the relationship between effective friction and bubble geometry [Davis and Lauga \(2009a\)](#), [Davis and Lauga \(2009b\)](#), [Davis and Lauga \(2010\)](#).

1.2 Motivation

The motivation of the research comes from the potential application fields such as interventional surgery. Furthermore, robots cruising inside the human body can provide great help to improve people's health. This scene is not just science fiction now, the development of technology has brought the possibility of realising this dream.

The first possibility came from the development of microbiology.

It can be noted from Fig. 1.1 that there are three kinds of propulsion from the microbiology analysed by [Hancock \(1953\)](#):

- Flat wave flagella
- Helical flagella
- Cilia

These creatures provide evidence of micro swimmer existences and encourage this research to explore the methods of designing micro-swimming robot.

Secondly, the development of Micro-electromechanical systems (MEMS) technology increases the possibility of fabrication of micro-robot.

MEMS is a system composed of a series of micro-electromechanical components. These micro-components include micro-sensors, micro-actuators, micro-mechanical structures, micro-power/micro-energy generators, signal processing and control circuits, and high-performance electronic integrated devices. These components provide functionality

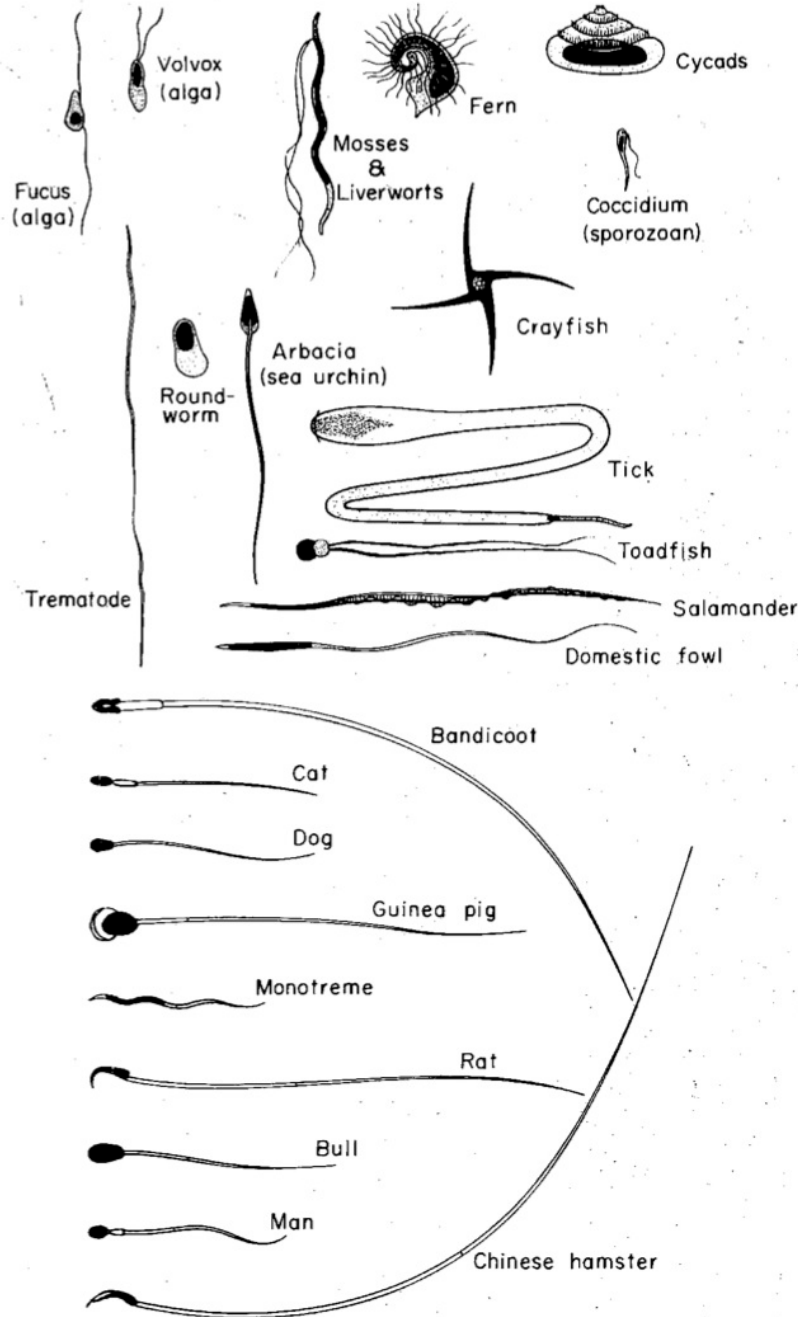


Fig. 1.1 Micro Swimmers [Brennen and Winet \(1977\)](#)

including system integration as well as interfaces and communications. The basic characteristics of MEMS include miniaturisation, versatility, high integration, suitable for mass production. The goal of MEMS technology is to explore new components and systems with new principles and new functions through system miniaturisation and integration. MEMS technology is a typical multidisciplinary approach to cutting-edge research. The MEMS technology is progressing from individual, chip-level micro-sensor and micro-actuator devices to integrated systems. The biomedical micro-robot widely developed base on MEMS technology.

As Fig. 1.2 shows, there are many applications depend on biomedical micro-robotics.

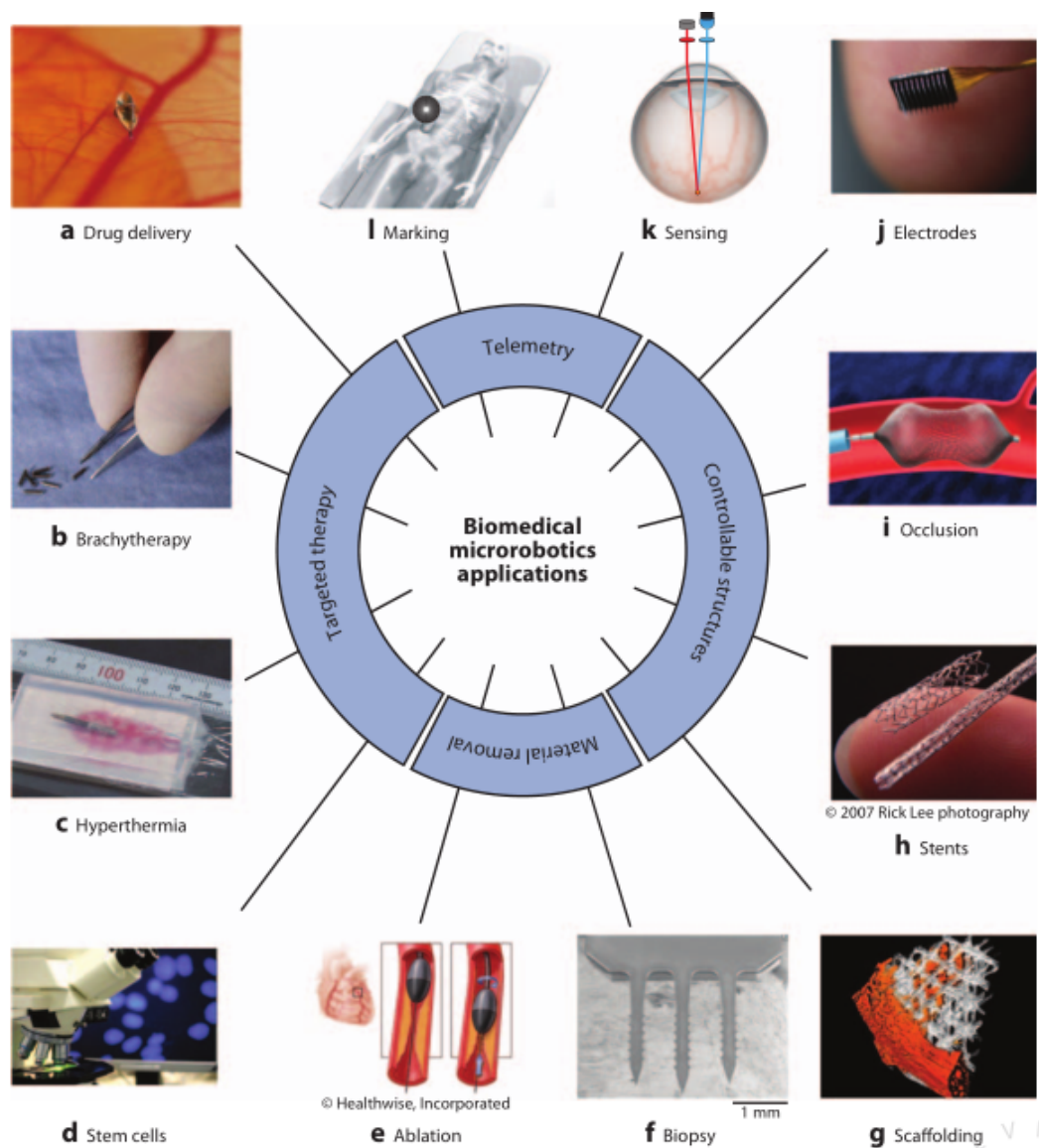


Fig. 1.2 Biomedical microrobotics applications Nelson et al. (2010)

The development of material technology also reveals a bright future for swimming micro-robots. A recent review that summarises the micro/nano application of materials such as molecular machines and nano-motors, advanced bio-sensors can be found in [Sokolov et al. \(2017\)](#).

1.3 Research aim and Objective

1.3.1 Problem statement

Except for the passive driven micro-robot such as driven by an external magnetic field, the current peristaltic and capsule robots can move due to the friction between the fuselage and the pipe wall. So that the squeeze and friction between the robot and the pipe wall cannot be avoided, those may cause damage to the pipe wall. At the same time, the flexibility and acceleration of the “screw robot” is poor, and the energy utilisation rate is low. The micro-swimming robot is separated from the pipe wall so that it does not cause damage to the pipe wall and is flexible and accelerating. However, when the robot is running in the liquid pipe, the position adjustment and the backward movement are more difficult to control. In a narrow space of pipeline, a large range of steering is difficult to achieve. The helical robot generates the driving force due to the rotation of the helical groove on the outer surface and utilises the dynamic pressure effect of the liquid in the pipeline to realise the floating operation. This avoids the contact between the robot and the pipe wall and can realise the no damage operation. But the micro-helical robot has a large volume, and the single-helix robot driven by the external magnetic field is not easy to control, and the high-speed rotation of the spiral groove on the outer surface of the robot also has the possibility of damaging the pipe wall. A micro-robot is expected to be used in human blood vessels, urethra and other fine pipelines due to its small size. One of the challenges for the micro-swimming robot is the moving performance and its efficiency. Because of the limited energy level, the micro-swimming robot needs to be highly efficient to have its extended lifetime. The structure design is very important for velocity and efficiency improvement. This research focuses on the issues of micro swimming robot structure design.

1.3.2 Research aim

This research aims to investigate and develop a swimming robot for medical or pipe inspection applications. Hydrodynamic analysis, partial differential equations and modelling, simulation technology, micro actuation, sensing and control strategies will be studied and adopted to improve the performance of the robot in different environments.

1.3.3 Research objectives

To realise the aim outlined above, this research has the following objectives:

- 1) To identify the challenges of research issues and potential application through literature review;
- 2) To propose & design a swimming robot for an application;
- 3) To model the proposed robot based on 2);
- 4) To conduct theoretical analysis;
- 5) To conduct simulation analysis;
- 4) To develop a prototype (scaled up) based on 2) & 4) & 5) to prove the concepts studied in this research;
- 8) To conduct experimental test & analysis.

1.4 Resources

The resources of this research including but not limited to:

1.4.1 Hardware

- Two standard computers with
Intel i7 processor,
8GB of RAM,
500 GB of HDD,
- High speed Internet connection 100 Mbps
- the chance to access High Performance Computing(HPC) with GPU

1.4.2 Software

- Ansys version 16,18, with components of:
Workbench,
Spaceclaim,
Meshing,
Fluent,
CFX,
- Maple version 17

1.4.3 Experiment facilities

- 3D print service from a provider
- Oil tank
- Polymethylmethacrylate(PMMA) pipe
- Speed measurement system
Infrared radiation device,
Timer,

1.4.4 Library access

- Access to on-line material e.g. IEEE, ACM etc. conference, journal papers.
- Relevant books on Fluid Dynamic, Computational Fluid Dynamic, Robotics etc. etc.

1.5 Research contribution & Deliverables

The main contributions of this research are as follows:

(1) Based on the brief introduction of micro-hydrodynamics, the five most widely theories and methods have been discussed: propulsion—slender body theory, resistance theory, immersion boundary theory, boundary element theory and method of regularised Stokes.

(2) To improve the performance of a micro-swimming robot, a novel double-helix design is proposed. The design is composed of a cone connection part and cylinder-shaped main tail part. In the same environment and robot condition, the double helix design has better stability and velocity.

(3) Based on the computational fluid dynamics, the direct motion of the proposed micro-swimming robot with the symmetrical double helix propulsion structure has been simulated by CFD analysis software ANSYS/Fluent. The numerical results show that the main factors affecting the straight-line velocity of the swimming robot are the number of the whole wave of the spiral tail, section thickness, the pitch and the cross-section width. However, it has been noted that the effect of the cross-section width is the smallest. Besides, the straight-line velocity of the robot increases linearly with the density of the liquid medium and decreases with the increase of the dynamic viscosity coefficient.

(4) Based on the experimental platform and the measurement methods, the effects of the helical tail structure parameters, the liquid parameters and the helical end kinematic parameters on the straight-line velocity of the robot are studied experimentally. The

experimental results show that the relationships between the parameters and the straight-line velocity of the robot are in good agreement with the simulation results. Beyond a certain velocity i.e. , the experimental results are different from the simulation results.

The deliverables include follows:

- Literature review on modelling methods and swimming model of low Reynolds number flow.
- Literature review on Numerical methods involved in micro-swimmer.
- An efficient design of micro-swimmer to produce higher velocity.
- A theoretical model of the proposed micro-swimming robot.
- Two groups of simulation results for each application.
- A prototype for an application.
- A group of experimental results.

1.6 Project Plan

This research conducts an investigation of existed micro-swimmers at low Reynolds number flow. Then it discusses the basic physics condition in the environment and the application domain is also identified. A novel design is proposed to pursue the maximum velocity and efficiency for the swimming-micro robot. The model of the new design is discussed. Then two cases of the simulation are conducted: one is a pipeline inspection robot that links to an experiment and the other one is blood vessel robot which is only virtual prototype i.e. simulation without realisation. Finally, the experiment of the pipeline inspection robot is committed to a real environment and prototype. The whole research framework is shown in Fig. 1.3.

1.7 Structure of the Thesis

This thesis focuses on the improvement of the performance of swimming micro-robots. The structure of the thesis is as follows:

In chapter 1, the background of this research includes key issues in micro-swimming robot development and theories, followed by motivation, aim and objectives, resources, contribution and deliverables.

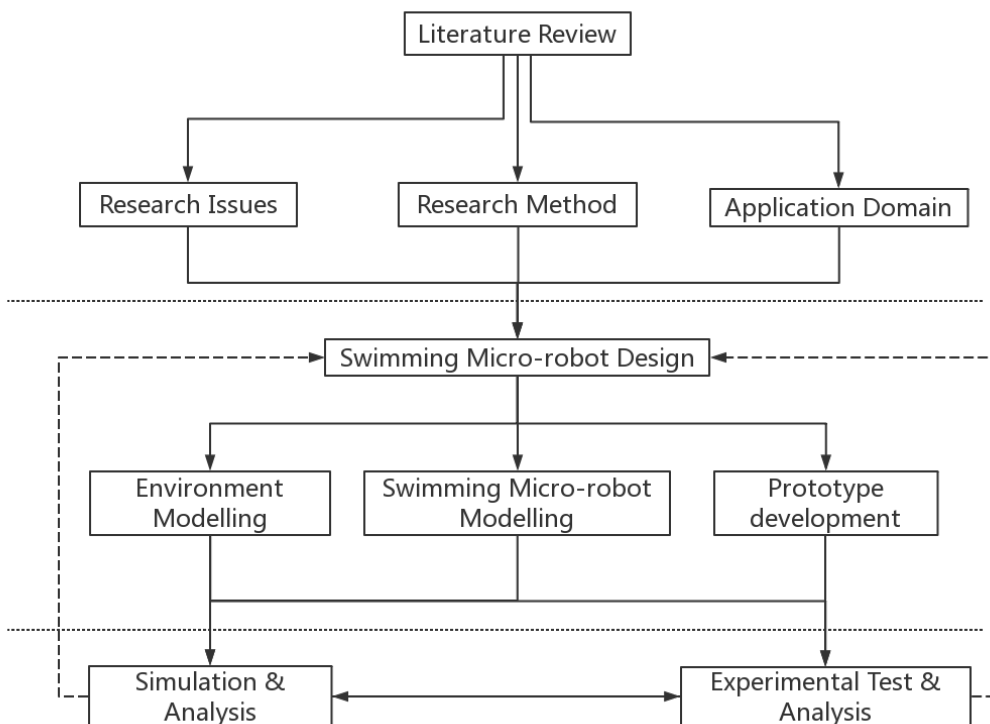


Fig. 1.3 Research Framework for the thesis

In chapter 2, related previous researches are reviewed from the classical research to the latest results. The modelling methods (including RFT, SBT, BEM, IBM, MRS) are reviewed and the swimming models based on RFT, RSM and IBM are analysed. The hydrodynamic interaction between micro-swimmers and flagella, between micro-swimmers and boundaries are reviewed. The previous researches related to analysis, design and optimisation are discussed. The existing prototypes of micro-swimming robots based on different actuators are reviewed. Finally, the numerical methods and software are summarised.

In chapter 3, a new micro swimming robot model has been proposed. The design and modelling process is presented from the simplest rigid flagellum to a design of symmetric double flagella with the body. The optimisation of shape of flagella and the body is discussed based on the design.

In chapter 4, based on the new design, simulations for two potential applications i.e. pipe inspection robot and human vessel robot are conducted. The solution of fluid-structure interaction is adopted for both cases, and cross-development method is adopted in the first case.

In chapter 5, an experiment is illustrated that includes prototype fabrication, experiment facilities and experiment results for pipe inspecting micro swimming robot. The experimental results are compared with the simulation results in chapter 4 for validation.

In chapter 6, conclusions are made for the research and the future works are proposed.

Chapter 2

Literature Review

2.1 Introduction

This chapter reviews the related topics of this research. Firstly, classical works from 1930 are briefly reviewed. The basis of low Reynolds number flow is studied in the 1970s'. Based on the principles proposed by these famous researchers, several solution theories are widely used in the computation of swimmer swimming models. This chapter reviews not only the theories but the models which utilise these theories. Furthermore, an extended topic such as hydrodynamic interaction in low Reynolds number flow is also reviewed. Then the researches about analysis, design and optimisation of swimming micro-robot are reviewed. Five driven methods for swimming micro-robot are summarised. Finally, the methods such as Finite Volume Method (FVM), Finite Difference Method (FDM) and Finite Element Method (FEM) and software such as Fluent, COMSOL, Star-CD and Open-FOAM for computational fluid dynamics are analysed at the end of this chapter.

2.2 Classical Works

Many classical reviews summarised a set of issues of swimmers from the perspective of fluid dynamics at low Reynolds number such as [Lighthill \(1975\)](#), [Lighthill \(1976\)](#), [Brennen and Winet \(1977\)](#), [Purcell \(1977\)](#) and [Yates \(1986\)](#). The research in this field started from biophysics and biology of cell motility can be found in [Holwill and Holwill \(1966\)](#), [Jahn and Votta \(1972\)](#) and [Blum and Lubliner \(1973\)](#). Many previous studies of cell motility in viscous fluids were found in the last 80 years. [Ludwig \(1930\)](#) figured out that a microorganism waved rigid arms like oars could not achieve a net motion.

[Parker \(1911\)](#) experimental studies analysed the movement of several swimmers from nature. After that, [Taylor \(1951\)](#) followed Gray's research by analysing the swimming of

organisms using small amplitude motion swimming in Stokes flow and compared his data with Gray's experimental results.

Hancock (1953) created a high-amplitude flagellum model that uses the distribution of Stokes and dipoles along the centerline to represent the velocity of the flagella. Gray et al. (1955) developed a simplified resistance theory (RFT) to derive expressions of sperm propulsion speed.

The integral of the coefficients gave the flagellation propulsion and torque that allowed the propulsion rate to be calculated.

Batchelor (1970) proposed an improved Slender-body theory (SBT) for particles of arbitrary cross-section in Stokes flow. This model was used by many researchers in studying flagella propulsion.

Lighthill (1976) and Brennen and Winet (1977) thoroughly reviewed these SBT and RFT approaches, and Johnson and Brokaw (1979) investigated and compared the distinctions between (RFT) and (SBT) on forces, bending and shear moments. They found agreement of the two theories on energy expenditure estimates by increasing the Gray and Hancock (RFT) drag coefficients.

Wu (1961) studied the two-dimensional potential flow on a finite string wave plate. The thrust, the required power and the energy imparted to the wake are calculated by applying the general theory of the oscillating deformable airfoil, and the propulsion efficiency is also evaluated.

Machin et al. (1958) and Brokaw and Brokaw (1965) investigated the propagation of spermatozoa bending waves in the sinusoidal and non-sinusoidal form for free-swimming organisms.

Peskin (1972) studied that the flow of a viscous incompressible fluid contains a region immersed in the boundary that moves with the fluid and exerts pressure on the fluid.

Higdon and Higdon (1979) proposes an improved SBT that incorporates a flagellum image system inside the spherical cell head. This precise method explains the dynamic interaction of the gyro between the head and the flagella, which is not the RFT. Explained. Higdon et al. (1979) also studied the fluid dynamics of microbial swimming using Stokeslets, dipoles and rotlets to represent the cell body, and applied slender body theory to represent flagellum with a set of Stokeslets and dipoles.

In the experimental inspection, Berg and Anderson (1973) viewed bacteria with their flagella by high-speed cinematography and showed existing evidence favoured a model in which each filament rotated.

The main achievements in previous works are summarised in Table. 2.1

Table 2.1 Previous works

Researcher(s) & years	Key Contributions
Ludwig (1930)	A microorganism is incapable move forward with waving rigid arms;
Parker (1911)	Experimental study;
Taylor (1951)	Swimming sheet analysis in low Reynolds number flow;
Hancock (1953)	High amplitude model for flagellum velocity represented by Stokeslets and dipoles distribution ;
Gray et al. (1955)	Resistive force theory;
Wu (1961)	Swimming of a waving plate;
Cox (1971)	Slender-body theory;
Blake (1971)	Spherical envelope approach to cilia propulsion;
Peskin (1972)	A numerical method of flow patterns around heart valves;
Berg (1974)	Flagella inspection;
Purcell (1977)	Scallop theorem, Purcell swimmer ;
Block et al. (1989)	Optical tweezers measure method ;
Cortez (2001)	The Method of Regularised Stokeslets ;
Peskin (2002)	The immersed boundary method ;
Baudry et al. (2005)	A flexible flagellum made of colloidal magnetic particles linked by DNA and attached to a red blood cell;
Williams et al. (2014)	A self-propelled bio-hybrid swimmer
Qiu et al. (2014)	Swimming by reciprocal motion at low Reynolds number
Ahmed et al. (2017)	Neutrophil-inspired propulsion in a combined acoustic and magnetic field

2.3 Modelling methods of low Reynolds number flow

The topic of low Reynolds number flow modelling around objects, either stationary or moving, have been studied for many years by [Davies \(1975\)](#), [Ludwig \(1930\)](#), [Hancock \(1953\)](#), [Youngren and Acrivos \(1975\)](#), [Lauga and Powers \(2008\)](#) and [Dillon et al. \(2007\)](#). The benefit from linearity of the Stokes equation allows analytical treatment and low computational cost numerical approaches. Many researchers from a wide range of fields, including fluid mechanics, mathematics, biology and micro-robotics, have an interest in low Reynolds number modelling. In this section, a series of modelling methods are introduced followed by the relationship among them. The rigid body motion is the simplest

one and is therefore presented first. Then the Method of Fundamental Solutions (MFS), the Restrictive Force Theory (RFT), the Slender Body Theory (SBT), the Boundary Element Method (BEM) and method of regularised Stokeslets are discussed.

2.3.1 Rigid body motion)

Based on the linearity of Stokes flow, the relationships between the body's velocity U , rotational speed Ω , external force F and external torque T can be represented by a matrix equation as shown below:

$$\begin{pmatrix} F \\ T \end{pmatrix} = \begin{pmatrix} A & B \\ B^T & C \end{pmatrix} \begin{pmatrix} U \\ \Omega \end{pmatrix} \quad (2.1)$$

here A , B and C are 3×3 matrices. The matrix parameters can be decided based on the swimmer's geometric body (For et al. (2004)).

2.3.2 Singular point force solution

The Stokes equations can be solved analytically for some special types of external forces. When an external force f_s acts as a singular point force and acts on the fluid at the position x_0 , it can be presented as

$$f_s = \delta(x - x_0)b \quad (2.2)$$

where δ is the Dirac delta and b is present the direction and magnitude of the external force. The flow changed by the force and it can be computed analytically by solving the equation eq: 2.1, and the results are shown in

$$\nabla - p + \mu \nabla^2 u = -\delta(x - x_0)b \quad (2.3)$$

The resulting flow field velocity $u(x)$ is shown in

$$u_i(x) = S_{ij}(x, x_0)\dot{b}_j, S_{ij}(\hat{x}) = \frac{1}{8\pi\mu} \left(\frac{\delta_{ij}}{r} + \frac{\hat{x}_i \hat{x}_j}{r^3} \right) \quad (2.4)$$

where $\hat{x} = x - x_0$ and $r = |\hat{x}|$. The pressure field and stress tensor can be found in similar expressions. S_{ij} is known as Stokeslet (also known as Oseen-Burgers tensor), and it plays the most important role in singularity solution of the Stokes flow. A two-step approach is used for solving Stokes equation of different geometries. The first step is to determine the singularities distribution and strength to fulfil the boundary conditions. The second step is to calculate velocities at discrete field points of interest. The Stokeslets is one order singularities, through higher-order singularities have been successfully employed.

2.3.3 Resistive-Force Theory (RFT)

Resistive-force theory, also known as a kind of local drag theory, which is focus on simply the force-velocity relationship between a body and its surrounding fluid rather than calculate the flow profile. This relationship is represent by a drag coefficient.

In the classical RFT in [Hancock \(1953\)](#) and [Gray et al. \(1955\)](#), the force f applied by the flagellum on the fluid at the point where s (s is along the arc of the flagellum) is proportional to the local centerline velocity $U(s, t)$, assuming that the fluid is stationary at infinity in the coordinate frame. Separating U into components lying along with the directions normal and tangential to the body centre line, U_n, U_s respectively, there are the two corresponding components of the force/length as in

$$f_s = \mu C_s U_s, \quad f_n = \mu C_n U_n \quad (2.5)$$

It can be noted that the fluid viscosity μ has been separated and it makes the force coefficients dimensionless.

The coefficients which be used widely is proposed by Gray and Hancock (1955) [Gray et al. \(1955\)](#) for computing flagella motions as

$$C_s = \frac{2\pi}{\ln \frac{2\lambda}{r} - \frac{1}{2}}, \quad \gamma = \frac{C_n}{C_s} = 2 \quad (2.6)$$

where r is the cross-sectional radius of the flagellum and λ is the wavelength. The ratio, $\gamma = 2$, given by Gray and Hancock is only correct for the vanishing thin flagellum cases.

On the basis of Cox's results (1970) [Cox \(1971\)](#), [Brokaw\(195\)](#) [Brokaw \(1979\)](#) suggested that a more appropriate value for C_n is show in

$$C_n = \frac{4\pi}{\ln \frac{2\lambda}{r} + \frac{1}{2}} \quad (2.7)$$

which, for a sea urchin spermatozoon, should give $\gamma = 1.7$. However, the best agreement with experimental measurements was obtained when using $\gamma = 1.8$ and for this reason, this value was used in subsequent work [Brokaw \(1974\)](#). The application of this theory can be found in recent research. [Powers \(2002\)](#)

[AvronAvron et al. \(2004\)](#) introduced the notion of the swimming drag coefficient which allows for the ranking of swimmers to compare the efficiencies of different swimmers.

2.3.4 Slender-body Theory (SBT)

The objective of the slender-body theory is to take advantage of the slenderness to achieve simplifications in obtaining approximate solutions for the flow around such bodies [Brennen and Winet \(1977\)](#). The slender-body theory, pioneered by Hancock [Hancock \(1953\)](#), provides an alternative solution for the dynamics of the three-dimensional of the filament surface by that of its centre-line using an appropriate distribution of flow singularities. The development of this theory evolved through the work of Burgers [Saffman \(1956\)](#), Broersma [Broersma \(1960\)](#), Tuck [Tuck \(1964\)](#), Taylor [Taylor \(1969\)](#), Tillett [Tillett \(1970\)](#), Batchelor [Batchelor \(1970\)](#), Cox [Cox \(1971\)](#) and Blake [Blake \(1972\)](#). A simple but elegant demonstration of the low-Reynolds-number slender-body theory is given by Lighthill [Lighthill \(1975\)](#).

E. Lauga [Lauga and Powers \(2008\)](#) summarised two different approaches of Slender-body methods.

The resulting value of the velocity of the filament at $s = s_0$ is given by the integral equation

$$u(s_0) = \frac{f_{\perp}(s_0)}{4\pi\mu} + \int_{|r_0-r|>\delta} S_{ij}(r_0-r) \cdot f(s) ds \quad (2.8)$$

Further research was conducted in orientations order and dynamics in suspensions of self-locomotion slender rods [Saintillan and Shelley \(2007\)](#).

2.3.5 Immersed Boundary Method (IBM)

The immersed boundary method was proposed by Charles S. Peskin in 1972 [Peskin \(1972\)](#) [Peskin \(1977\)](#) [Peskin \(2002\)](#).

The general form of the IBM method mathematical model can be described by the following equations:

$$\rho\left(\frac{\partial u}{\partial t} + (u \cdot \nabla)u\right) + \nabla p = \mu \Delta u + f, \quad (2.9)$$

$$\nabla \cdot u = 0, \quad (2.10)$$

$$\rho(x, t) = \int M(q, r, s) \delta(x - X(q, r, s, t)) dq dr ds, \quad (2.11)$$

$$f(x, t) = \int F(q, r, s, t) \delta(x - X(q, r, s, t)) dq dr ds, \quad (2.12)$$

$$\begin{aligned} \frac{\partial X}{\partial t}(q, r, s, t) &= u(X(q, r, s, t), t) \\ &= \int u(x, t) \delta(x - X(q, r, s, t)) dx, \end{aligned} \quad (2.13)$$

$$F = -\frac{\delta E}{\delta X}. \quad (2.14)$$

In these equations, $M(q, r, s)$ is a given function which presents the Lagrangian mass density of the material, and $E[X]$ is a given function, the elastic potential energy of the material in configuration X . The notation $\delta E / \delta X$ is shorthand for the *Fréchet* derivative of E .

2.3.6 Boundary Element Method (BEM)

The Boundary Element Method (BEM) uses an integral equation over the surface of a body to solve the Stokes flow around an arbitrary geometric body. It is different from the method above which directly superposing singularities. The integral equation is given below.

$$u_j(x_s) = \int_S u_i(x) T_{ijk}(x, x_s) n_k(x) dS(x) - \int_S S_{ji}(x_s, x) f_j(x) dS(x) \quad (2.15)$$

This equation is found by using the Lorentz reciprocal theorem [Pozrikidis \(2011\)](#). S_{ij} is the Stokeslet, $f = \delta n$ is the modified boundary traction. The drag force on a body is contained in the boundary traction force f introduced in this method. Phan-Thien, Tran-Cong & Ramia [Phan-Thien et al. \(1987\)](#) introduced the boundary-element method (BEM) for flagella propulsion to account for non-spherical heads and non-slender flagella. Derivation and application of BEM can be found in literature [Pozrikidis \(2011\)](#) [Tran-Cong and Phan-Thien \(1986\)](#) [Tran-Cong and Phan-Thien \(1988\)](#) [Tran-Cong et al. \(1990\)](#) [Muldowney and Higdon \(1995\)](#) [Fujita and Kawai \(2001\)](#) [Goto et al. \(2001\)](#) [Ishikawa et al. \(2007\)](#). The recent utilisation of BEM can be found in [Smith \(2010\)](#), which applied the method to cilia and flagella driven flow.

2.3.7 Method of Regularised Stokeslets (MRS)

The equation of BEM is not valid at the point of the singularity, so special integration methods are needed to solve the equation over the surface including the singularity. One of the solutions is the method of regularised Stokeslets. Cortez [Cortez \(2001\)](#) proposed a numerical method which is based on smoothing of the forces, leading to regularised Stokeslets.

A numerical method for calculating the Stokes flow in the presence of immersion boundaries and obstacles is proposed. The method is based on the smoothing of forces to produce regularised Stokeslets. The resulting expression provides the pressure and velocity fields as a function of force. The latter expression can also be reversed to find the force that applies the given velocity boundary condition. The numerical examples given demonstrate the broad applicability of the method and its properties. When calculating the force along the smooth direction, the solution uses a second-order precision convergence.

In 2005, Cortez, Fauci and Medovikov [Cortez et al. \(2005\)](#) used the regularised Stokeslet method (RSM) as a solution for removing singularities from the Stokeslet distribution and applied it to BEM and infinitesimal flagella. Then, they proposed a three-dimensional regularised Stokeslets method, and analysed its model problem in the flow of the sphere and the accuracy and performance of the steady-state rotation of the rigid spiral tube. The author combines this method with the immersion boundary expression of the elastic helix to study the passive elastic properties of the elastic helix and the mechanism of internal force generation.

The method of regularising Stokeslets is a Lagrangian method for calculating the force-driven Stokes flow of material points distributed in a fluid. When the force is given by the cutoff function, it is based on the superposition of the exact solutions of the Stokes equation. The predicted swimming speeds of various spiral geometries were compared with experimental data of the moving spirals.

The method of regularised Stokeslets was proposed to remove singularities from distributions of Stokeslets and applied this to BEM and infinitesimally thin flagellum. It is for the computation of two- and three-dimensional Stokes flows driven by external forcing [Cortez \(2001\)](#). The solution of Stokes equations comes in the form of Stokeslets and Rotles which assumes point forces and torques as

$$U_s(x; x_0, F_0) = \frac{f_0}{8\pi r} + \frac{[f_0 \cdot (x - x_0)](x - x_0)}{8\pi r^3} \quad (2.16)$$

$$U_r(x; x_0, L_0) = \frac{L_0 \times (x - x_0)}{8\pi r^3} \quad (2.17)$$

In the above constructions, $r = \|x - x_0\|$ and f_0 and L_0 represent force and torque, respectively, applied at a point x_0 . Since it is desirable to evaluate the flow arbitrarily close to the points where the forces and torques are applied, it is clear that the above construction will lead to unacceptable singularities in the flow. The way to remove these singularities is through the introduction of a "spread" to the forces and torques applied. This spread is chosen to match the cross-sectional area of flagella.

About the cutoff function:

- (i) Should be radially symmetric;
- (ii) Defines a delta function in the limiting case as the spread goes to 0.

Cortez [Cortez \(2001\)](#) proposed a suitable cutoff function in three dimension as

$$\phi_\delta(x) = \frac{15\delta^4}{8\pi(r^2 + \delta^2)^{7/2}} \quad (2.18)$$

It shows that (i) is satisfied.

Obviously, $\lim_{\delta \rightarrow 0} \phi_\delta(0) \rightarrow \infty$ and $\int_{\mathbb{R}^3} \phi_\delta(x) dx = 1$, which shows (ii) is satisfied. Involving this cutoff function with Equ.(2.16) and Equ.(2.17) yields the regularised Stokeslet and Rotlet as:

$$U_{\delta,s}(x; x_0, f_0) = \frac{f_0(r^2 + 2\delta^2)}{8\pi(r^2 + \delta^2)^{3/2}} + \frac{[f_0 \cdot (x - x_0)](x - x_0)}{8\pi(r^2 + \delta^2)^{3/2}} \quad (2.19)$$

$$U_{\delta,r}(x; x_0, L_0) = \frac{(2r^2 + 5\delta^2)}{16\pi(r^2 + \delta^2)^{5/2}} [L_0 \times (x - x_0)] \quad (2.20)$$

For non-zero δ , the regularised Stokeslet and Rotlet remove the singularities induced in the solution of Stokes flow. As δ approaching zero, the equation towards the Stokeslet expression.

The evolution process of modelling methods for the solution of Stokes equations can be found from the above illustrations and [Smith \(2010\)](#). The traditional methods are based on the singularities theory. The important parts of these methods are the singularities points distribution and the shape mapping which make the approximation of the solution and simplified the calculation. The accuracy of the solution depends on the levels of singularities distribution and the shape mapping method. The RFT method is somewhat different than other methods which avoid the calculation of the flow profile but just simply the force-velocity relationship between a body and its surrounding fluid. The BEM method utilises an integral equation over the surface of an arbitrary geometric body. And the RSM uses a specific function to regularise the singularities (which are not included in the

solution) with the assumption of point force applied not at single points but within small spheres centred at those points. The accuracy of the solution of the equations depends on the function's design.

2.4 Swimming model in low Reynolds number

To develop an artificial swimmer, the swimming model is necessary. From the analysis of biophysics of cell motility, many swimming models at Stokes flow have been proposed [Abbott et al. \(2009\)](#). In this section, swimming models at low Reynolds number is reviewed, then the details of three models for helix flagella structures are given.

The swimming model in low Reynolds number can be classified into four categories: three-link swimmer, helix flagella, flat-wave flagella and cilia which show in [Fig. 2.1](#). A review of undulatory locomotion swimming at low Reynolds number is given in [Cohen and Boyle \(2010\)](#). For the most realistic propulsion obtained from surface deformation or elastic body, many researchers take focus on it.

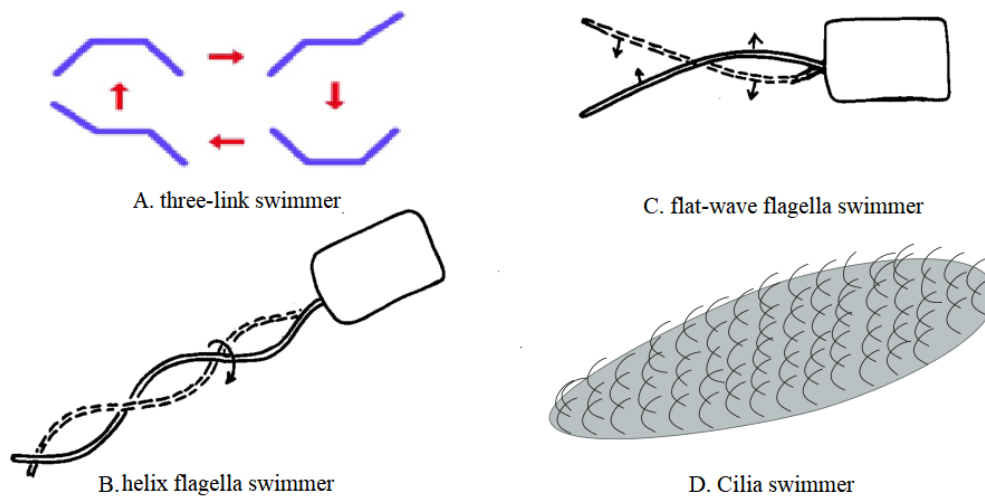


Fig. 2.1 Swimming model Categories

[Lauga \(2007c\)](#) [Lauga \(2007b\)](#) [Lauga and Davis \(2012\)](#) discussed the propulsion in a viscoelastic fluid and viscous Marangoni .

The related research including a model for dynamical coherence in thin films of self-propelled microorganisms [Aranson et al. \(2007\)](#); modelling magnetic torque and force for controlled manipulation of soft-magnetic bodies [Abbott et al. \(2007\)](#); mathematical analysis of microswimmer with bi-linear theory [Felderhof \(2006\)](#) and analytic results for the three-sphere swimmer at low Reynolds number [Ajdari et al. \(2008\)](#) [Golestanian \(2008\)](#).

The elastic rod model for anguilliform swimming [McMillen and Holmes \(2006\)](#) and the rod-shaped monotrichous bacterial model [Hsu and Dillon \(2009\)](#) were also discussed. The latest research is about the elastic rod with intrinsic curvature and twists [Olson et al. \(2013\)](#).

The detailed models are illustrated in the following sections which use RFT, RSM and IBM.

2.4.1 Helical flagellum micro-swimmer model with RFT

Behkam and Sitti [Behkam and Sitti \(2004\)](#) [Behkam and Sitti \(2005\)](#) [Behkam and Sitti \(2006\)](#) proposed two hydrodynamic models inspired by the motility mechanism of bacteria with peritrichous flagellation. Their models are based on the Resistance Force theory. The authors also fabricated a scaled-up model of the swimming robot to validate the theoretical results.

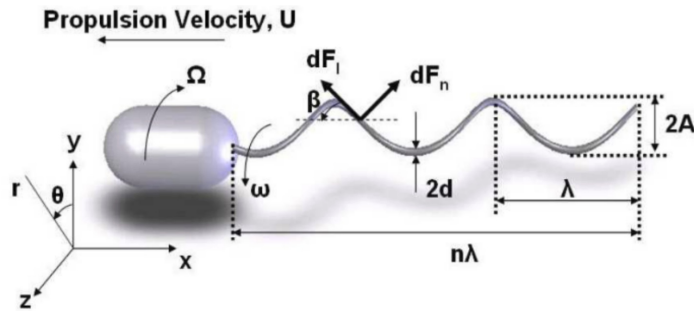


Fig. 2.2 Swimming model with RFT [Behkam and Sitti \(2006\)](#)

The parameter setting of the model can be found in Fig. 2.2.

This model is based on cylindrical coordinates. It takes the helix size and the rotation frequency as input and returns important performance parameters such as propulsion, forward speed and generated torque.

For an element ds on the helix, the Equ. (2.21) shows the propulsive force in the x -direction in terms of its normal and longitudinal components.

$$dF_x = dF_n \sin \beta - dF_l \cos \beta \quad (2.21)$$

and the force in θ - direction is:

$$dF_\theta = -(dF_n \cos \beta + dF_l \sin \beta) \quad (2.22)$$

Based on the Resistive Force theory (RFT), we have

$$dF_n = C_n(V_\theta \cos\beta - U \sin\beta) \sec\beta dx \quad (2.23)$$

$$dF_l = C_l(V_\theta \sin\beta + U \cos\beta) \sec\beta dx \quad (2.24)$$

where $V_\theta = A_{helix} \omega_{app} = A_{helix}(\Omega - \omega)$.

The velocity in x-direction of head is:

$$U = \frac{n\lambda V_\theta \sin\beta \cos\beta (C_n - C_l)}{n\lambda (C_n \sin^2\beta + C_l - C_l \sin^2\beta) + 6\pi\mu a \cos\beta} \quad (2.25)$$

this result can be compared with a different model proposed by Chen B et al. [Chen et al. \(2008\)](#) [Chen et al. \(2010\)](#) without a cell body, the maximum velocity is:

$$U = \frac{(C_l - C_n) \sin\theta \cos\theta \omega A}{C_l \cos^2\theta + C_n \sin^2\theta} \quad (2.26)$$

Many researches, such as [Rodenborn et al. \(2013\)](#), [Tabak and Yesilyurt \(2014\)](#), [Nourmohammadi and Keighobadi \(2014\)](#), utilise RFT to develop micro-swimming robot model.

[Powers \(2002\)](#) utilised resistive force theory to show that the counter-rotation of the cell body necessary for torque balance is sufficient to wrap the filaments into a bundle, even in the absence of the swirling flows produced by each individual filament.

2.4.2 Helical flagellum micro-swimmer model with RSM

The helical flagella model is proposed by Flores et al. in 2005 and is based on the method of Regularised Stokeslets [Flores et al. \(2005\)](#). The model is shown in Fig: 2.3.

Since the Stokes equation is linear, its solution can be represented as a superposition of each solution for a given Stokeslet and/or Rotlet combination, that is

$$U(x) = \sum_{i=1}^{N_r} U_{\delta,r}(x; x_i, L_i) + \sum_{j=1}^{N_s} U_{\delta,s}(x; x_j, f_j). \quad (2.27)$$

N_r and N_s represent the number of Rotlets and Stocklets, respectively.

Applying a constant motor torque at the head of the first rod activates Hooke's law forces between each pair of points connected by rigid rods (high spring constant k) obeying

$$f_{jk} = \frac{k}{L_0^{jk}} (L^{jk} - L_0^{jk}) \frac{x - x_0}{L^{jk}} \quad (2.28)$$

$$f_{kj} = -f_{jk} \quad (2.29)$$

$$L^{jk} = \|x_k - x_j\| \quad (2.30)$$

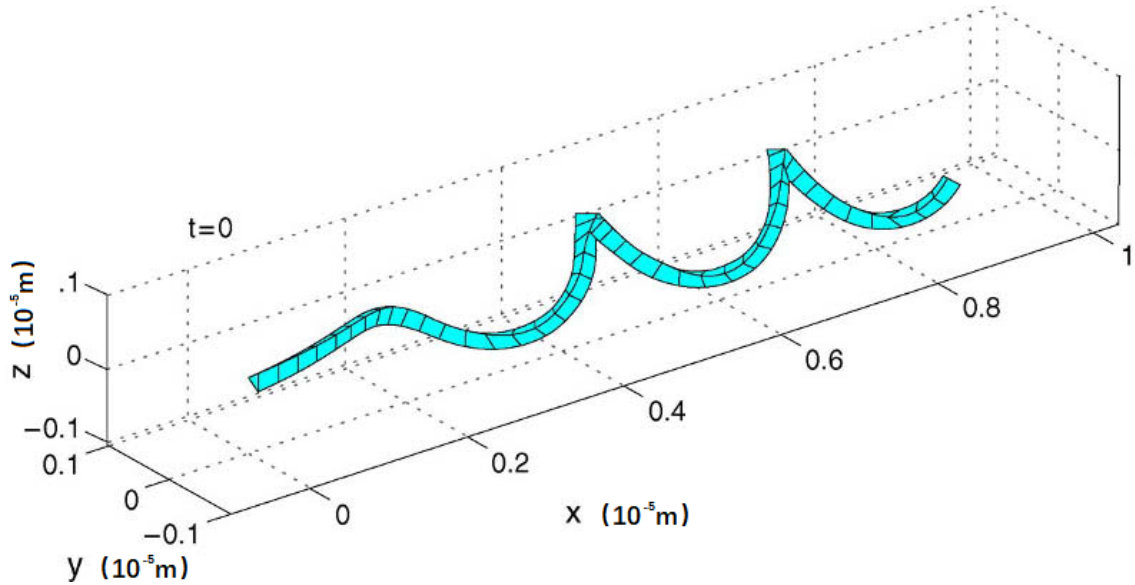


Fig. 2.3 Swimming model with RSM Flores et al. (2005)

where f_{jk} is interpreted as the force acting on the force acting on the $K^l h$ particle as a result of the j^h particle's interaction, L^{jk} is the length of the rod connecting the $k^l h$ particle to the j^h particle and L_0^j is the rest length of the rod connecting the $k_t h$ particle to the j^h particle.

For the numerical implementation of a one-motor flagellum consisting of N_s rods, the flow field can be time-evolved for any point x_k by

$$U(x_k) = \frac{dx_k}{dt} = U_{\delta,r}(x_k; x_0, L_0) + \sum_{j=1}^{N_s} U_{\delta,s}(x_k; x_j, f_{jl}) \quad (2.31)$$

With RSM, models and optimisation methods were proposed for the analysis of a micro-structure Lobaton and Bayen (2009) Bouzarth et al. (2011). Other issues on the multi-rate time integrator Bouzarth and Minion (2010) and the method of images Ainley et al. (2008) were discussed.

2.4.3 Helical flagellum micro-swimmer model with IBM

The immersed boundary method (IBM) provides a modelling framework for studying the interaction of incompressible fluid flow and immersed elastic structures. Furthermore, it gives a numerical method for computing. An application model is shown in Fig. 2.4 which is proposed by Hsu et.al Hsu and Dillon (2009).

Equ. (2.32) to Equ. (2.35) shows the general form of the IBM method model.



Fig. 2.4 Swimming model with IBM [Hsu and Dillon \(2009\)](#)

$$\rho(u_t + (u \cdot \nabla)u) = -\nabla p + \mu \Delta u + F(x, t) \quad (2.32)$$

$$\nabla \cdot u = 0 \quad (2.33)$$

$$F(x, t) = \int f(s, t) \delta(x - X(s, t)) ds \quad (2.34)$$

$$\frac{\partial X}{\partial t} = u(X(s, t), t) = \int u(x, t) \delta(x - X(s, t)) dx \quad (2.35)$$

where x and s are the Eulerian and Lagrangian variables and $\delta(x)$ is the Dirac delta function.

2.5 Hydrodynamic interaction in low Reynolds number flow

The hydrodynamic interactions in low Reynolds number flow is an extraordinary hot research topic in this field so many leading publications are available. The hydrodynamic interactions are suspected to play an important role for most of microswimmers swimming in viscous fluids affected by their companions or boundaries.

2.5.1 Interactions between micro-swimmers and flagella

Microorganisms and micro-robots swimming in viscous fluids usually swim in semi-dilution or dense cell populations. Swimming organisms produce a flow that is felt by nearby cells. These flows affect the kinetic energy of all cells [Lauga and Powers \(2008\)](#). The analyse of the fluid-dynamical interaction of pairs of two swimming cells [Ishikawa et al. \(2007\)](#) and flagella bundling [Powers \(2002\)](#) [Flores et al. \(2005\)](#) were discussed respectively. The experiments of a macro-scale model of flagella bundling [Kim et al. \(2003\)](#) have been conducted. An important particle-based numerical simulation was conducted of two locomotion artificial swimmers [Keaveny and Maxey \(2008\)](#) which is based on the micro-swimmer proposed by Dreyfus [Baudry et al. \(2005\)](#).

Pooley [Pooley et al. \(2007\)](#) investigated the hydrodynamic interactions between two micro-organisms swimming at low Reynolds number. The long-time dynamics of two hydro-dynamically-coupled swimming cells [Michelin and Lauga \(2010\)](#) and mechanics of swimming of multi-body bacterial swarms were discussed [Phuyal and Kim \(2013\)](#).

Eric Lauga [Lauga \(2007c\)](#) inspected a waving sheet of small amplitude propulsion and transport in a complex fluid [Lauga \(2007b\)](#) [Lauga \(2007a\)](#). The synchronisation problem of flexible sheets was analysed [ELFRING and LAUGA \(2011\)](#), even in two-dimensional cases [Elfring et al. \(2009\)](#) [Elfring and Lauga \(2011\)](#). A wider discussion about the cooperation of sperm in two dimensions including synchronisation, attraction, and aggregation through hydrodynamic interactions can be found in [Yang et al. \(2008\)](#).

The research of interaction between rotating flagella has a long history. From 70's the bundle of helical geometry attracted the researchers [Macnab \(1977\)](#). Hydrodynamic interaction analysis between two rotating flagella can be found in [Thaokar \(2008\)](#) [Powers \(2002\)](#) [Yang et al. \(2012\)](#).

Experimental investigations of elastic tail propulsion and bundling at low Reynolds number was implemented by several researchers. Kim et al. [Kim et al. \(2003\)](#) built a macroscopic scale model consisting of stepper motor-driven polymer helices in a tank filled with high-viscosity silicone oil. Tony et al. [Yu et al. \(2006\)](#) presented a macroscopic experimental investigation of a passive flexible filament propulsive mechanism.

Other related researches include energetic of synchronised states in three-dimensional beating flagella [Mettot and Lauga \(2011\)](#) and the orientation of swimming bi-flagellates in shear flows [Malley and Bees \(2012\)](#).

Another interesting interaction is the cilia internal mechanism [Gueron et al. \(1997\)](#) [Gueron and Levit-Gurevich \(1998\)](#) [Dillon et al. \(2000\)](#) [Kantsler et al. \(2013\)](#). The discussion includes unsteady model microorganisms [Ishikawa et al. \(2010\)](#), unsymmetrical microfluidic propulsion driven [Khaderi et al. \(2010\)](#) and magnetically-actuated artificial cilia [Khaderi et al. \(2011\)](#).

2.5.2 Interactions between swimmers and boundaries

The research in interactions between swimmers and boundaries at low Reynolds number is increasing dramatically in recent years. From the movement of slender bodies near plane boundaries [Katz et al. \(1975\)](#) to the motion of bacteria near solid boundaries [Lauga et al. \(2006\)](#), micro-cantilever oscillating near a wall [Clarke et al. \(2006\)](#), and helical swimming in-porous media [Liu \(2012\)](#).

The following researches have been conducted: hydrodynamic attraction [Berke et al. \(2008\)](#), dynamics and stability [Or and Murray \(2009\)](#) [Or et al. \(2011\)](#), passive filaments and active flagella [Evans and Lauga \(2010\)](#) of swimming microorganisms. The researches

include three-sphere swimmers [Zargar et al. \(2009\)](#), sperm motility [Fauci and McDonald \(1995\)](#) [Cosson et al. \(2003\)](#), and flagella.

Accuracy of far-field approximations [Spagnolie and Lauga \(2012\)](#) and two-dimensional model [Crowdy et al. \(2010\)](#) of self-propulsion near a boundary are also discussed.

Other research includes the complex fluid swimming [Leshansky \(2009\)](#) and Brinkman fluid swimming [Morandotti \(2012\)](#) can be classified in the boundary problem.

2.6 Micro swimmer analysis, design and optimisation

The research of microswimmers ranges from microorganism analysis to artificial swimmers locomotion optimisation. This section reviews related researches in this area.

2.6.1 Analysis

The analysis of swimming microorganisms is an extraordinary popular research topic including the analysis of the bacteria, the protozoa, the algae and spermatozoa.

It can also be found in recent papers in biophysics and biology of cell motility [Chen et al. \(2017a\)](#) [Waters \(2013\)](#) [Baskaran and Marchetti \(2009\)](#) [Spagnolie and Lauga \(2011\)](#) [Elfring and Lauga \(2011\)](#) [Dombrowski et al. \(2004\)](#). These researches investigate aspects from trajectories of bacteria [Hyon et al. \(2012\)](#) [Vaccari et al. \(2017\)](#) to optimal feeding of bacteria [Michelin and Lauga \(2011\)](#) and coordinated switching of bacterial flagella motors of *E. Coli* [Hu and Tu \(2013\)](#). There are also some analysis for flow field around nematode *Caenorhabditis elegans* [Montenegro-Johnson et al. \(2016\)](#) and cilia driven. [Mayne et al. \(2017\)](#) There is a review written by [Schuster and Khan \(1994\)](#) for the understanding of operation of the bacterial flagella motor.

The development in the technology of recording given people more direct methods to inspect bacteria flagella.

Bacteria have flagella filaments that are several microns long but only about 20 nm in diameter. When the bacteria move, the thrust is obtained by rotating the flagella. The flagella can be regarded as a slender body with different curvature and distortion values. The flagella filaments exist in different polymorphic forms with a rate of rotation of approximately 100 Hz.

Block [Block et al. \(1989\)](#) uses a single laser to determine the torsional compliance of flagella in tethered *Escherichia Coli* and motile streptococcus. He found that the spring-like linear torsion of the flagella of these bacteria was about half a turn and it was found that the flagella became stiffer when it exceeded the torsional amplitude in either direction. Turner [Turner et al. \(2000\)](#) found a simple procedure to label bacteria and their flagella by

using fluorescent. With this marking method, general cameras and ordinary fluorescent microscopes with mercury arc or stroboscopic laser irradiation can record the movement of bacteria and flagella in real-time.

Wiggins cite Wiggins 1998 studied the super-diffusion equation of elastic shape in viscous fluids, found the solution of pulse or oscillating force, and analysed the related factors affecting propulsion. Ten years later he also studied the joint movement of reciprocating swimmers. The results showed that two active particles that experienced reciprocal deformation could swim together [Lauga and Bartolo \(2008\)](#).

Hydrodynamic propulsion analysis of sperm is an active topic from investigation [Maude \(1963\)](#) [Winet et al. \(1984\)](#) to motility analysis [Davis and Katz \(1989\)](#) [Riedel et al. \(2005\)](#) [Kirkman-Brown and Smith \(2011\)](#) [Gillies et al. \(2009\)](#) [Olson et al. \(2011\)](#). The research about hydrodynamic phase locking of swimming microorganisms can be found in [Elfring and Lauga \(2009\)](#) [Niedermayer et al. \(2008\)](#). An impressive research about *Chlamydomonas* swimming was analysed with two in a eukaryotic version of run-and-tumble locomotion [Polin et al. \(2009\)](#). Another *Chlamydomonas* locomotion research can be found in [Foster \(2009\)](#). There is a review of recent findings of flagellum motor on rotor-stator interactions, on the role of different stators, and on how stator selection could be regulated [Microbiology et al. \(2010\)](#).

2.6.2 Design and optimisation

The Purcell three-link swimmer, which is the basic artificial micro swimmer, shown in [Fig: 2.5](#) is widely analysed in many researches, from the mathematical analysis [Becker et al. \(2003\)](#) [Najafi and Golestanian \(2004\)](#) [Pickl et al. \(2012\)](#) to experiments [Dreyfus et al. \(2005\)](#).

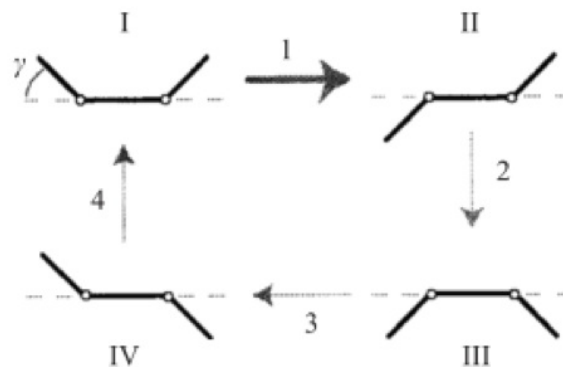


Fig. 2.5 Purcell's three-link swimmer [Purcell \(1997\)](#)

Tam et al. [Tam and Hosoi \(2007\)](#) modelled Purcell's three-link swimmer as a jointed chain of three slender rods moving in an inertia-less flow. They attained a more efficient swimmer and considered the slenderness influence. The research of the swimmer with hydrodynamics analysis [Alexander et al. \(2009\)](#) and a cargo container [Golestanian \(2008\)](#) was also conducted.

Edwin W. H. Jager ([Jager \(2000\)](#)), from Linköping University in Sweden, developed a micro-robot of the length of $670 \mu\text{m}$ and a width of $170 \mu\text{m}$ or $240 \mu\text{m}$. These robots had flexible elbows and wrist joints, and the research team made them a variety of shapes - each with two to four fingers on each hand. To enable these micro-robots to be able to move, the research team used conductive macro-molecules at their joints. The actuator used a gold bi-molecular film (polypyrrole a gold bi-layers). These polymers were able to adsorb or get rid of charged particles (ions) from the surrounding liquid according to their own charged charge. The researchers could control their charge by connecting the miniature wires of the robot. Absorption or rejection of ions caused swelling or contraction of the polymer, while the gold layer remains in its original state. By rationally arranging the polymer layer and the gold layer, the expansion and contraction of the joints of the robot caused them to bend when imparting different charges, similar to changes in thermostats caused by thermal changes. The bending of the polymer-gold layer caused the elbow and wrist of the robots arm to bend, and the fingers were stretched for gripping. Jager pointed out that there were many kinds of micro-robots, such as the use of electrodes and control rods of electronic equipment, artificial insects and mobile silicon robots, but no one could operate in the fluid.

An artificial low Reynolds number swimmer, based on the magnetic interactions of a pair of ferromagnetic particles was proposed by Ogrin et.al [Ogrin et al. \(2008\)](#). The analysis of transient swimming of a waving sheet was conducted by Pak [Pak and Lauga \(2009\)](#). A designing of phoretic micro- and nano-swimmers [Golestanian et al. \(2007\)](#) was proposed, the conclusion is the swimming velocity is size-independent for a given geometrical shape and surface pattern. It also provides a guide for optimising the design of swimmers.

[Itoh \(2000\)](#) characterised "negative galvanotaxis" based on protozoa and bacteria, that is, when DC voltage was applied to the culture medium, they would move toward the negative electrode, so they tried to control the use of protozoa as a biological micro Mechanical or micro-driver. At the beginning of 1994, the use of computer and image processing methods to achieve the intention of an operator to control the movement of paramecium, in 1998 to achieve the control of Paramecium rapid turning movement were possible. The experimental results showed that the precise control of Paramecium could be achieved by any predetermined trajectory. Besides, the output and power of a single

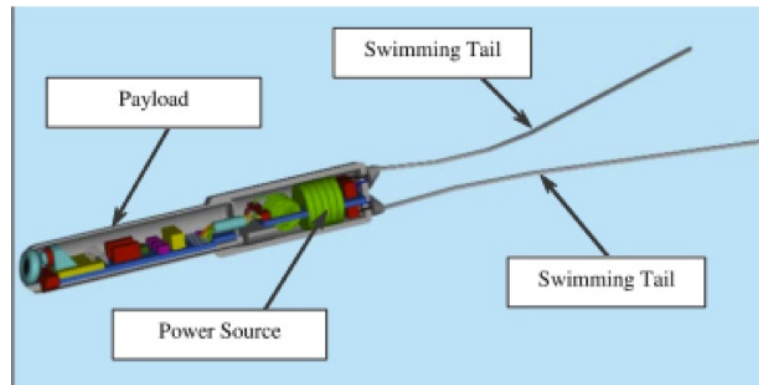


Fig. 2.6 travelling waves swimmer [Kósa et al. \(2006\)](#)

paramecium were measured. In 1999, some of the components of Paramecium were studied and found to have the characteristics of "negative order". [Tanaka and Fujita \(2015\)](#) also established a control software for driving paramecium, and develop light to control paramecium. The current swimming micro-robot have a cable power supply, known as cableway. But in practice, the cable approach is almost impossible to complete the task, so the study provides a way to use bio-energy for micro-robot to provide energy.

Kosa et al. ([Kósa et al. \(2005\)](#), [Kósa et al. \(2007\)](#), [Hata et al. \(2008\)](#)) proposed a swimming method mediated by elastic tail travelling waves. The swimming action relies on travelling waves generated along a piezoelectric layered beam that is divided into segments. The swimming model was theoretically analysed by solving the coupled electro-elastic fluid problem, and the tail structure was optimised to obtain reasonable thrust.

Becker ([Becker et al. \(2012\)](#)) proposed a similar piezo actuator driven microrobot and presented experimental results. Pawashe ([Pawashe et al. \(2008\)](#) [Pawashe et al. \(2013\)](#)) proposed a dynamic modelling of stick-slip motion in an un-tethered magnetic micro-robot. Zhang et al. ([Zhang et al. \(2009b\)](#), [Zhang et al. \(2009c\)](#), [Zhang et al. \(2009a\)](#), [Zhang et al. \(2010\)](#)) characterised the swimming properties of artificial bacterial flagella which used nano-belts to construct helical tail and adhere with soft-magnetic heads. Bio-inspired magnetic swimming micro-robots and magnetic helical micro-machines were reviewed in [Peyer et al. \(2013\)](#).

[Byun et al. \(2011\)](#) proposed a swimming micro-robot driven by an external alternating magnetic field. The magnet field generated by two pairs of Helmholtz coils. Ko, Youngho et al. proposed a jellyfish-like swimming mini-robot which driven by an electromagnetic actuation system [Ko et al. \(2012\)](#).

Another direction of artificial micro-swimmer is to employ microorganism's as driven method and this kind of works utilise different cells [Baudry et al. \(2005\)](#) [Williams et al.](#)

(2014) Roggo and van der Meer (2017) to generate thrust force for swimmer. Researchers even proposed a bacteria-based drug delivery system Lo et al. (2017).

The cilia swimming pattern is another interesting topic of design and optimisation. A review on the propulsion of mucus by cilia was given in Sleight et al. (1988). The optimisation of bio-inspired multi-segment IPMC cilia was proposed by Sareh et al. (2010).

Roper conducted an experimental with magnetic micro-swimmer and proposed a mathematical model. The results show that the swimmer's velocity and direction depend on magnet field parameters Roper et al. (2008). A swimming micro-robot based on artificial cilia was proposed for biomedical applications Ghanbari and Bahrami (2011).

2.7 Development of swimming micro-robots

In the industrial and daily life, there are numerous liquid fulfilled pipelines, such as oil pipelines, water pipelines, many of them buried in underground and spread widely. Their maintenance is an urgent problem to solve all through the world. Therefore, tube robot research has become a hot topic. For a more complex application environment, robot swimming in the blood can reach any part of the human body through blood vessels, and now a sub-mm miniature endoscopy has been developed for local treatment through the blood vessels in the body Kang et al. (2013). But the movement of this miniature endoscope is carried out by the hand of the operator's thrust, which will give patients a lot of pain, and also requires high-level operation skill of doctors. So, people are envisioned by the vascular robot for drug delivery or other forms of treatment. Based on the above problems, the research of the swimming micro-robot in the liquid will provide an optimised form for the pipeline robot, and also provide the basis for the research of the vascular robots. According to the driving method, swimming micro-robot can be divided into the following categories.

2.7.1 Shape memory alloy drive swimming robot

Some metals exhibit deformation by some external excitements such as by heating to the temperature above a certain threshold and can be restored to the shape before the deformation. This phenomenon is known as the *shape memory effect*. The metal with this effect is usually an alloy, so it is called a *shape memory alloy*. Shape memory alloy driver is the use of the shape memory effect in the output displacement and force to the outside work of the body. The current shape memory alloy is a micro-drive that can be the main drive with film drive, fibre drive, wire drive, spring drive and embedded drive Webb

et al. (2000) Kim et al. (2006). Various micro-robots have been developed according to the characteristics of shape memory alloys Rediniotis et al. (1997) Garner et al. (2000). For example, the United States and others have used a driver to study a robot propulsion device that can swim in liquids such as water by simulating fish's caudal fins to achieve the swimming forward Gorini et al. (2006) motion. Fig.2.7 shows the structure of the memory alloy propeller.

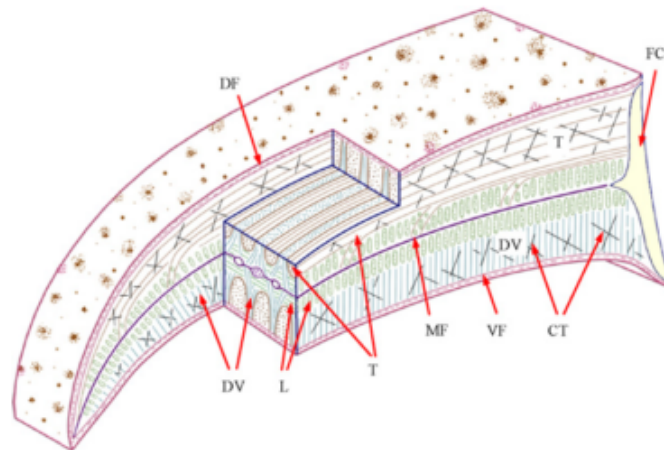


Fig. 2.7 Shape memory alloy propeller Webb et al. (2000)

2.7.2 Giant magnetostrictive material driven vibrating swimming robot

The magnetostrictive material principle is that the magnetic domain in the magnetic material of the magnetic field rotates until it is aligned with the direction of the magnetic field and causes the material to expand, so that the giant magnetostrictive material is deformed in the direction of the magnetic field line under the action of an external magnetic field. An electromechanical energy converter consisting of a giant magnetostrictive material will generate external displacement and force output under a magnetic field excitation so that it can act as a micro-actuator drive element Honda et al. (1996). Micro-actuators made of giant magnetostrictive materials have been used in micro-robots and have achieved good results Ishiyama et al. (2001b) Ishiyama et al. (2001a). Fig.2.8 is a micro-robot made of a giant magnetostrictive material Ishiyama et al. (2002).

As the external magnetic field changes, the film of the giant magnetostrictive device is constantly deformed to bend the film. This feature can be used in the liquid to swim like a fish to promote the movement of a micro-robot.

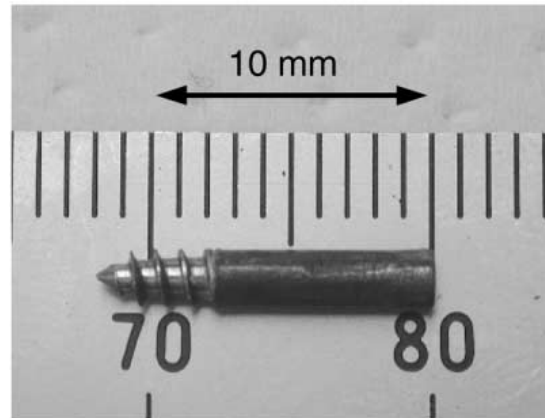


Fig. 2.8 Giant magnetostrictive robot [Ishiyama et al. \(2002\)](#)

2.7.3 Ferromagnetic polymer driven swimming robot

Ferromagnetic rubber is a rubber containing pure iron powder particles. To prepare such material, the particle size of $5 \mu\text{m}$ reduction of iron powder and silicone rubber put in a certain proportion of uniform mixing, and then placed in a mould at room temperature curing for 48 hours and finally the curable sample is cut into the desired shape to make micro-actuators. As the FMP contains pure iron powder, it has a soft magnetic property, both magnetic fields can be magnetised, resulting in magnetic attraction, when the magnetic field can be restored after the basic recovery of non-magnetic state [Gilbert et al. \(2011\)](#). At the same time, FMP substrate is silicone rubber with good flexibility and external force, it exhibits larger deformation and external force can be restored after the original state [Suzumori et al. \(2007\)](#) [Mathieu et al. \(2006\)](#). Fig.2.9 shows a swimming robot utilising ferromagnetic polymer propeller. The micro-robot have two particles, one with hard and another with the soft magnetic property. It can move in the liquid in an external magnetic field, and the robot can advance or retreat in the liquid by changing the intensity and frequency of the magnetic field.

2.7.4 Piezoelectric material components drive swimming robots

Compared with other micro-drives, piezoelectric components micro-drive has many advantages e.g. easy to miniaturise, fast response, easy control, little impact on the surrounding environment. In addition to the piezoelectric micro-drive, there is no magnetic field interference, low voltage drive. So, it is suitable as a micro-robots' driver [Sayar and Farouk \(2011\)](#) [Swee-Leong et al. \(2011\)](#) [Lopez-Sanchez et al. \(2001\)](#). FUKUDA et al. used a piezoelectric element to develop a double fin-fish microrobot, as shown in Fig: 2.10 [Fukuda et al. \(1994\)](#) [Guo et al. \(2003\)](#). The robot can swim in the liquid like a fish.

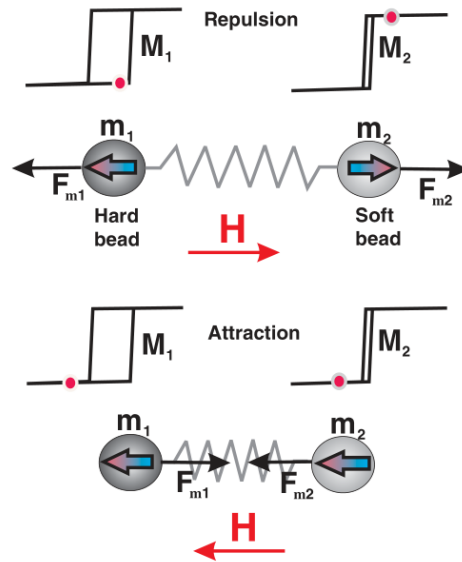


Fig. 2.9 Micro-swimming robot with Ferromagnetic polymer propeller [Ogrin et al. \(2008\)](#)

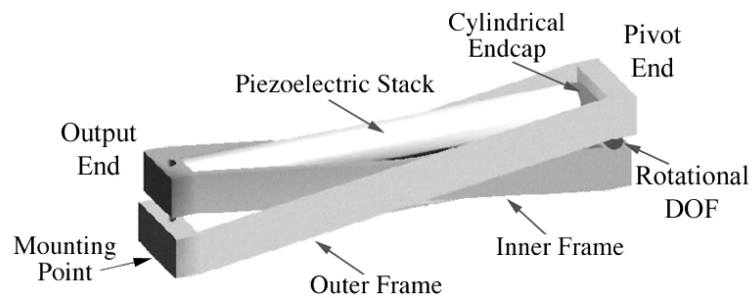


Fig. 2.10 Piezoelectric material propeller [Sayar and Farouk \(2011\)](#)

2.7.5 Ionic polymer metal composites (IPMC)

IPMC which is composed of cation exchange membrane and platinum and other precious metals through the chemical coating method. Since the microstructure of the IPMC material is ionised, the opposite polar charge on both sides of the polymer molecule is attracted and repelled by the action of the electric field, and the moving ions of the same charge polarity are migrated, causing IPMC. The film produces local shrinkage and swelling, and both sides produce a pressure gradient to form a bend. When an alternating voltage is applied, the film vibrates, and the bending displacement depends on the amplitude and frequency of the input signal. So, IPMC constitutes a driver or sensor. IPMC driver performance is very similar to a biological muscle and so-called "artificial muscle" and is suitable for the development of micro-robot driving materials [Guo et al. \(2012\)](#). It can produce the degree of manoeuvrability, no noise, flexible movements etc. and can be used to imitate the human arm, fish, insects and other acts of bionic robot [Sareh et al. \(2010\)](#). It provides high conversion of chemical energy to mechanical energy compared to a drive mechanism made of conventional materials [Ye et al. \(2009\)](#). At present, researchers used IPMC to develop a variety of swimming micro-robots [Guo et al. \(2006\)](#) [Kamamichi et al. \(2006\)](#). Fig.2.11 demonstrates a micro-robot with a flexible, low-voltage drive and in-vivo safety developed using an IPMC polymer driver. This miniature robot mimics the swimming principle of the fish, looks like a boat. It is 40mm long, 10mm wide, 2mm thick, with a pair of drive wings, driven by the pulse voltage to produce the driving force, by changing the pulse voltage frequency (3.1–5Hz) and can be utilised for swimming in the water characteristics.

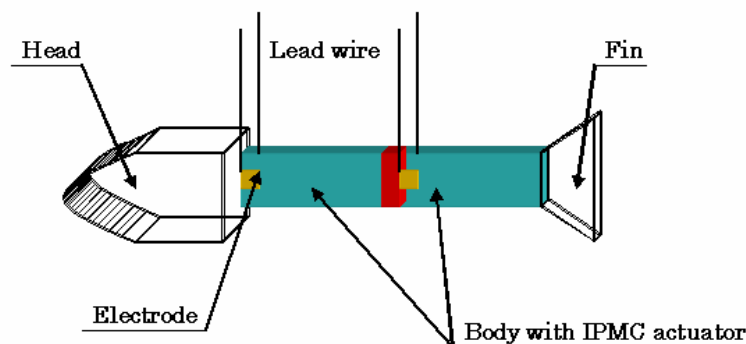


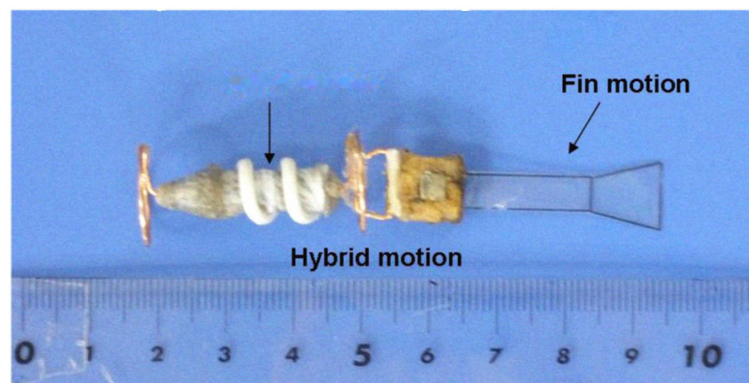
Fig. 2.11 Fish-like robot use IPMC propeller [Guo et al. \(2006\)](#)



Fig. 2.12 IPMC swimmer

2.7.6 Other types of swimming robots

At present, researchers use micro-motor or external magnetic field combined with the spiral drive to develop a variety of micro-robots' [Taheri et al. \(2009\)](#) [Chen et al. \(2010\)](#) [Desimone and Zoppello \(2017\)](#). Fig.2.13 shows a micro-robot driven by hybrid mechanism include spiral motion and fin motion. An external magnetic field act as the moving energy. The micro-robot is composed of a helical head and a fin tail which is rotated under the action of a magnetic torque by applying an external magnetic field, and the micro-robot drives by propulsion mechanism which under the changes of three axes Helmholtz coil [Okada et al. \(2011\)](#).

Fig. 2.13 Helical head driven by external magnetic field [Okada et al. \(2011\)](#)

2.8 Numerical methods

This section reviews the numerical methods involved in microswimmer and investigate the software and tools employed in this field.

There is an overview of the most common numerical solution strategies for the incompressible Navier-Stokes equations [Petter et al. \(2002\)](#).

The classical numerical solution for fluid dynamics is based on the Finite Volume Method (FVM), Finite Difference Method (FDM) and Finite Element Method (FEM). In recent year, some new methods have been proposed.

They include the immersed boundary method (IBM) proposed by Peskin [Peskin \(2002\)](#). Beside the modelling framework, the method also covers computer simulation of fluid-structure interaction, especially in biological fluid dynamics. Lim [Lim and Peskin \(2004\)](#) used this method to study the interaction between the elastic filament and the surrounding viscous fluid. Then the author [Lim et al. \(2008\)](#) also used this method to study the whirling instability of an elastic rod. Examples of segmented boundaries and forcing at random points are presented. This method is utilised in many applications for numerical study and simulation in recent years, especially for an elastic body in viscous fluid [Maniyeri and Kang \(2012\)](#) [Maniyeri et al. \(2012\)](#) and fluid-structure interaction in two-phase medium [Lee and Wolgemuth \(2012\)](#).

[Gauger and Stark \(2006\)](#) presented a detailed numerical study of a microscopic artificial swimmer which realised by Dreyfus et al. in the experiments in [Baudry et al. \(2005\)](#).

[Saintillan and Shelley \(2007\)](#) investigated numerically of orientational order and dynamics in super ions of self-locomotion slender rods. Then they developed a kinetic theory and applied to study the linear sterility and the nonlinear pattern formation in swimming micro-organism ([Saintillan and Shelley \(2008\)](#)).

2.8.1 Computational Fluid Dynamic (CFD)

With the rapid development of computer technology and the emergence of high-performance computers, computational fluid dynamics in fluid mechanics is growing rapidly. Since fluid mechanics as an independent discipline, for a long period, theoretical research and experimental analysis have been the most important means of research, but also formed a very great achievement. The arrival of CFD is considered after the invention of computers. The N-S equation is proposed in the 19th century. Because of the non-linearity of this partial differential equation, it is difficult to calculate its exact solution, and thus usually people employ a lot of physical simplification so that an analytical solution can be obtained. Unfortunately, plenty of important features are also lost in the process of simplification. So it is difficult to be used in industry application. Later, with the arrival of computers, the partial differential equation numerical solution theory gradually matures, finite difference method, finite element method, finite volume method, finite analysis method, boundary element method and other algorithms have sprung up. These methods have a series of common characteristics:

- (1) the entire area is divided into small areas, the calculations are applied in each small area;
- (2) the partial differential equation into algebraic equations to solve;
- (3) it is impossible to find an overall exact solution, only the exact solution at the critical position can be found.

Of course, there are some differences in these methods, the difference is only the discrete way.

The finite difference method (FDM) was first applied to the CFD solution. The main idea of this method is to apply the Taylor series to redefine the derivative term as the relationship between the node values. The main advantage is that one can easily adjust the calculation accuracy. But there is a very serious disadvantage: geometric adaptability is relatively poor. It is easy to construct the difference equation in the structural grid, but for the unstructured grid, the difference equation construction process is quite complicated. Finite element method (FEM) is currently used in many solid mechanics calculations, but in the fluid calculation of the application is rare. The main reasons for this are explained below.

- (1) The finite element method is based on node motion and uses Lagrangian grids which are similar to the Eulerian grids commonly used in fluid mechanics.
- (2) finite element method occupies a large number of computing resources, so the calculation of the number of the grid cannot be used too much, otherwise, the computer requirements are too high to implement.

However, hydrodynamics requires that the grid cannot be too large because it captures important characteristics of fluid motion, which are usually quite small in scale. Although finite element method has many problems in the fluid calculation, it is still one of the most important methods in fluid calculation due to its advantages such as high precision and precision can be infinitely adjustable. So, there is some popular finite element fluid calculation software.

The finite volume method (FVM) is another widely used method for mainstream general-purpose fluid calculation software. It combines some of the advantages of FDM and FEM. The core algorithm is to use Gaussian formula, in the limited control of the body to integrate, the volume points into the integral, and then use the differential method to construct discrete equations. The biggest advantage of this method is that it can keep the conservatism well and is very adaptable to the unstructured grid. CFD is a technology, a tool or a means, it is the result of the discrete calculations. It has the same characteristics as our common experiments. In many cases, CFD acts as a computer simulation test. In the CFD calculation process, it needs to pay special attention to some of the problems:

(1) boundary conditions. The boundaries in CFD do not necessarily coincide with reality. In the case of non-coincidence, it is very important for the determination of boundary conditions. For the boundary conditions directly determine the correctness of the results, the correct and accurate of boundary conditions are the prerequisites for the calculation.

(2) the results of the assessment. CFD calculation is completed, how to determine the merits of the calculation results. Realistic tests require reproducibility, CFD calculations do not require reproducibility (this is naturally satisfied), but it requires grid independence. So, the calculation results are not affected by grid changes.

A brief view of Numerical Software & Tools

The process of Computational Fluid Dynamics software is usually including several modules: build, pre-processor, solver and post-processor. There are numerous hydrodynamic solvers available ranging from free code to commercial software. Some of these solvers are listed in table 2.2 that may be used for microswimmer analysis.

Table 2.2 Softwares & tools

Name	Numerical Method	License Type
CFX	Finite-element-based control volume method	Commercial
FLUENT	Finite volume method	Commercial
PHOENICS	Finite volume method	Commercial
COMSOL (CFD)		Commercial
PowerFlow	Lattice Boltzmann Method	Commercial
FLOW-3D	Structured finite difference/control volume Finite element meshes for structural analysis	Commercial
STAR-CD	Finite volume method	Commercial
OpenFOAM	Finite volume method	GPL
GERRIS	quadtree (octree in 3D) finite volume method	GPL
Palabos	Lattice Boltzmann Method	GPL
Sailfish	Lattice Boltzmann Method	GPL
Code Saturne	Co-located Finite Volume method	GPL

2.8.2 Components of CFD software

pre-processor

The main function of the pre-processor is to prepare the model data for the solver. It mainly includes:

1. Define the geometric area of interest-the calculate domain
2. grid generation - the calculation domain is divided into small, non-overlapping areas
3. choose the physical and chemical phenomena that need to be simulated
4. Define the fluid properties
5. specify the appropriate boundary conditions

The solution of all flow problems (pressure, velocity, temperature, etc.) is carried out on the nodes inside the control body. CFD solution results are mainly grid number control. The more the number of grids is, the more accurate the results are. Solution accuracy and costs depend on the computational time spent on computer hardware and grid refinement. Good grids are usually not uniform: they are refined in areas where the amount of physical changes is large, and in areas where the variation is relatively small. The grid adaptive function of the CFD program is a direction of effort. Eventually, such programs will automatically perform grid encryption in a rapidly changing area. Before incorporating these technologies into commercial CFD programs, there is still a lot of work to be done to ensure their robustness. There is still a need to improve the ability of CFD users to design grids, which need to be chosen between computing accuracy and solution costs.

solver

There are three numerical solutions: finite difference method (FDM), finite element method (FEM) and spectral method. The finite volume method (FVM) which is widely used in commercial CFD programs such as CFX / ANSYS, FLUENT, PHOENICS and star-CD, is a special finite difference method. The numerical algorithm usually consists of a few steps:

1. Integrate the flow control equations in all finite control of the computational domain.
2. Discrete - converts the integral equation into an algebraic equation
3. The iterative method is used to solve the algebraic equation

post-processor

mainly include:

1. Regional geometry and grid display
2. Vector display
3. Line blanking and cloud map display
4. 2D and 3D display
5. Particle tracking
6. View operation (pan, rotate, zoom, etc.)
7. Picture output

2.9 Summary

This chapter focuses on the literature background of this research. The micro-swimmers such as bacteria and sea urchin attracted researchers for many years. At the first stage, the research focus on the swimming principles of natural swimmers. The principle of swimmers in low Reynolds number is explored and several theories are presented. After that, artificial micro-swimmers design and analysis have been discussed.

To develop a micro-swimming robot that can be used in medical applications or other industries, people have made great advances so far. But there is still a long way to go and many issues need to be solved. One of the most important issues is the mobility. The movement performance of a micro-swimming robot needs to be improved for its usability in many applications. The following chapter presents the design and modelling of micro-swimming robots with simple structure which can increase the velocity. The simulation and experiments have been conducted to prove the viability of this model.

Chapter 3

Design and Modelling of Artificial Micro-Swimmer

3.1 Introduction

The swimming micro-robot model starts from the discussion of the solution of Navier-Stokes equation. Fortunately, the micro-swimmers can be regarded as swimming in low Reynolds number flow which is dominated by Stoke equation. The research starts from a simple design which contains just one helix flagellum. After that, the whole swimmer is discussed, and then the swimmer with double flagella. These designs are analysed by suitable modelling method and are discussed in dimensional details. The optimisation is conducted for flagella and body respectively.

3.2 Design and Modelling of a Rigid Flagellum

3.2.1 Design of a rigid flagellum

The design of the rigid flagella is derived from the shape of the microbial flagellum and the tail material is set to rigidity. Most microbes that rotate the flagellum are a left-handed spiral(Lighthill (1976)). The parameters to be considered are shown in Table 3.1. The position of the flagella corresponding to these parameters is shown in Fig. 3.1.

Table 3.1 Parameters in Rigid Flagellum Design

Parameters	Expression	typical range
Helix amplitude	R	
Wavelength	λ	$2R < \lambda < 11R$
Length	L	$3\lambda < L < 11\lambda$
Pitch angle	θ	
Contour Length	$\Lambda = L/\cos\theta$	
Filament radius	a	

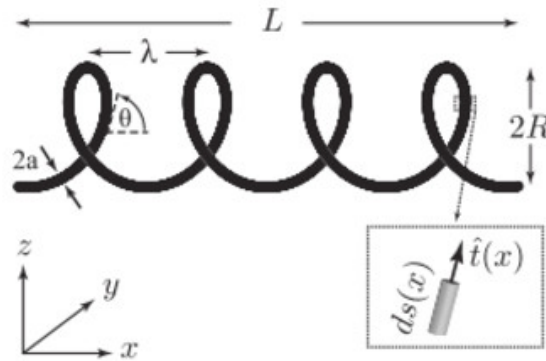


Fig. 3.1 Rigid Tail model

3.2.2 Modelling of a rigid flagellum

Base on the design of a rigid flagellum, it is necessary to discuss the modelling method. Firstly, the Reynolds number need to be considered. The typical Reynolds number for flagellum is $10^{-4} - 10^{-2}$ from $Re = \rho\Omega R^2/\mu$ (Ω is the rotation rate; μ , the dynamic viscosity; and ρ , the fluid density). A rotating helical flagellum can produce forward thrust. The thrust F and torque τ have a relationship with flagellum's axial velocity U and rotation rate Ω which shown in

$$\begin{pmatrix} F \\ \tau \end{pmatrix} = \begin{pmatrix} A & B \\ B & D \end{pmatrix} \begin{pmatrix} U \\ \Omega \end{pmatrix} \quad (3.1)$$

This 2×2 matrix proposed by Purcell (1977). The equation shows that the propulsion thrust depends on the rotation torque and geometry parameters of the flagellum.

Where the values of A, B and D are shown below in the following equations.

$$A = 2\pi nR \left(\frac{\xi_{\parallel} \cos^2 \theta + \xi_{\perp} \sin^2 \theta}{\sin \theta} \right) \quad (3.2)$$

$$B = 2\pi nR^2 (\xi_{\parallel} - \xi_{\perp}) \cos \theta \quad (3.3)$$

$$D = 2\pi nR^3 \left(\frac{\xi_{\perp} \cos^2 \theta + \xi_{\parallel} \sin^2 \theta}{\sin \theta} \right) \quad (3.4)$$

where the value of ξ_{\parallel} and ξ_{\perp} is present in

$$\xi_{\parallel} = \frac{4\pi\eta}{\ln\left(\frac{0.36\pi R}{a \sin \theta}\right) + \frac{1}{2}} \quad (3.5)$$

$$\xi_{\perp} = \frac{2\pi\eta}{\ln\left(\frac{0.36\pi R}{a \sin \theta}\right)} \quad (3.6)$$

where R is helix amplitude, η is viscosity and a is filament radius.

Another drag coefficients from [Lighthill \(1976\)](#) is show in

$$\xi_{\parallel} = \frac{2\pi\eta}{\ln\left(\frac{2\lambda}{a}\right) - 2.9} \quad (3.7)$$

$$\xi_{\perp} = \frac{4\pi\eta}{\ln\left(\frac{2\lambda}{a}\right) - 1.9} \quad (3.8)$$

where λ is the wavelength.

3.3 Design and Modelling of a Single Rigid Flagellum with a body

3.3.1 Design of a single rigid flagellum with a body

The basic components of this design consist of a body, a spiral flagellum and a connecting part between the two. The connecting portion is seen as a hook that extends from the body and is attached to the spiral flagellum. The connecting part receives the torque from the body and conducts it to the spiral flagellum. The torque is the active component that drives the motion of the whole system. This design is from [Lobaton and Bayen \(2009\)](#) and utilise different modelling method in this research.

The flagellum is a spiral structure that is rotated by the effect of the torque applied thereto. Specifically, the main part of the model is designed as an ellipsoid; the flagella portion is designed as a tubular spiral with a centerline; the connecting portion is designed as a conical spiral with a centerline, and the conical spiral centerline represents a hook connecting the main body to the flagella. The design is shown in Fig. 3.2.

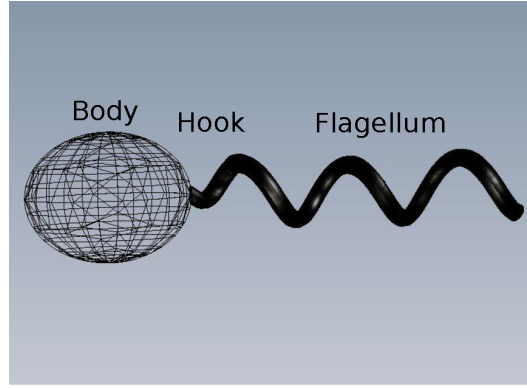


Fig. 3.2 Tail model with body

3.3.2 Modelling of a single rigid flagellum with a body

In propulsive matrix Equ. 3.1, the off-diagonal elements should be negative, $B < 0$, for a right-handed spiral. The rotate direction of the torque needs to meet the condition of $\omega < 0$ to drive the helix and push the system to the left, ie. $v > 0$. The external force F acting on the helix is negative, that is, toward the right side.

The body itself is characterised by the propulsion matrix P_0 , which is presumably diagonal, with its only nonzero elements A_0 and D_0 as $A_0 = 6\pi\eta a$ and $D_0 = 8\pi\eta a^3$.

The body part rotation reversed, which means $\Omega < 0$. Considering the above requirements, to meet the balance of force and torque on the central axis of the spiral, the following conditions must be met:

$$A_0 v = -A v - B \omega \quad (3.9)$$

$$D_0 \Omega = -B v - D \omega \quad (3.10)$$

Since the motor itself is also rotating, its speed can be expressed as $\omega - \Omega$, which is the speed of the "rotor" connected to the flagella relative to the "stator" attached to the outer

wall of the body, which is greater than ω . Let the motor speed be set to Ω_m and derive the following equation:

$$v = -\frac{BD_0}{(A_0 + A)(D_0 + D) - B^2}\Omega_m \quad (3.11)$$

From this, there are two steps approximation can be done.

Step 1, in some practical cases, B^2 is much smaller than AD . Because $B^2 \ll AD$, the equation Equ. 3.11 can be well approximated by

$$v = -\frac{BD_0}{(A_0 + A)(D_0 + D)}\Omega_m \quad (3.12)$$

Step 2, the factor $D_0/(D_0 + D)$ is just the ratio $\omega/|\Omega_m|$. Because the reverse rotation speed of the main body portion is much slower than the rotation speed of the flagellum. So the value of $D_0/(D_0 + D)$ will be close to 1. Therefore, the equation can further be approximated by

$$v = -\frac{B}{A_0 + A}\Omega_m \quad (3.13)$$

Next, the efficiency is discussed. Firstly, the torque τ exerted by the motor on the flagellum is present in

$$\tau = \frac{B^2 - D(A_0 + A)}{B}v \quad (3.14)$$

Let the output power of the motor be $\tau\Omega_m$, and the minimum power required to push the entire structure move at the speed of v is A_0v^2 . The ratio of A_0v^2 to $\tau\Omega_m$ is the definition of the propulsive efficiency E . With the relations above, the efficiency is present in

$$E = \frac{A_0v^2}{\tau\Omega_m} = \frac{A_0D_0B^2}{[(A_0 + A)D - B^2][(A_0 + A)(D_0 + D) - B^2]} \quad (3.15)$$

use the same approximation steps, the efficiency can be derived in

$$E = \frac{A_0B^2}{(A_0 + A)^2D} \quad (3.16)$$

Assumption: The body's motility does not seriously affect by the flow around the propeller.

3.4 Design and Modelling of Double rigid Flagella with a body

3.4.1 Design of double rigid flagella with a body

This design proposed by this research and it is inspired by the structure of DNA. The moving velocity and efficiency may increase significantly by using this structure. The design contains a rigid body and 2 rigid tails connected to the body. The connection part, which consists of a hook coming out from the body and attaches to the two helical flagella, has at its base the rotor engine that drives the motion. The design is present in Fig. 3.3.

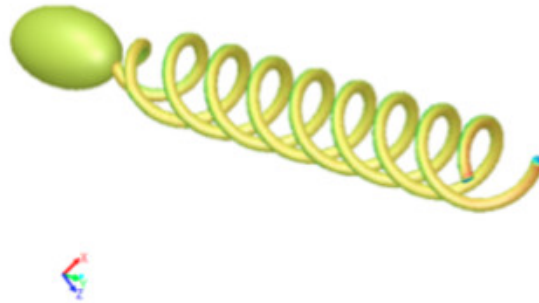


Fig. 3.3 Design 3 Double-tails with body

3.4.2 Modelling of double rigid flagella with a body

From this design, it is predictable that the flow around tails will move faster than a single tail. The velocity of the swimmer should have bigger performance than previous ones and presented by

$$v = -\frac{B^2 D_0^2}{(A_0 + A)(D_0 + D) - B^2} \Omega_m \quad (3.17)$$

A simulation-based on this design has been conducted and illustrated in chapter 4. The prototype fabrication and experiment conducted in chapter 5. It can be noted that this design is difficult to fabricate. By using 3D-printer technology, it is easy to get a accurate physical model based on the designed shape and size. The difficult part of fabrication is the connection which is connecting the motor from the body and the flagella.

The junction part structure design contains rotor, stator, bushing and a three-way connector that connect the motor and two flagella as shown in Fig. 3.4.

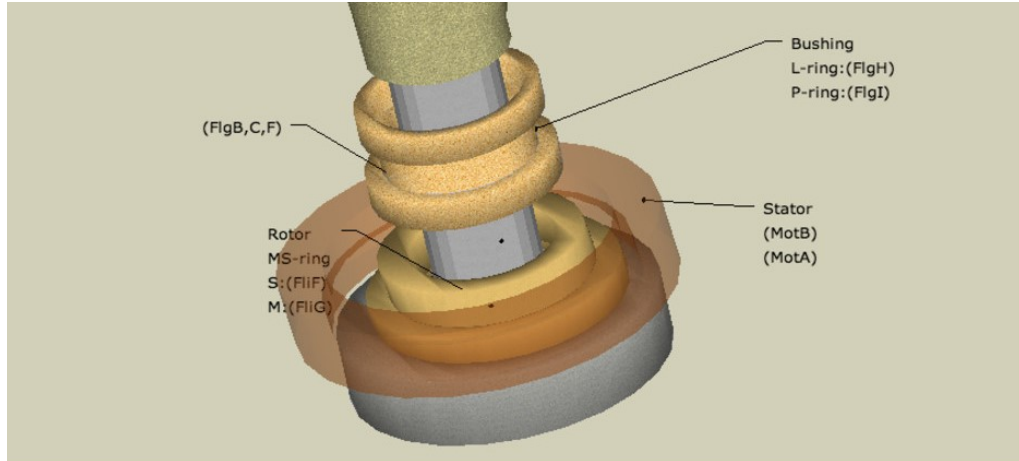


Fig. 3.4 Junction part structure design

3.5 Shape Optimisation

3.5.1 Flagellum Shape optimisation

It can be noted that the whole shape of the flagellum is similar to a cylinder as shown in Fig. 3.5. The shape changes slightly when in motion. There are several different structures for the artificial flagellum. The comparison of these structures is given in this section. The performance comparison is based on the models of each flagellum conducted by resistance force theory. The condition of this theory is the low Reynolds number. It can be set for helix radius A is 6mm , the rotational speed of motor w is 0.1Hz . The environment parameters set as follow:

$$\text{Dynamic viscosity } \mu = 10^4 \text{Ns/m}^2,$$

$$\text{Density } \rho = 9.55 \times 10^2,$$

It can be calculated for $Re \approx 10^{-5}$, the environment is similar to Stoke flow. Under this condition, the inner force is much smaller than the viscous force, so the resistance force theory can be applied to calculate the thrust force. It needs to define some parameters for analysing the thrust force and torque of artificial flagellum. The pitch of the artificial flagellum can be fixed when designing this conical-helix.

The optimisation of the shape of a helical flagellum is important for improving swimming performance independent of the input field.

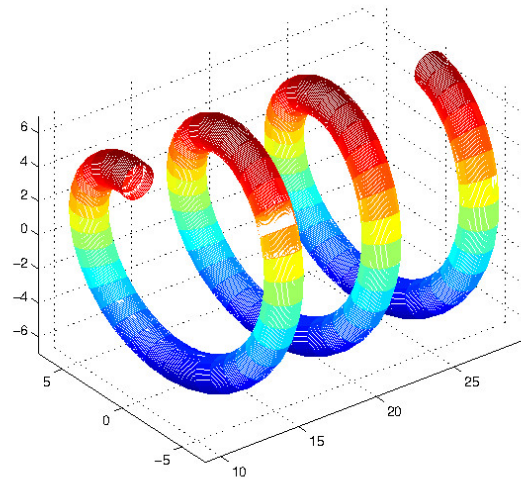


Fig. 3.5 Flagellum shape

For the convenient discussion for the optimisation, the designed model set to only a helical flagellum. The engine is modelled by a torque. The optimisation is base on the model of Equ. 3.1 to Equ. 3.6.

The Optimisation method is the Preconditioned conjugate gradients method. The Conjugate Gradient Method is the most prominent iterative method for solving sparse systems of linear equations. The conjugate gradient method is an algorithm for finding the nearest local minimum of a function of variables which presupposes that the gradient of the function can be computed. It uses conjugate directions instead of the local gradient for going downhill. If the vicinity of the minimum has the shape of a long, narrow valley, the minimum is reached in far fewer steps than would be the case using the method of steepest descent.

The optimisation is an iteration process. Firstly, the grid-point method (globally method) is utilised to identify the value range of parameters. secondly, one of the parameters set as a variable, other parameters set as constants. The relationship between the variable parameter and the velocity is calculated.

The parameters involved in the model is given below.

Number of pitch n ,

Helix amplitude R ,

wavelength λ ,

length L ,

pitch angle θ ,

filament radius a .

There are some relationship between these parameters, for example, $L = \lambda n$, $\tan\theta = R/\lambda$, so the following four independent parameters are discussed.

- wavelength λ ,
- helix amplitude R ,
- helix wave number n
- filament radius a .

Firstly, the relationship between wavelength λ and velocity is illustrated. From the model, it can be predicted that the velocity will increase with the wavelength rising in a specific range, and then keep at a stable level.

Fig. 3.6, Fig. 3.7, Fig. 3.8, Fig. 3.9 show the same trend.

The dimensionless relationship identified there is a respectively stable value of velocity with wavelength increasing.

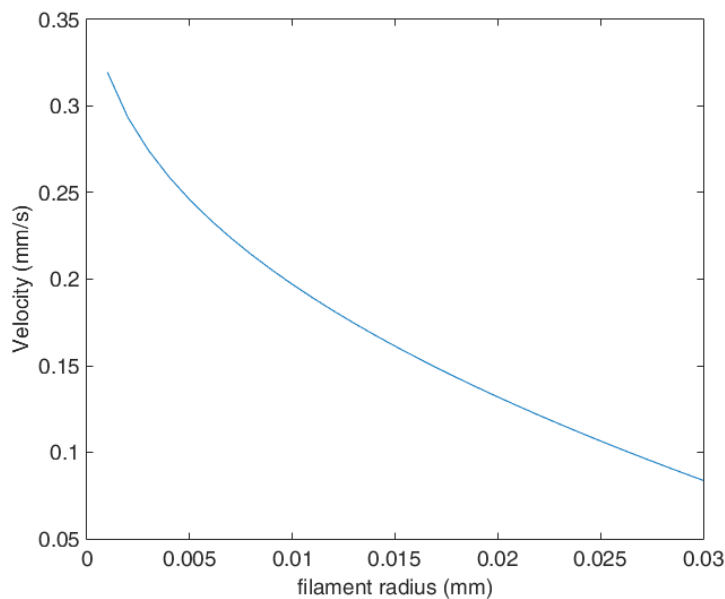


Fig. 3.6 Relationship between velocity and filament radius

From the results, it can be found that there is a maximum value of velocity during the helix amplitude increase. As the helix wave number increases, the velocity shows a decreasing trend.

In further research, the parameters should be considered in the control stage:

1. The magnitude of torque;

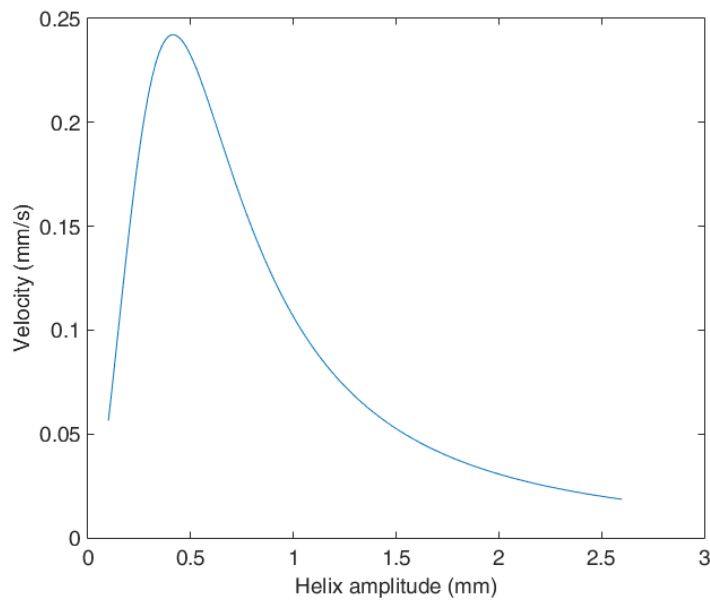


Fig. 3.7 Relationship between velocity and helix amplitude

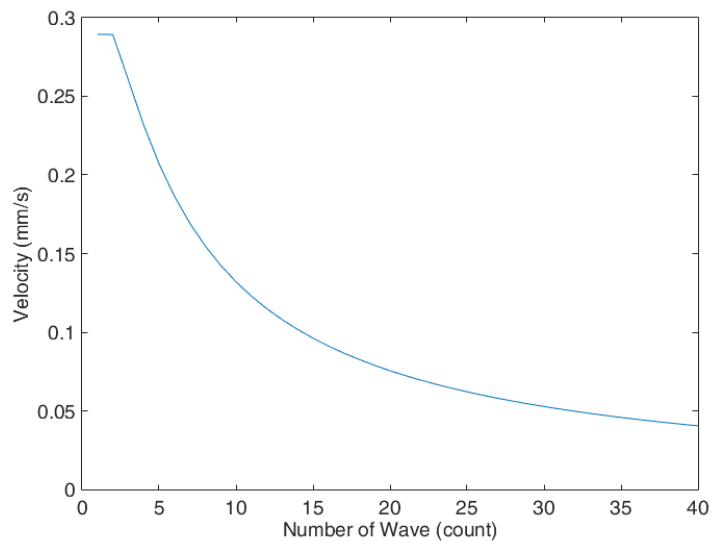


Fig. 3.8 Relationship between velocity and wave number

2. Dimensionless time;

The results to be monitored:

1. Angular velocity;
2. Forward displacement;

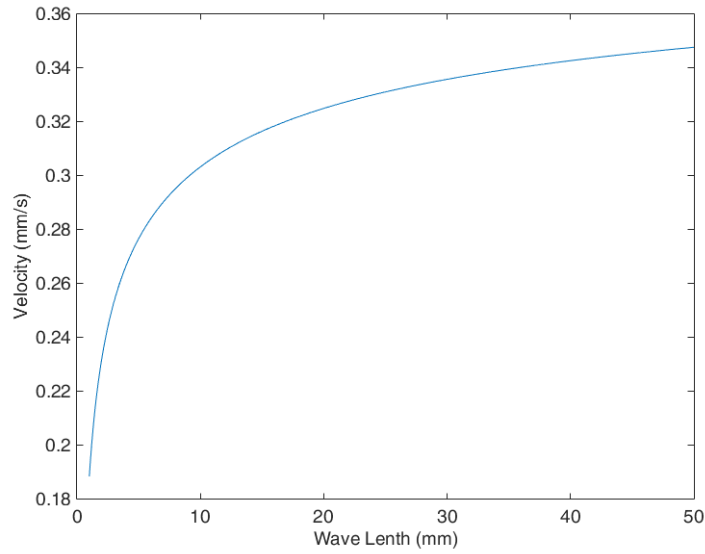


Fig. 3.9 Relationship between velocity and wave length

3. structural stability;
4. Thrust force;

For further optimisation, it is necessary to employ some multi-independent variable optimisation method to identify the parameters of respectively high performance of the swimmer.

3.5.2 Body Shape Optimisation

The body shape of artificial micro-swimmer is a rotational ellipsoid. The length of the long axis equals a and length of short axis equals b . The advantage of this shape not only drag convergence caused by streamlined, but also enough space for components like motor, battery etc. The drag applied on the body including viscous force and viscosity moment. The relationship between them and transitory velocity U and rotation speed ω of body is in

$$F_b = C_F U \quad (3.18)$$

$$T_b = C_M \omega \quad (3.19)$$

where the coefficient C_F and C_M are 3×3 diagonal matrix shown in

$$C_F = 6\pi\mu a \begin{pmatrix} C_{F3} & * & * \\ * & C_{F3} & * \\ * & * & C_{F1} \end{pmatrix}, C_M = 8\pi\mu ab^2 \begin{pmatrix} C_{MR} & * & * \\ * & C_{MR} & * \\ * & * & C_{M0} \end{pmatrix} \quad (3.20)$$

where

$$C_{F1} = \frac{Se^3/3}{-2e + (1 + e^2)\ln(1 + e)/(1 - e)} \quad (3.21)$$

$$C_{F3} = \frac{16e^3/3}{2e + (-1 + 3e^2)\ln(1 + e)/(1 - e)} \quad (3.22)$$

$$C_{M0} = \frac{4e^3/3}{2e - (1 - e^2)\ln(1 + e)/(1 - e)} \quad (3.23)$$

$$C_{MR} = \frac{(4e^3/3) \times ((2 - e^2)/(1 - e^2))}{-2e + (1 + e^2)\ln(1 + e)/(1 - e)} \quad (3.24)$$

and $e = \sqrt{a^2 - b^2}/a$. From the coefficient relationship above, the viscous force and viscosity moment are related to body shape. So, it is possible to get the drag convergence through optimisation of the body shape.

If the volume of the inner ellipsoid body be set to a fixed value like $V = 2.8 \times 10^{-5} (m^3)$. It is clear that there is only one independent variable about body shape (From the volume calculation formula of ellipsoidal $V = \frac{4}{3}\pi ab^3$). It can be set so that the short axis b is the independent variable, then $a = \frac{3V}{4\pi b^3}$. The range of values of short-axis b is limited by condition $a > b$. It is can be defined that aC_{F1} as the first coefficient of drag, aC_{F3} as the second coefficient of drag, ab^2C_{M0} as the third coefficient drag, ab^3C_{MR} as the forth coefficient of drag. The relation of the coefficients and short-axis b is shown in Fig. 3.10 and Fig. 3.11.

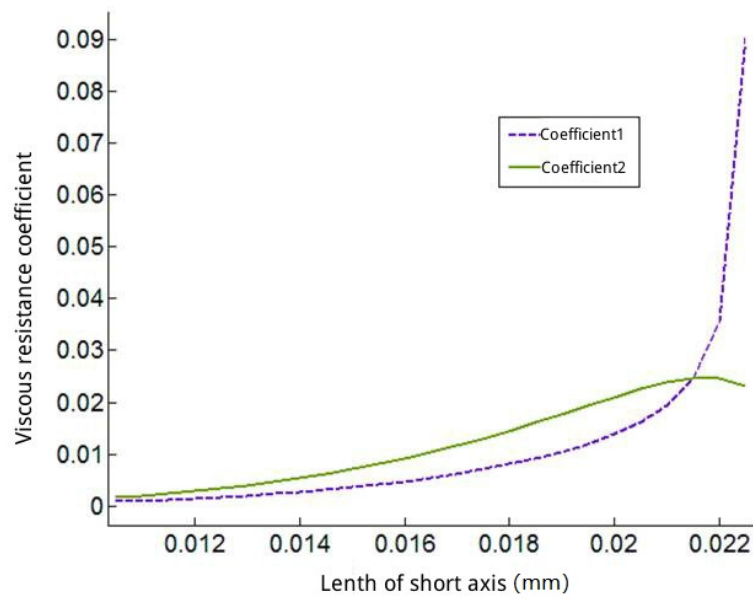


Fig. 3.10 Changing of viscous resistance force coefficients depend on short axis

From Fig. 3.10, it can be found that the viscous resistance force coefficient is going up with the increasing short axis length. But different coefficients have different change trends.

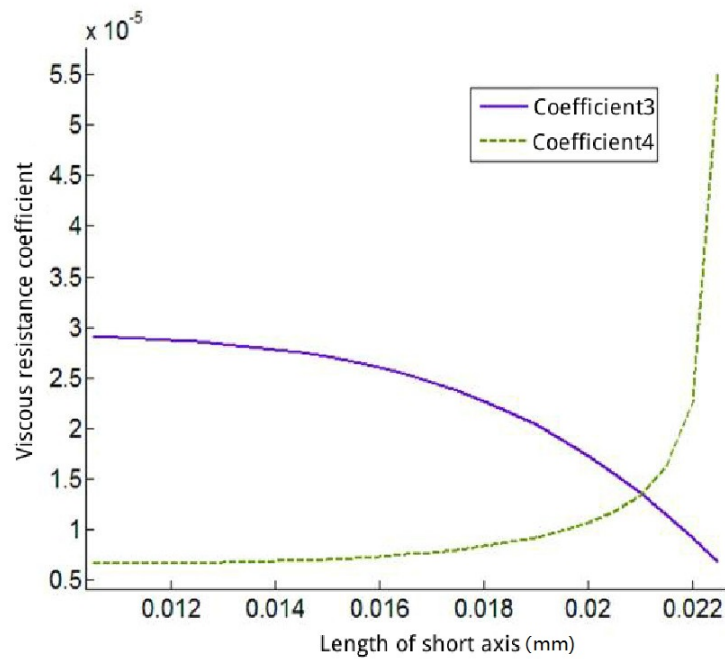


Fig. 3.11 Changing of viscous resistance torque coefficients depend on short axis

From Fig. 3.11, it can be found a similar trend with Fig. 3.10, the resistance torque coefficients growth slowly with short-axis size increasing, and resistance torque coefficients got a sharply increase with a certain value of short axis for the third coefficients.

3.6 Summary

This chapter presents the derivation of the kinetic and dynamic models of micro-swimming robots based on RFT. The process of evolution is from rigid single flagellum, rigid single flagellum with a body to rigid symmetry double flagella with a body. From these models, the optimisation is conducted to identify the range of helix parameters settings. The model and the parameter settings are the base of the remaining parts of the thesis. The 3D model for simulation built in chapter 4 is based on the parameters set. The prototype developed in chapter 5 also utilises the parameter settings proposed in this chapter.

Chapter 4

Simulation and Analysis

4.1 Introduction

In this chapter, simulation is executed for two case studies. One is a pipe inspection robot, which is millimetres scale size. The results of this simulation are compared with the experiment results in the next chapter for validation.

Another case is a swimmer robot for human blood vessel, which is in micro-meter scale. Since there is not enough fabric technology to develop a real prototype for this case, simulation is the only method to verify the design for this kind of application.

Both cases have the same environment that the robots are swimming in low Reynolds number flow. The Reynolds number of case 1 can be calculated using Eq. 1.2.

From the dimension and environment of the pipe inspection robot, the value of variables in the equation is $\rho = 0.97g/mL$, $L = 94mm$, $U = 4 \sim 39mm/s$, $\mu = 1000CSt$. Reynolds number of case 1 is given in Eq. 4.1,

$$Re = \frac{\rho LU}{\mu} \sim \frac{\text{inertial forces}}{\text{viscous forces}} \simeq 0.027 \quad (4.1)$$

which is far small than 1, so the environment of case 1 can be regarded as low Reynolds number flow.

The Reynolds number of case 2 can be calculated based on human blood's physical properties. The variables have the values as $\rho = 1.054g/mL$, $L = 13.7\mu m$, $U = 12 \sim 40\mu m/s$, $\mu = 1.779CSt$, Reynolds number of case 2 is $0.042 \ll 1$, it is also a typical low Reynolds number flow.

So both cases can be solved with the low Reynolds number flow model explained in Chapter 3.

The process of simulation is as follows:

(1) Workbench module to organise the whole process;

- (2) Model module (Spaceclaim) to build up the geographic model;
- (3) Mesh module (mesh) to create the mesh of model;
- (4) Solve module (Fluent) to execute the Calculations;
- (5) Post-processing

The simulation of this research is based on fluid-solid coupling mechanics. An important feature of fluid-solid coupling mechanics is the interaction between two different media. The fluid motion will cause solids deformation or motion. At the same time, the deformation or movement of the solid in turn affects the movement of the fluid, thereby changing the distribution of the fluid load. This interaction effect may initiate by solids or by fluids.

This research employ ANSYS as the simulation software. This kind of simulation in ANSYS have two solutions, one is fluid-structure interaction (FSI) and another is 6 degree-of-freedom (6DOF).

FSI is a method for the study of the behaviour of the deformed solid under the action of the flow field and the interaction of the solid shape to the flow field.

Nowadays, due to the development of numerical calculation methods and computing technology, the FSI solution tends to solve N-S equation (Navier-Stokes equations) and nonlinear structural dynamics. Generally, the iterative solution is used, that is, in the flow field, the structure of the solution, in each time step between the coupling iteration, convergence and then move forward. The advantage is that mature code in their respective fields can be applied with minor modifications. This may also involve a dynamic grid problem. Due to the deformation of the structure, the computational domain of the flow field changes, and the deformation of the flow field grid is considered to adapt to the deformation of the coupling interface. The framework of the FSI method applied in ANSYS Workbench is shown in Fig. 4.1

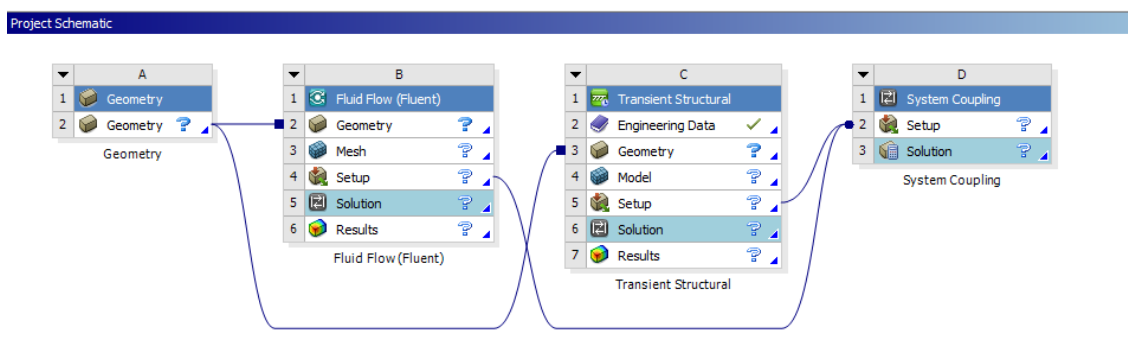


Fig. 4.1 The framework of FSI method using ANSYS

4.2 Simulation Case 1-Pipe Inspection Robot

Pipeline detection robot is the most commonly used mechanical and electrical integration device for the pipeline inspection application. It can carry a variety of testing equipment, with the operator's control or automatic control to complete the pipeline detection operations.

With close inspection, it can find defects such as deformation, damage, corrosion, perforation, thickness changes of pipe wall or coating and obtain accurate and reliable detection data. Based on the analysis of these data, pipeline safety assessment and integrity management can be improved.

With the continuous development of computational science and numerical analysis methods, the study of fluid-structure coupling, or fluid-structure interaction has drawn wide attention from academic and industrial communities in recent years. The fluid-solid coupling problem is a branch of mechanics generated by the intersection of Computational Fluid Dynamics (CFD) and Computational Solid Mechanics (CSM). It is also an important branch of multidisciplinary or multi-physics research. It is a study of a variety of behaviours of deformable solids under the influence of the flow field and the influence of solid deformation on the flow field affect the interaction between the two.

The problem of fluid-structure coupling can be understood as both a solid solution and a fluid-solution, both of which cannot be ignored. Because of both fluid and structural properties are considered, fluid-structure interaction can effectively save time and cost of analysis, while ensuring that the results are closer to the laws of the physical phenomena themselves. Therefore, in recent years, the application of fluid-structure interaction analysis in engineering design, especially in virtual design and simulation has become more and more extensive and in-depth.

In this research, only one kind of pipe inspection robot is discussed which is the robot swimming in a pipe fulfilled with Stokes flow such as petroleum. The environment condition is the same as discussed in chapter 3. So, the design is suitable for this application. This research follows the process as described below. The prototype is developed based on the cross-development method shown in Fig. 4.2.

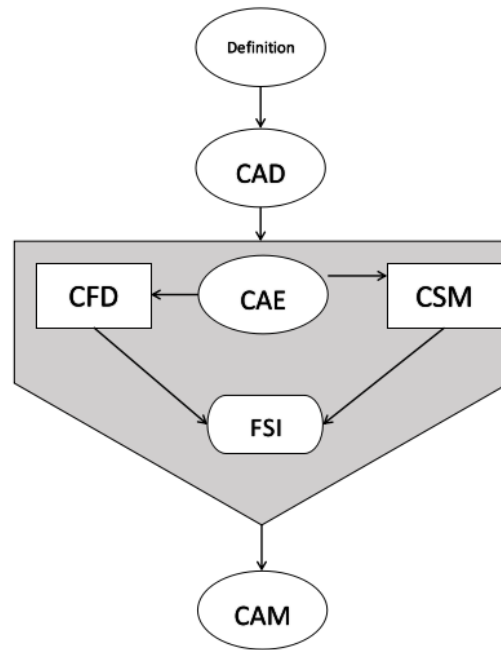


Fig. 4.2 Cross Development method for FSI using ANSYS

The first stage: prototype design phase, the main use of Computer-Aided Design (CAD) prototype design by product structure design.

The second stage: Prototype virtual simulation phase, mainly through Computer-Aided Engineering (CAE) on the initial design of product performance evaluation. According to the characteristics of various disciplines, the simulation analysis mainly includes: Computational fluid dynamics analysis, Computational solid mechanics analysis, Computational acoustics and Computational electromagnetism analysis. Among them, the analysis combining computational fluid dynamics analysis and computational solid mechanics analysis is simply referred to as fluid-structure interaction analysis.

The third stage: prototype processing stage, the main use of computer-aided processing methods and means of prototype Computer-Aided Manufacturing (CAM).

Wherein, if it is found in the second stage that the prototype performance can not meet the design requirements, it can return to the first stage. In the third stage, if there is a problem with the finished prototype, it can be returned to the first stage and the second stage for redevelopment and design, respectively.

4.2.1 Problem Identification

In the simulation, the flow field around the swimmer needs to be identified and the swimming velocity needs to be calculated in a fixed time domain. Through the analysis of flow around the swimmer, the performance of the designed swimmer would be verified.

The gravity of the robot can be ignored since the mass of the robot can be adjusted to match the buoyancy force it receives in prototype fabrication.

The consideration of robot mass

The mass of the robot may create two effects. One is gravity, and another is inner force.

For the gravity issue, the mass of the robot is 0.4 gram, it receives a gravity of 0.00392N. Gravity makes the robot goes down. On the other hand, the volume of the robot is about 147mm^3 , the buoyancy force it receives is 1.403N. To balance the forces in vertical, a weight gain block needs to planted in robot to increase gravity. The mass of weight gain block can be calculated using:

$$M_w = (F_b - G_r)/g \quad (4.2)$$

Where M_w is the mass of weight gain block, F_b is buoyancy force the applied on the robot, G_r is the gravity applied on the robot, g is the acceleration of gravity, which is 9.8N/kg .

For the inner force issue, based on the basic environment condition in Low Reynolds number flow explained in Chapter 1, the inner force is much smaller than viscous force. So, the mass of the robot can be ignored both in simulation and experiment with the weight gain block added.

Goal Definition

The goal of the simulation is to identify the performance of the designed robot in a specific application. The environment condition satisfies with the experiment condition. The affection factors of performance are discussed after the simulation results obtained.

Domain Identification

Since the simulation results need to be compared with the experiment results, the computation domain has the same properties as the experiment settings. The domain ranges from the robot surface to the tank inner wall. The size of the domain is $420\text{mm} \times 130\text{mm} \times 100\text{mm}$. Fig. 4.3 shows the proportion of the computing domain and the robot. The time domain is set to 12 seconds for the limitation of computing ability.

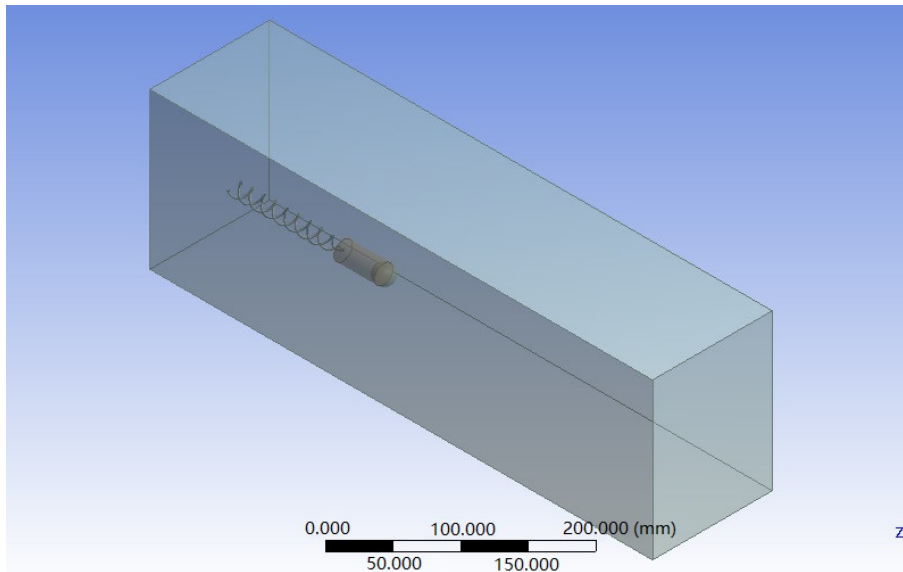


Fig. 4.3 Case1-Domain identification

The computing domain is from the surface of the robot to the wall of the oil tank. The details of the whole flow field should be inspected.

4.2.2 Pre-processing

The purpose of this stage is to complete the preparation for calculation. The tasks of the pre-processing stage mainly include geometry modelling and meshing.

Geometry

Body(a Cylinder and a half-sphere)

Length: 25mm

Radius: 6mm

Sphere head fore-side

Connection (Conical helix)

Length: 11mm

Amplitude: 0–12mm

Radius: 1mm

Double Tail (Cylinder helix)

Length: 58mm

Amplitude(2R): 12mm

Helix pitch: 16mm

Radius:

The body shape adopted a cylinder and a half-sphere rather than ellipsoid proposed in chapter 3. The reason is for convenient of prototype fabrication. The size of the tank inner, will be defined as fluid field as computing domain, is 420mm*130mm*100mm. That keeps match with experiment condition.

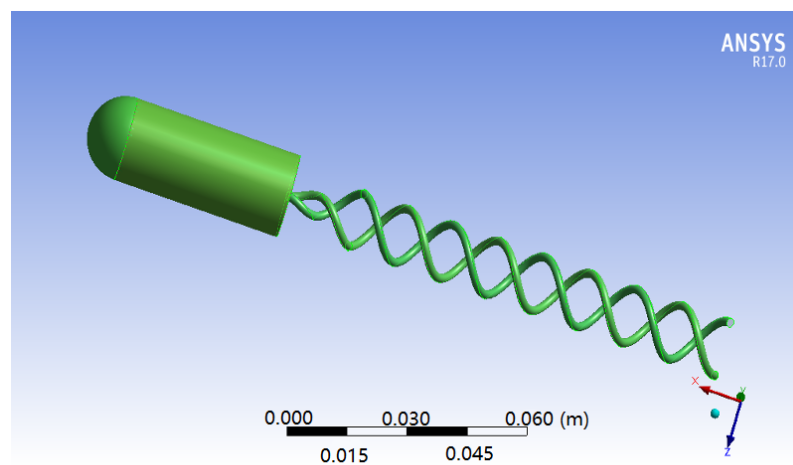


Fig. 4.4 Case1-Geometry of robot

Meshing

Mesh quality has a big impact on computational accuracy and stability. It determines the precision and convergence for numerical simulation.

The parts of the body have mixed mesh method — half-sphere part has triangle mesh and the cylinder part has rectangle mesh. The tails' mesh method is mainly rectangle mesh. The whole view of robot meshing is shown in Fig. 4.5.

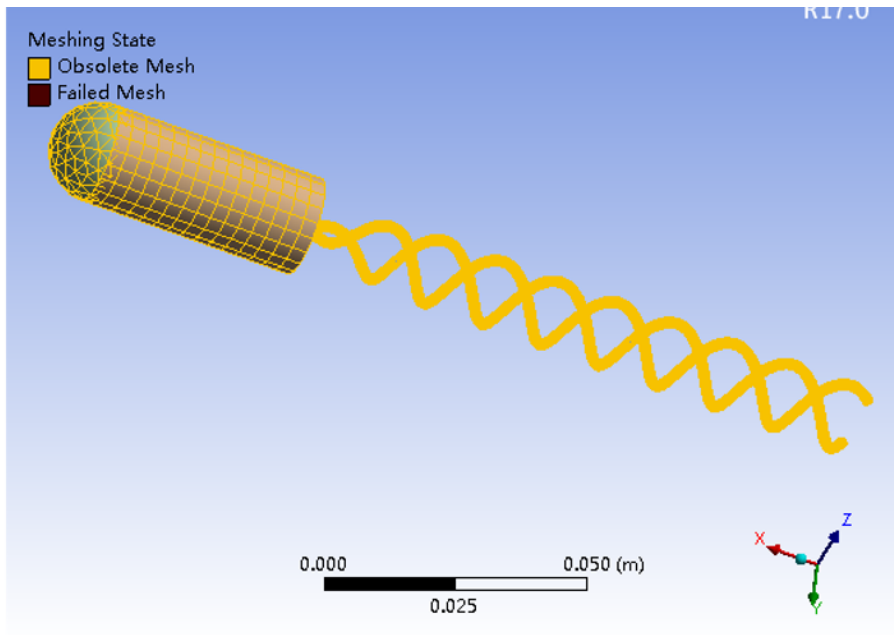


Fig. 4.5 Case1-Meshing

The details of body meshing are shown in Fig. 4.6.

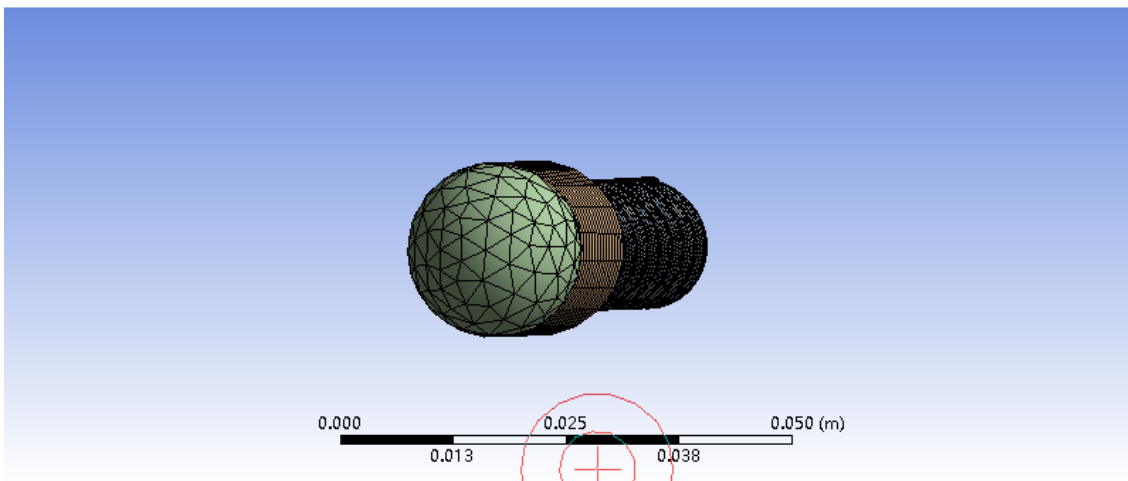


Fig. 4.6 Case1-Meshing of Body

From the graphic, it is clear that the mesh of the forwarding part of the body has a triangle mesh design and is a typical low-density mesh.

The details of tails meshing are shown in Fig. 4.7.

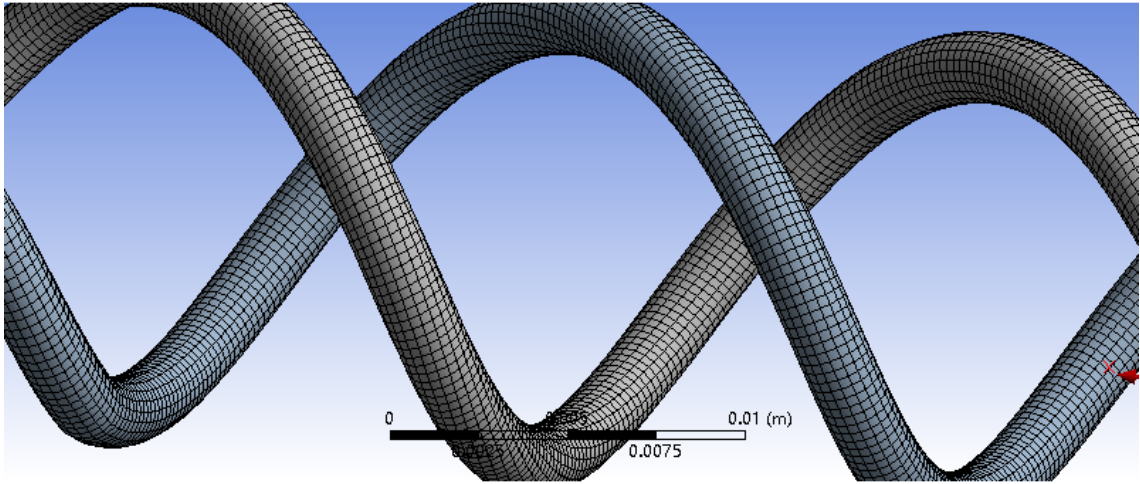


Fig. 4.7 Case1-Meshing of tails

The properties of the meshing are:

- Size function: Curvature
- Smoothing: Medium
- Transition: Slow
- Statistics
- Nodes: 96,977
- Elements: 221,226

4.2.3 Solve

In this stage, the problem is solved using a calculation. This stage is completed by ANSYS/Fluent in this research. Firstly, the solve condition is set up to ensure the goal to be achieved. This includes mesh verification, scale check solver type and time setting. Solver models selection and setup, materials setup, cell zone conditions setup, boundary conditions set up and most importantly, the dynamic mesh setup. After the setup is complete and checked, the calculation can be run and the results are presented in the next stage.

Mesh Verification

Mesh Checking

Domain Extents:

x-coordinate: min (m) = -6.992660e-02, max (m) = 1.356141e-02

y-coordinate: min (m) = -4.841284e-03, max (m) = 4.841284e-03

z-coordinate: min (m) = -4.841284e-03, max (m) = 4.841282e-03

Volume statistics:

minimum volume (m3): 2.033570e-13

maximum volume (m3): 2.718876e-09

total volume (m3): 2.159375e-06

Face area statistics:

minimum face area (m2): 2.126336e-09

maximum face area (m2): 2.184124e-06

Mesh Quality Minimum Orthogonal Quality = 3.47779e-01 (Orthogonal Quality ranges from 0 to 1, where values close to 0 correspond to low quality.)

Maximum Ortho Skew = 5.60727e-01 (Ortho Skew ranges from 0 to 1, where values close to 1 correspond to low quality.)

Maximum Aspect Ratio = 1.10557e+01

It seems acceptable.

The solver type is set as pressure-based and the time is set as transient. As the mass of robot can be adjusted to keep balance with buoyancy force it received, the gravity can be ignored.

Solver model selection

The solver model is set to Low-Re number k-epsilon model.

Model constants:

Cmu: 0.09

C1-Epsilon: 1.44

C2-Epsilon: 1.92

TKE Prandtl Number: 1

TKR prandtl Number: 1.3

Table 4.1 Case1-Silicon Oil selection

Viscosity (25°CSt)	dielectric con- stant	Flash point (°C)	Density ratio	Inter-facial tension (dyn/cm)
10	2.65	155	0.930~0.940	20.1
20	2.68	250	0.945~0.955	20.6
50	2.70	270	0.950~0.960	20.9
100	2.70	300	0.960~0.970	21.0
300	2.72	300	0.965~0.975	20.1
500	2.75	300	0.965~0.975	21.1
1000	2.76	300	0.965~0.976	21.2
2000	2.80	300	0.970~0.975	21.2

Materials

Fluid: silicon-oil

chemical formula: $(\text{CH}_3)_3\text{SiO}[(\text{CH}_3)_2\text{SiO}]_n\text{-Si}(\text{CH}_3)_3$

Physical characteristics: Show in Table. 4.1 (red is selected type of silicon oil)

Solid: aluminium

Density: 2719 kg/m³

Cell Zone Condition

Zone: Tail1—solid

id: 11 mesh motion—rotation axis direction:X

Tail2—solid

id: 12 mesh motion—rotation axis direction:X

Head sphere—solid

id:15 mesh motion—rotation axis direction:X

Head cylinder—solid

id :13 mesh motion—rotation axis direction:X

Tank—fluid

id:14

Boundary Condition and Dynamic Mesh

Dynamic mesh methods are smoothing and re-meshing. To calculate velocity, one of the goals of this simulation, the option of six DOF is selected. The over-set mesh is used. The

over-set mesh is good for “Transient Flow with Rigid Body Motion”, and is supported by ANSYS fluent 17. Over-set meshing technology extends current capabilities.

It can handle relative mesh motion with small gaps (gears, pumps) in a better way. The setting is more natural than the re-meshing method. It also exhibits simplified mesh generation for complex geometries and avoids re-meshing failures and setup issues as in dynamic mesh.

Overset interface in this case:

component grids—the swimmer: Tail1, Tail2, Head sphere, Head cylinder

Background grids—the calculate domain: tank

4.2.4 Post processing

In this section, the results are presented using graphics, plots and reports. The main goal of the simulation, the velocity of the robot, can be achieved and explained.

The contours of pressure are shown in Fig. 4.8. The pressures on robot forward body and forward side of tails are the highest and the pressures on the backside of body and tails are the lowest. The reason for the low pressure is that the separation of the boundary layer occurs in these places, resulting in increased velocity and reduced pressure.

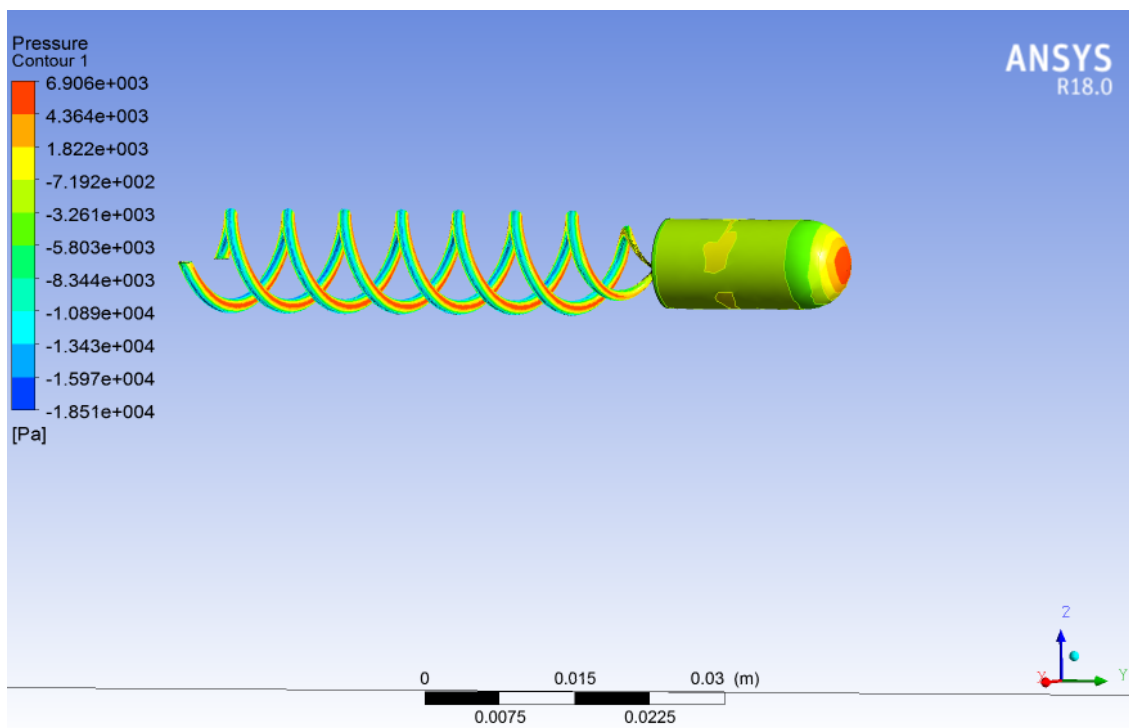


Fig. 4.8 Case1-Contours of Pressure

Contours of the density of this case are shown in Fig. 4.9

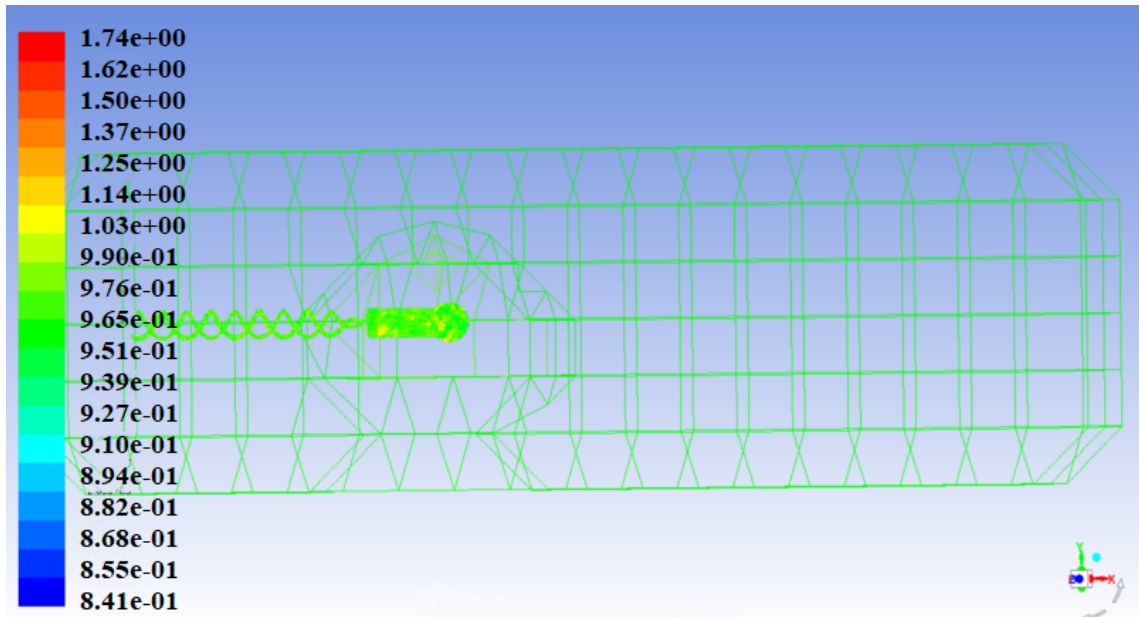


Fig. 4.9 Case1-Contours of Density

From Fig. 4.9, it is clear that the density of computing domain is almost evenly distributed. The density only changes around the robot body part. A sphere formed around robot body may decrease the resistive force for the robot movement.

Contours of kinetic energy are depicted in Fig. 4.10

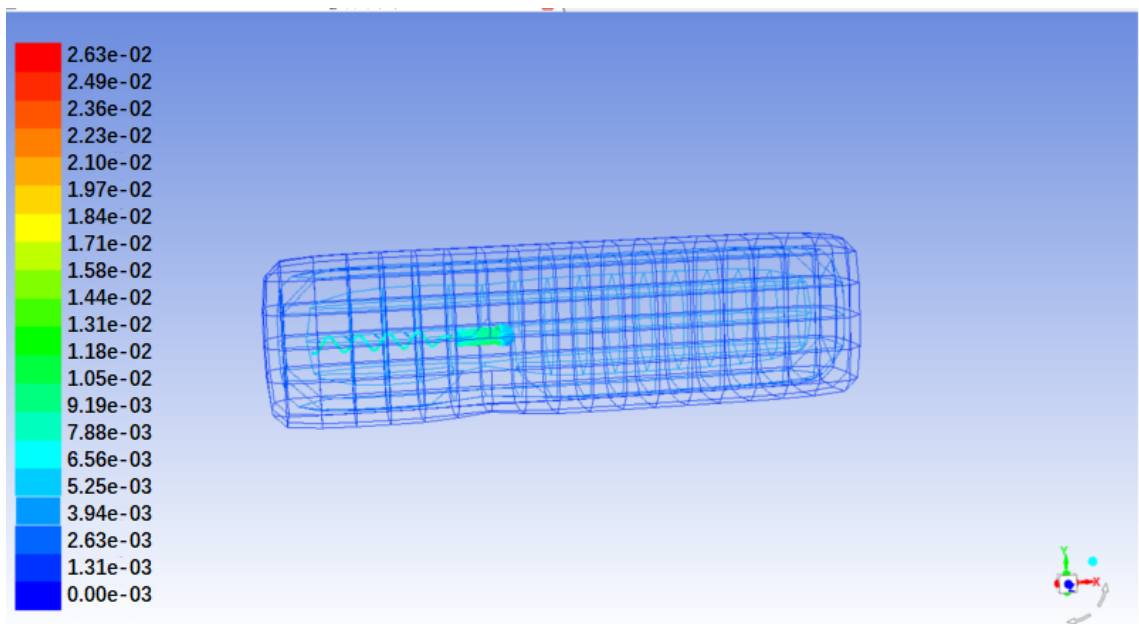


Fig. 4.10 Case1-Contours of Kinetic Energy

Fig. 4.10 shows that the kinetic energy is kept at a low level for the whole computing domain. The whole robot has higher kinetic energy. An interesting point is that the robot body, tails and the moving path are covered by a small higher kinetic area.

The velocity vectors from different perspectives are shown in Fig. 4.11, 4.12, 4.13, 4.14. The highest velocity of the flow field is achieved at the backside of the tails. That part is also the propulsion force generation place. The stable velocity of robot achieved at 4.7 second and the final velocity is 84mm/s.

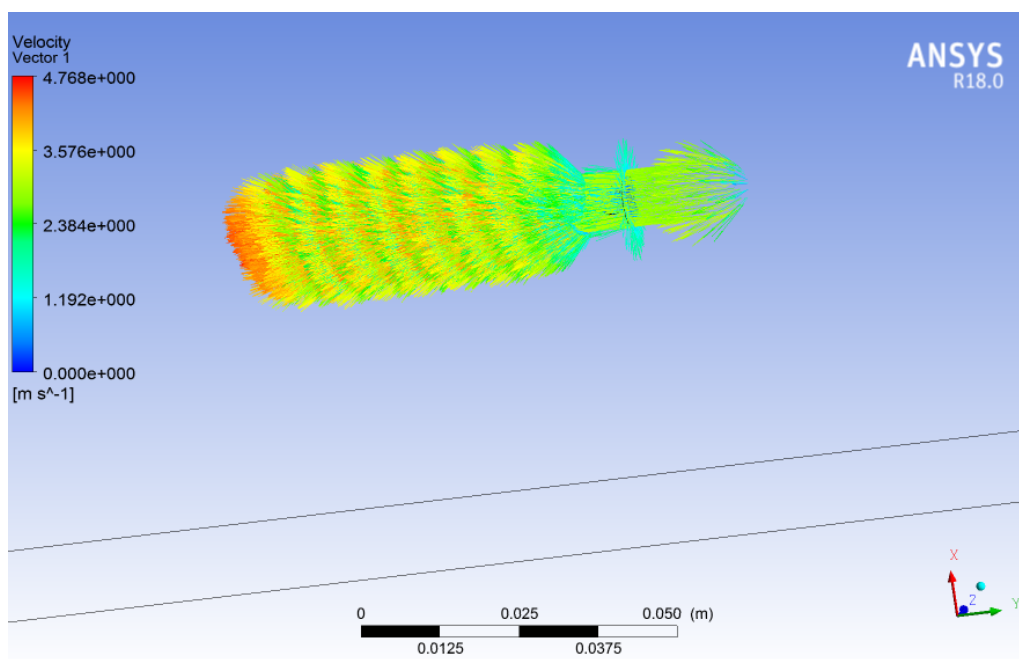


Fig. 4.11 Case1-Velocity Vector 1

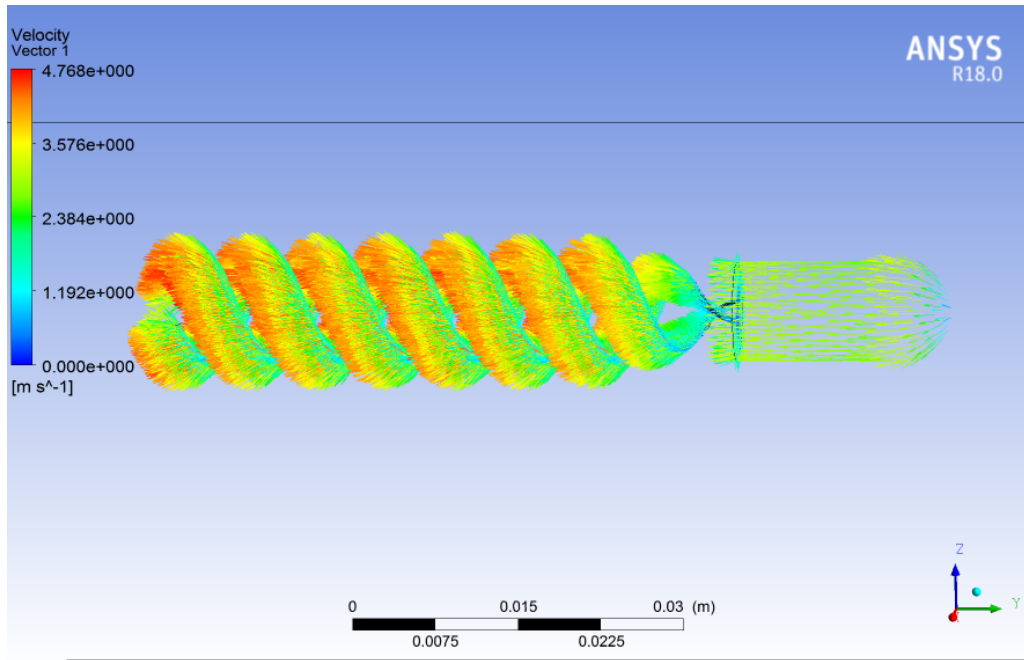


Fig. 4.12 Case1-Velocity Vector 2

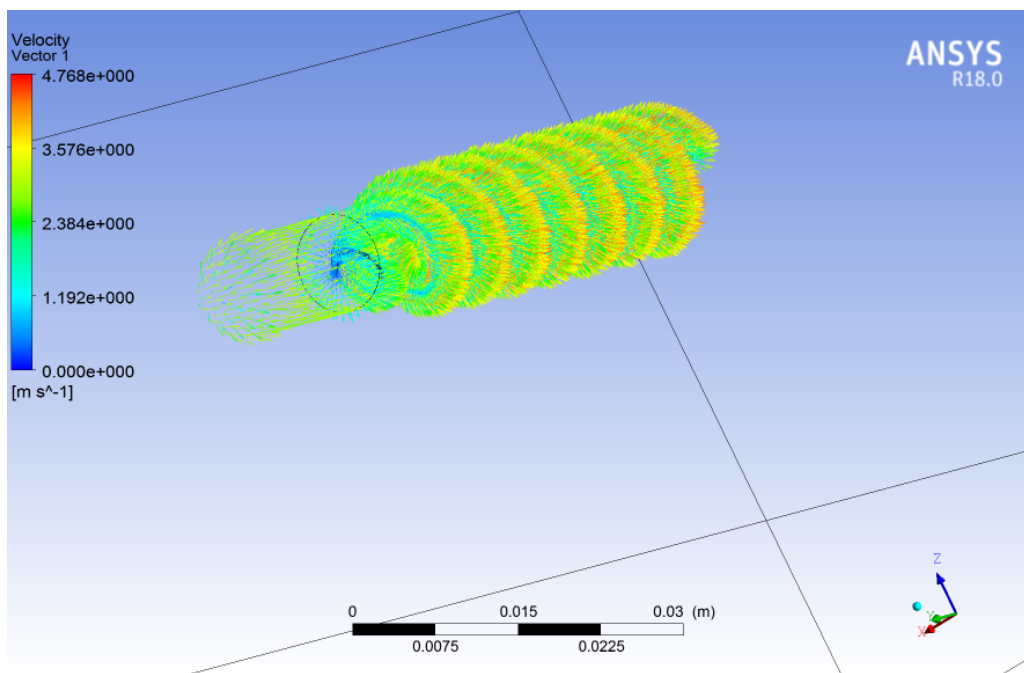


Fig. 4.13 Case1-Velocity Vector 3

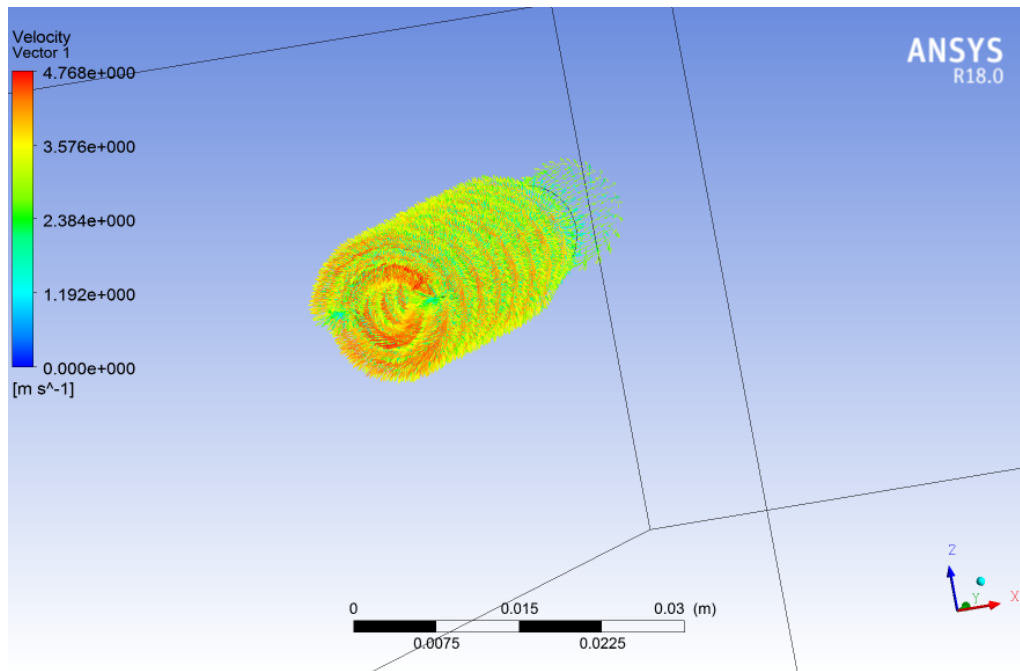


Fig. 4.14 Case1-Velocity Vector 4

4.2.5 Results and analysis

When the swimming robot is working, its surrounding liquid environment is bound to affect its movement. Therefore, this section discusses the effect of the the robot's operating environment on its motion characteristics, and focus on the relationship between the speed of the moving robot and the density and viscosity parameters of the liquid.

When the simulation parameters are set, it is assumed that the helix tail drives the swimming robot movement at a rotational speed of 2200r / min, and the density and dynamic viscosity coefficients of the fluid are in the range of 110^3kg/m^3 — — 1.210^3kg/m^3 and 0.001Pas 0.01Pas . Thus, the simulation results are shown in Fig.4.15 and Fig.4.16.

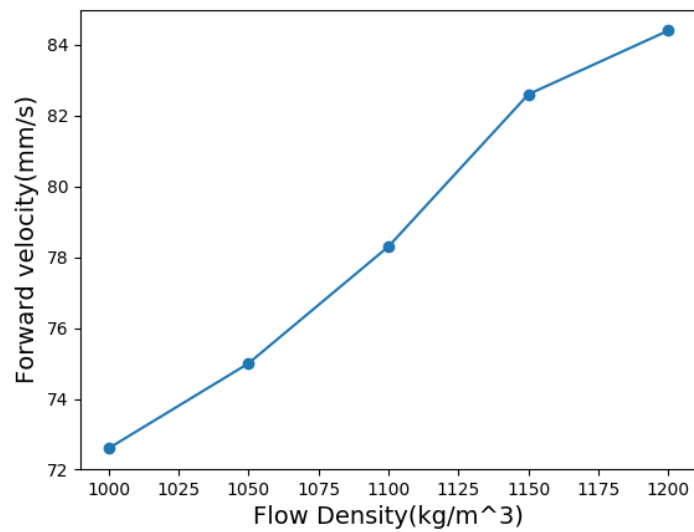


Fig. 4.15 The relationship between velocity and density

Fig.4.15 shows the variation of the velocity of the moving robot with the liquid density ρ . It can be seen from the figure that the straight speed of the robot is linearly related to the density of the liquid medium, and as the density increases, the speed is also increasing. This is different from the swimming of the bacteria in the low Reynolds number environment, which is not affected by the density of the surrounding environment according to the microfluid dynamics described in Chapter 2.

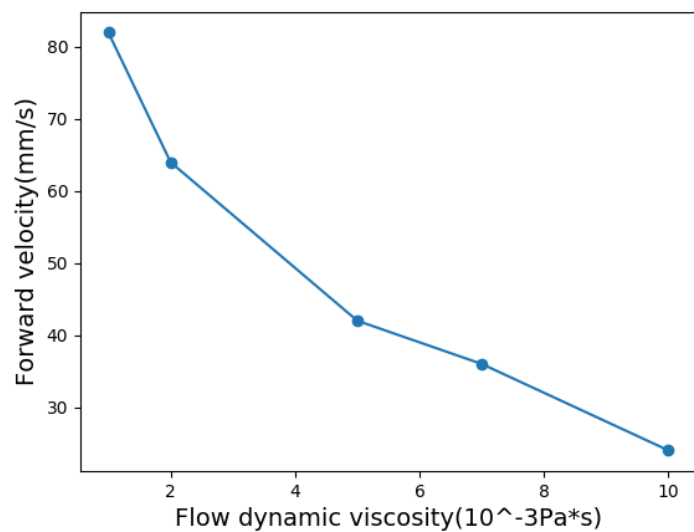


Fig. 4.16 The relationship between velocity and viscosity

Fig.4.16 shows the effect of the hydrodynamic viscosity coefficient μ on the velocity of the swimming robot. It can be seen from the figure that the straight speed of the robot decreases with the increase of the dynamic viscosity coefficient. The propulsion of the spiral tail increases with the increase of the liquid dynamic viscosity coefficient μ , and it is speculated that the increase of the liquid viscosity leads to the increase of the viscosity of the spiral tail. The resistance of the fuselage and the increase of the tail thrust, and the effect of viscosity on the resistance is more significant. To prove this hypothesis, this thesis simulates the motion of four kinds of body-sized swimming robots in different viscosity coefficient liquids, and obtains the simulation results shown in Fig.4.17.

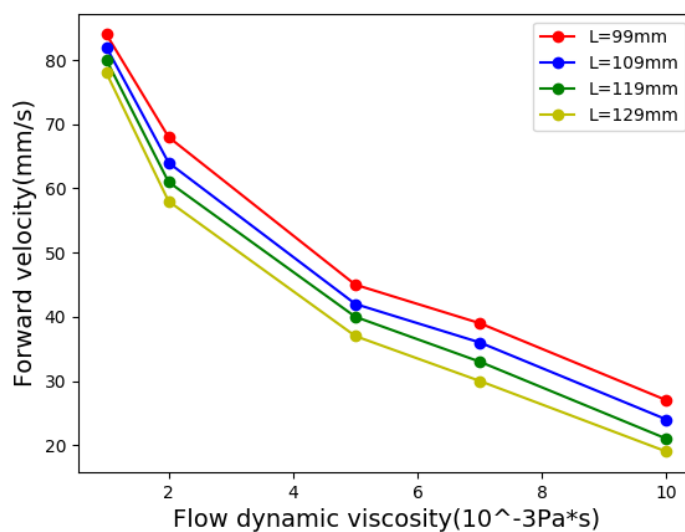


Fig. 4.17 The relationship between velocity and Body-size

Fig.4.17 shows four curves of the body when the axial length of 99mm, 109mm, 119mm, and 129mm, the swimming robot's straight speed with the dynamic viscosity coefficient μ changes. It can be seen from Fig.4.17 that when the robot moves in the same viscosity liquid, the smaller fuselage size robot has faster straight-line velocity. It indicating that the force applied by the fluid is decreasing. From another perspective, straightening speed is getting smaller when the liquid viscosity increases; and the speed is slower when the axial length of the fuselage is bigger. It indicating that the effect of the reduction of the movement is more obvious when the robot body has greater size. It proved the speculation above.

4.2.6 Optimisation Based on Simulation Results

In the case of resistance, the length of the short axis should be as small as possible in the optimisation scheme. The body length of the robot also needs to be as small as possible.

However, too small body length will inevitably lead to the body of the volume of the components difficult to load and layout.

It can be seen from Fig. 4.8 that the pressure on the advance side is larger, because of the tail of the spiral radius is greater than the body part of the cylindrical radius, the pressure on the tail is significant high, it leads to increased resistance accordingly. Furthermore, the pressure on the body is high just at the centre of the advancing side. The reason should be that the spherical shape can reduce the advancing pressure. So, the radius of the cylinder in the body part should be greater than the radius of the tail helix for optimisation, and the length of the helix tail should be shortened accordingly.

It can be seen from Fig. 4.9 that the robot forms a lower density area around the body when swimming. This phenomenon is conducive to reducing the resistance when the robot is moving forward. At the same time, it can be noted that the region of lower density quickly disappears at the end of the body. In the optimisation scheme, it should be considered to shorten the length and size of the helix tail. To make surrounding fluid density smoother, the end side of the body needs to make smaller.

Considering the above factors of shape optimisation and the size of the robot components, the proposed optimisation scheme is shown in Fig. 4.18 and Fig. 4.19.

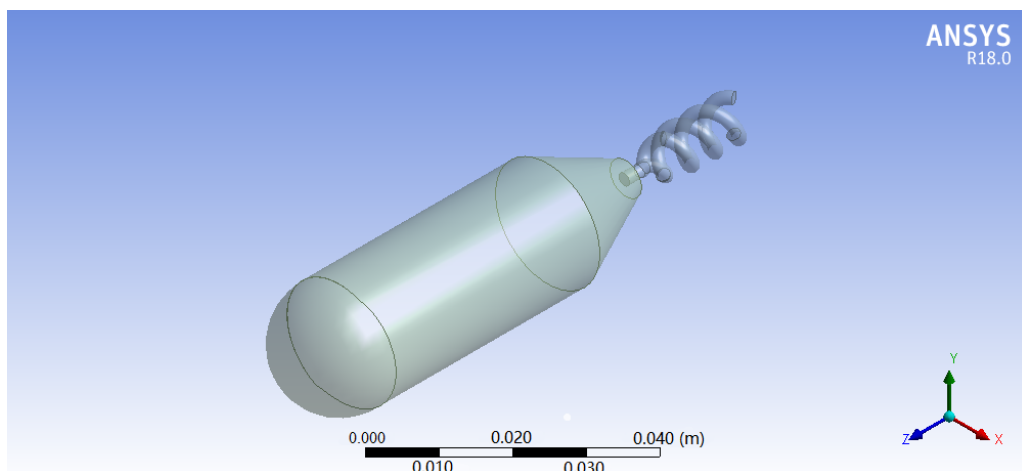


Fig. 4.18 optimised Model

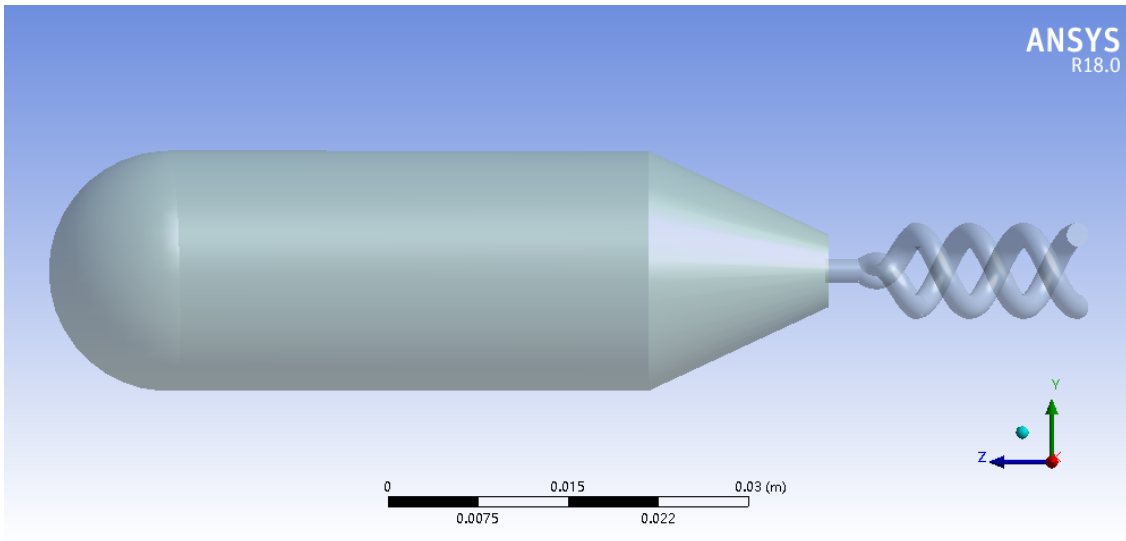


Fig. 4.19 The right-side view of the optimised Model

A simulation is conducted based on the optimised model. It utilises the FSI method to calculate the interaction between the solid robot and the fluid. The 3D model is built together for solid robot and fluid domain as shown in Fig. 4.20. After that, the fluid part is set up for mesh, solution method, material, cell zone, boundary condition, dynamic mesh, initial condition and calculation is executed.

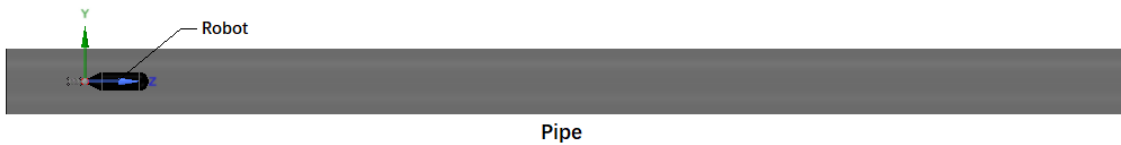


Fig. 4.20 The proportion of the optimised model and Pipe

For mesh part shown in Fig. 4.21, firstly the solid part need to be suppressed. The tetrahedral mesh is employed, and the mesh size is set to 0.1mm. Each part of the mesh needs to be named for a dynamic mesh.

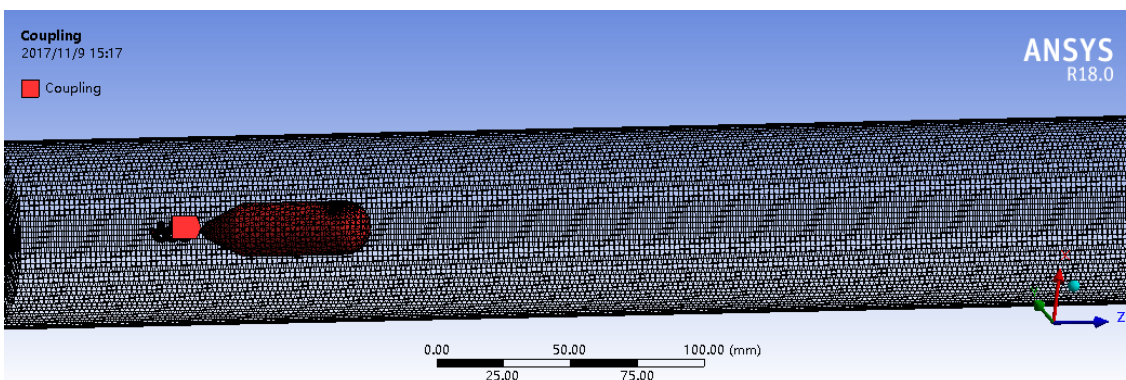


Fig. 4.21 The optimised Mesh in Pipe

For solution method part, the low-Reynolds number viscous flow model is selected.

For the material part, a kind of silicon oil is copied from the material database and modified according to the physical properties of the silicone oil used in the experiment.

For cell zone part, the material is assigned to the proper fluid domain.

For the boundary condition part, each of fluid boundary is configured.

For dynamic mesh part, firstly the dynamic categories are specified. Smoothing method and re-meshing methods are employed. Then the dynamic mesh zones are created and allocated. The most important part is the system coupling interface.

For initial condition, a series of parameters are allocated. The initial condition is set to coupling mesh.

For the calculation part, the time step is set to 0.01s, and the count of steps is set to 500. This means that the total simulation time is 5 seconds. The monitor of residuals is set to $0.1e-5$. The minimal number of iteration is set to 100.

After setting up the fluid part, the calculation can not be executed at this stage. The solid part needs to be set up.

In the solid part, the transient structure is employed. The setting includes Engineering data, Model and Setup.

In Engineering data, the material of PMMA Polymethylmethacrylate(PMMA) is set. The geometry is based on the previous shared 3D model.

In Model setting, the fluid part is suppressed, and the connection interface is deleted too. The solid-fluid interface is created according to the coupling mesh set up in a fluid dynamic mesh.

In the setup part, the transient model is selected. The length of time steps and count of steps is set. Some solution results such as equivalent stress, total deformation and directional velocity need to be created.

Finally, both fluid and solid setup are connected to system coupling setup. Firstly, the data transfer needs to be created from the interface of fluid and solid. A series of parameters need to be confirmed in the analysis setting. Another important setting is the execution control.

After setting up all three parts of the simulation, the calculation can be executed. The results are shown in Fig. 4.22 and Fig. 4.23. The solution is carefully adjusted to the parameters of dynamic mesh and another setting.

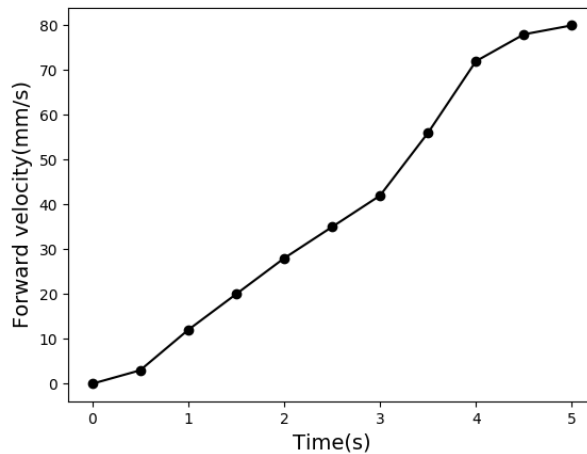


Fig. 4.22 v-t curve for the optimised model

From Fig. 4.22, it can be seen that the forward velocity is rising rapidly from 0.5 seconds, and at a faster rate from 3 seconds. The velocity achieves a stable situation around 5 seconds. The conditions of this V-t curve includes the density of the fluid is $1200\text{kg}/\text{m}^3$; the dynamic viscosity of flow is $1 \times 10^{-3}\text{pa} \cdot \text{S}$; the robot body length is 90mm; the rotation speed of robot tails is 2200 r/s.

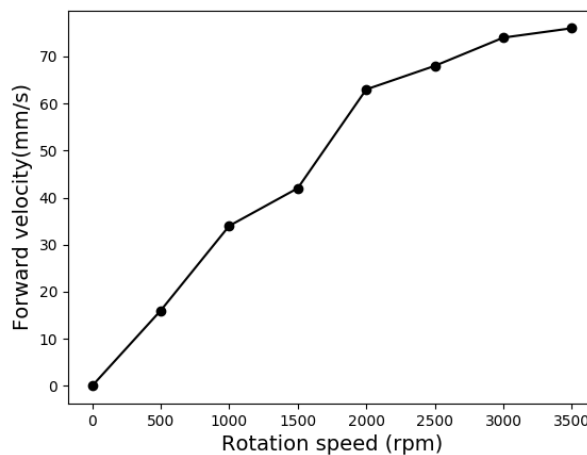


Fig. 4.23 The relationship between velocity and rotation speed for optimised model

Fig. 4.23 shows the velocity variation trend as a function of the rotation speed change. The curve is to keep a parabola shape approximately. The forward velocity rises as the rotation speed increases. It means higher rotation speed generates higher propulsion which leads to acceleration i.e. rise in the velocity. The higher velocity meets the higher resistance force. When the forces achieve a balance, the robot experiences a stable velocity.

4.3 Simulation case 2-human blood vessel robot

4.3.1 Hydrodynamic analysis of blood vessels

Mechanical properties of blood vessels

The blood circulation system is responsible for transporting oxygen and nutrients in the human body. It includes pulmonary and systemic circulation. As shown in the figure 4.24, the blood flows from the right ventricle through the pulmonary artery, pulmonary capillaries and pulmonary veins, the left atrium into the left ventricle, this circuit is for the pulmonary circulation. Blood from the left ventricular outflow through the aorta, capillaries and finally into the right ventricle through vena-cava; the loop is called the systemic circulation. It can be seen from the figure 4.24 that arteries, veins and capillaries make up the entire blood circulation system, and the blood vessels are the channels of the human blood circulatory system.

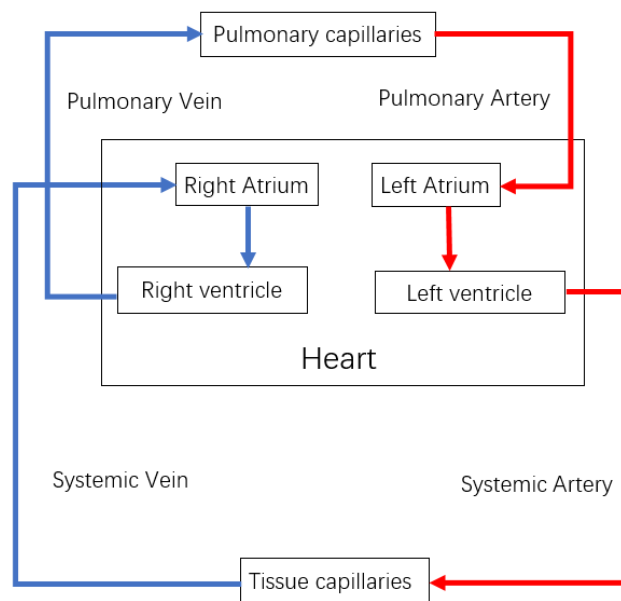


Fig. 4.24 Human blood circulation system

Vascular is a flexible pipeline, the entire blood vessels throughout the body is a complex pipeline network with a lot of bifurcation network system. The venous environment is simpler than arteries and is similar to the industrial pipelines. Due to the low Reynolds number movement during the robot operation, the relative motion can be used to study the effect of flow force. The robot structure design and operation control should be based on the aortic environmental parameters. Because the arterial flow field is more complex than the venous environment. An artery robot certainly can adapt to the venous environment, and vice versa is uncertain.

The arterial wall is not a strict elastomer, but a viscoelastic body. But because of the large proportion of elastic fibres in the vessel wall of the thoracic aortic segment, it can be assumed that the tube wall is Isotropic Hook elastomers. The artery undergoes periodic deformation by external forces, causing blood to flow in the axial direction of the vessel. The pulsation waveform of the variation of the blood vessel radius and the pressure pulsation waveform are isomorphic and synchronous.

Blood vessels are hollow tubes with lumen diameters from a few microns to a dozen millimetres, filled with or flowing or stationary liquid medium. Blood vessels include arteries, capillaries, and veins, where the inner diameter of the aorta is reachable, and the inner diameter of the venous blood vessels is about the inner diameter of the capillaries. The table 4.2 gives reference data on the diameter of the human blood vessel and the total cross-sectional area.

Table 4.2 The reference of human vessel diameter and cross section area

Vessel	Inner Diameter	Total Cross Section Area (cm^2)
Aorta	2.5 cm	4.5
artery	0.4 cm	20
Arteriole	30 μm	400
Capillaries	6 μm	4500
Venule	20 μm	4000
Vein	0.5 cm	40

Vascular is composed of multi-layer composite structure, including three kinds of material: elastic fibres, collagen fibres and smooth muscle, they all have certain viscoelasticity. For interventional treatment robots, the main application environment is human aortic blood vessels. Arterial blood vessels are viscoelastic. The pressure in the wind vessel changes with the pressure in the tube, so the arterial blood vessels have compliance. The blood flow and the arterial blood vessels are coupled with each other.

Rheological properties of blood

Blood is composed of blood plasma, as well as tangible elements including red blood cells (RBC) averaging about the total volume, white blood cells (WBC) not exceeding the total volume of the tangible components, platelets not exceeding the total volume of the tangible components. Blood is a viscoelastic non-Newtonian fluid medium, a working medium in the cardiovascular system, and the primary environment in which robots operate.

Normally, plasma is Newtonian fluid and its viscosity is independent of the shear rate. The apparent viscosity of the blood increases with the gradual increase of erythrocyte hema-

to crit; when the pressure is more than 10%, the blood shows significant non-Newtonian characteristics.

In the blood flow of large blood vessels e.g. aorta, the shear rates of blood flow in other blood vessels are all higher than $50s^{-1}$ except vena-cava blood flow. The blood exhibits the characteristics of a Newtonian fluid, at the same time the viscosity of the blood stays stable. Therefore, except vena-cava blood flow, physiological blood flow in the macrovascular can generally be treated as a homogeneous, incompressible Newtonian fluid. Furthermore, the flow of blood in the artery is assumed to be asymmetric laminar flow.

Pulsatile flow generation

The human heart has four elastic chambers i.e. left atrium (C), left ventricle (D), right atrium (A), right ventricle (B) as shown in Fig. 4.25. During myocardial relaxation, the ventricles or atrial diastole and expansion of the heart chamber reduces intracardiac blood pressure, hence, blood flows from the vein into the heart. During myocardial contraction i.e. atrial or ventricular contraction, increased pressure makes the heart cavity to pump out blood. The mechanism of heart contraction and relaxation is known as the heart-beat. Heart-beat is the driving force of the blood circulation. Cardiac diastolic contraction activity of a time called the cardiac cycle.

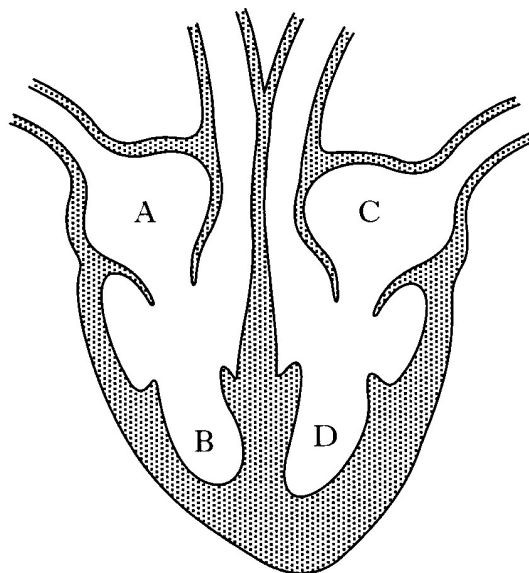


Fig. 4.25 Human Heart Diagram

When the heart is pumping blood out of the systole, the pressure in the blood vessel increases. When the heart stops pumping blood, the pressure of the blood vessel decreases. The blood vessel wall is elastic and moves with the blood vessel internal pressure changes

and deformations. When the blood pressure rises, the blood vessel wall expands to the outside. When the blood pressure decreases, the blood vessel wall rebounds to the original position. The blood pumping operation in the heart is cyclical, so the blood flow inside the blood vessel is also periodic. During ventricular contraction, the atrioventricular valve is closed, the aortic valve is opened. When the ventricle is dilated, the atrioventricular valve is opened, the aortic valve is closed to allow blood flowing from atrium to ventricle. However, the blood flow in the blood vessels is always continuous. This is because part of the blood that enters the aorta from the ventricle enters the venous cavity directly through the arterial and capillaries. When the ventricle is dilated and the heart stops pumping into the aorta, the blood is stored in the aorta which continues to flow forward under the elastic restoring force of the aorta and the aorta wall. The aortic wall elasticity ensures that the blood pressure will not be too high during the ventricular contraction while allowing the ventricular diastolic blood flow.

For aortic vessels, the length of the vessel depends on the length of the inlet segment. Within the entrance section, the blood flow velocity profile gradually changes until it reaches a certain length, and the velocity profile tends to be stable. This distance is called the inlet length (L_1) which is shown in Fig. 4.26.

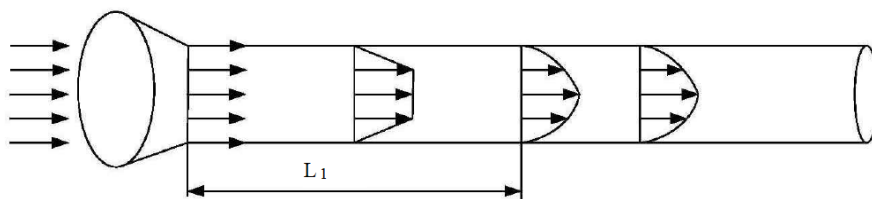


Fig. 4.26 schematic diagram of inlet length

4.3.2 Problem Identification

Human vascular robots run in the blood vessels. On one hand, the robot is restrained by the wall and on the other hand, it is impacted by the blood flow in the blood vessels. Therefore, it is necessary to study the mechanical properties of the blood vessel wall and blood.

The mobile robot system is operated in a fluid-filled environment in which the medium flow field is coupled to the lumen itself. The movement of the robot in the lumen is also affected by the flow field and the wall, and there is a coupling relationship between the three movements. So, the lumen environment factor becomes a very important part of the robot design and control. Due to the physical properties of the biological lumen environment, lumen geometry is very complex. Depending on the specific problem, some properties need to be selected to ensure the accuracy of the main parameters.

Goals Definition

When a robot swimming through the fluid, the flow field undergoes a stable change to drastic and then change back to a stable process. To ensure the flow at the inlet and outlet are stable, the calculation area of the robot is taken as the length of the cylindrical area. The flow area around the robot adopts the unstructured grid with strong adaptability and deformation ability, and the rest area utilises structural grid. This can save the grid generation time and reduce the number of grids. The grid can also reflect the trend of changing the flow field in the domain.

The basic calculation method used in this case is Semi-Implicit Method for Pressure Linked Equations (SIMPLE) method with speed and pressure as the basic solution variables. The calculation area is divided into blood flow, vascular wall, aortic inlet, aortic outlet, robot front, robot tail and other regions, respectively, given the boundary conditions and the initial conditions.

Domain Identification

Firstly, the fluid domain needs to be identified. The fluid domain is built so that it has the same properties as the main vessel environment for human. The fluid domain is set to a cylinder where the diameter is $100 \mu m$. The longitude of the domain is $600 \mu m$. The solid domain is presented in section 4.3.3 Geometry. The time-domain set to 1 second.

4.3.3 Pre-processing

Geometry

The geometry of the swimmer is shown as follows: * Shape parameters:

Body (Ellipsoid)

Length: $2.5 \mu m$

Diameter: $1.25 \mu m$

Connection (Conical helix)

Amplitude: $0 - - - 0.625 \mu m$

length: $1.6 \mu m$

Radius: $0.1 \mu m$

Flagella (Cylindrical helix)

Amplitude: $1.3 \mu m$

Pitch: $2.4\mu m$

Length: $9.6\mu m$

Parameters Setting

* Simulation parameters:

Flagella Rotational speed: 200 rps

Gravity of flagella: $9.5 \times 10^{-2} pN$

Gravity of body: $12 \times 10^{-2} pN$

Fluid density: $0.998203 g/cm^3$

Fluid viscosity: $1.0087 \times 10^{-3} Pa \cdot s$

Time-step: $2.4 \times 10^{-7} sec$

Meshing

* Physical appearance and meshing as shown in Fig. 4.27

This model consists of a body and two-centre symmetrical flagella components. The flagella are assumed to be connected with the body by conical helix with the same radius. In this simulation, the connection part is ignored for the simplification of the calculation. The effect to the final velocity from the connection part is very small. It is assumed that the body and the flagella are connected although the connection part is not calculated.



Fig. 4.27 Physical appearance and meshing

4.3.4 Solve

At this stage, the calculation is executed conducted with a selected solver. This stage is completed by ANSYS/Fluent in this research.

Mesh Verification

Mesh Checking

Domain Extents:

x-coordinate: min (m) = $-5.998182e-06$, max (m) = $5.998182e-06$

y-coordinate: min (m) = $-2.700000e-04$, max (m) = $3.000000e-05$

z-coordinate: min (m) = $-6.000001e-06$, max (m) = $6.000001e-06$

Volume statistics:

minimum volume (m3): $4.908309e-24$

maximum volume (m3): $3.487345e-19$

total volume (m3): $3.389970e-14$

Face area statistics:

minimum face area (m2): $4.764592e-16$

maximum face area (m2): $1.228208e-12$

Mesh Quality Minimum Orthogonal Quality = $7.83395e-01$ (Orthogonal Quality ranges from 0 to 1, where values close to 0 correspond to low quality.)

Maximum Aspect Ratio = $6.28707e+01$

Maximum Ortho Skew = $5.60727e-01$ (Ortho Skew ranges from 0 to 1, where values close to 1 correspond to low quality.)

It seems acceptable.

The solver type is set as pressure-based and the time is set as transient. As the mass of the robot can be adjusted to keep balance with buoyancy force is received, the gravity can be ignored.

Solver model selection

The solver model was selected as Low-Re number k-epsilon model.

Model constants:

Cmu: 0.09

C1-Epsilon: 1.44

C2-Epsilon: 1.92

TKE Prandtl Number: 1

TKR prandtl Number: 1.3

Materials

Fluid: Set the blood as an incompressible and uniform Newtonian viscous fluid, the viscosity coefficient $\mu = 0.0035 Pa \cdot s$, the density $\rho = 1.05 \times 10^3 kg/m^3$ (Human blood measured at normal body temperature), the discussion in this the article is confined to the context of macrovascular.

Solid: aluminium

Density: 2719 kg/m³

Cell Zone Condition

Zone: Tail1—solid

id: 2 mesh motion—rotation axis direction:X

Tail2—solid

id: 3 mesh motion—rotation axis direction:X

Head sphere—solid

id:4 mesh motion—rotation axis direction:X

Head cylinder—solid

id :5 mesh motion—rotation axis direction:X

Pipe—fluid

id:6

Boundary Condition and Dynamic Mesh

The methods of smoothing and re-meshing are employed for the dynamic mesh. The option of six DOF is selected and overset mesh is used.

Overset interface in this case:

component mesh—the swimmer: Tail1, Tail2, Head sphere, Head cylinder

Background mesh—the calculate domain: human vessel

4.3.5 Post processing

Results

* Flow field velocity vector

The velocity vectors are coloured by velocity magnitude. The flow field situation at time 2.9374×10^{-1} .

The rotating flagella cause a flow of fluid around them. A two-dimensional projection of the fluid flow in a plane parallel to the flagella axis is shown in Fig. 4.28.

From the result, it is can be found that the fastest velocity of flow is around the flagella, and then the velocity decreases gradually.

The forward motion of the flagella can be seen by the motion representation of the fluid because there is a flow that coincides with the helical tangent. It is can be seen that there is a fluid motion region, in which the fluid move in the cross direction and roughly be consistent with the shape of the spiral.

The forward motion of the flagellum is apparent and is also indicated by the fluid motion since there is flow coincident with the helix tangent. The figure 4.28 also shows regions of fluid rotation in alternating directions that approximately coincide with the helix shape.

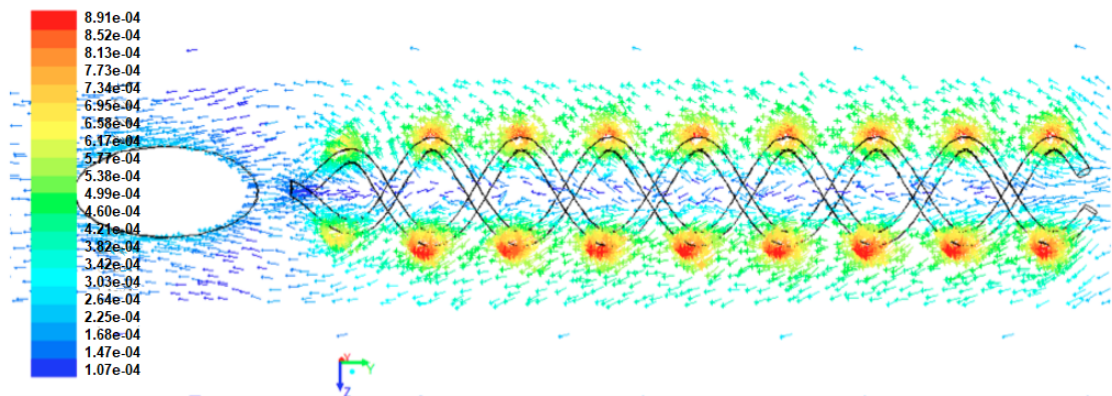


Fig. 4.28 Case2- velocity vector

* Flow lines around the swimmer is shown in Fig. 4.29. Path-line coloured by particular ID. The time is 2.9374×10^{-1} .

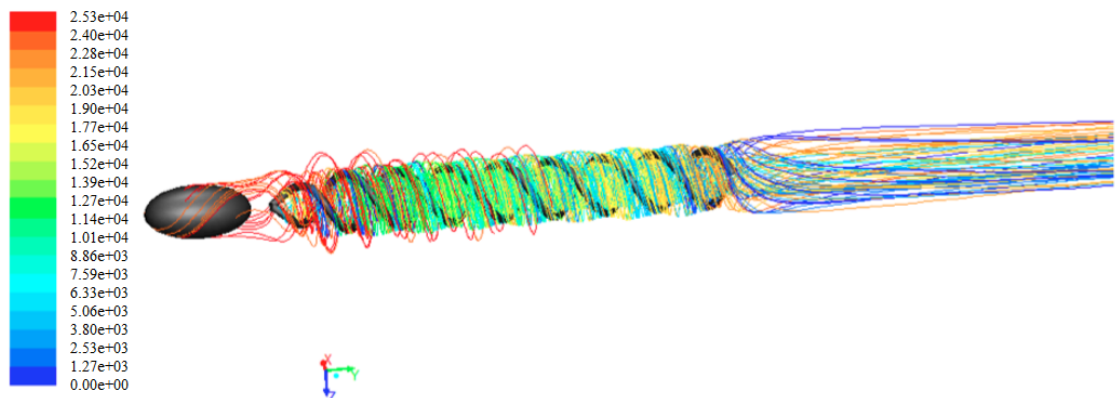


Fig. 4.29 Flow lines around the swimmer

* Flow field vectors around the body Flow field vectors around body showing Fig.4.30. The velocity vectors are coloured by velocity magnitude. The time is 3.2315×10^{-1} seconds.

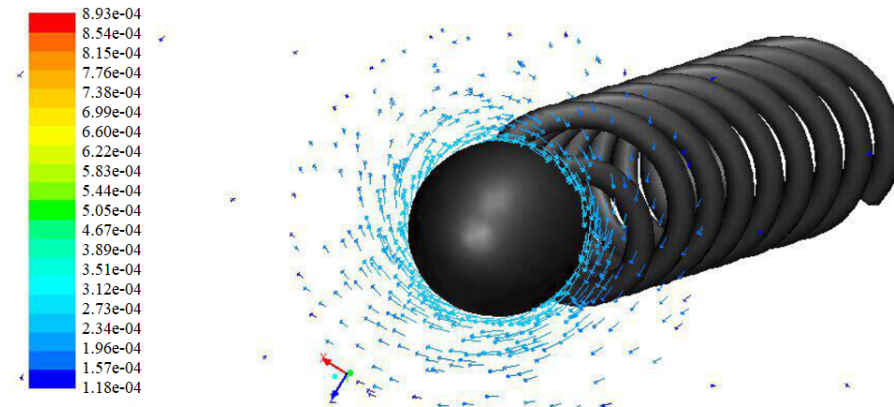


Fig. 4.30 Flow field vectors around body

The Flowfield vectors around flagella are shown in Fig.4.31

The velocity vectors are coloured by velocity magnitude. The time is 3.2315×10^{-1} .

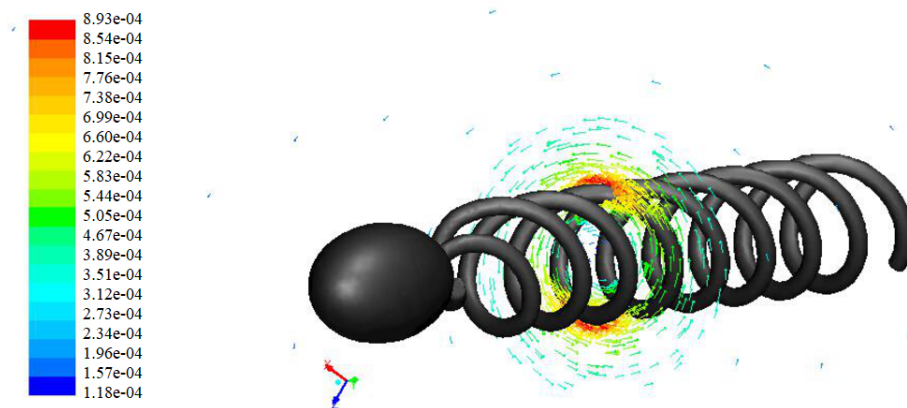


Fig. 4.31 Flow field vectors around flagella

The velocity of the system is around $195 \mu\text{m}/\text{s}$, it is significantly faster than previous research. The velocity is similar to some magneto-tactic bacteria strains. The maximum speed of the helical propeller in low Reynolds number flow is $96 \mu\text{m}/\text{s}$ from [Chen et al. \(2017b\)](#) [Ghosh et al. \(2009\)](#). The design of symmetrical double helix can be explored further and developed.

4.3.6 Analysis

Because of the difficulties with the prototype fabrication with current technologies for case 2, the analysis method is different from case 1 (cross-development). In this section, the force analysis of the robot is conducted based on human body vessel environment conditions.

Thrust force analysis

In the case of this study, the thrust force is generated by the rotation of the helix tails. The magnitude of the force is affected by several factors, such as the shape of tails, fluid properties and rotating speed. For the shape of tails, this case mainly focuses on the relationship between helix diameter and thrust force. The simulation results can be found in Fig. 4.32.

The average lumen diameter of human blood vessels listed below.

Elastic artery: 1.5 cm

muscle artery: about 6 mm

veins: 5 mm

small artery: about 37 microns

small veins: 20 microns

Capillary: About 9 microns

It can be seen that the smallest vessel is capillary which has about 9 microns diameter. Therefore, the ideal robot tails' diameter should much smaller than this to allow it to access most of the parts in the human body. So, the diameter range should be 0.1-3 microns. In this simulation 1.3 μm is chosen.

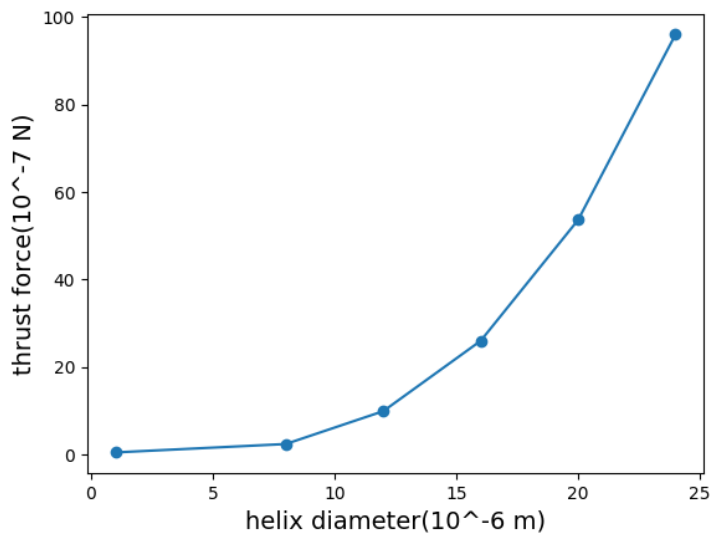


Fig. 4.32 thrust force vs. tails diameter

From Fig. 4.32 it can be found that the thrust force increasing when helix tails diameter becomes bigger. The relationship is not a direct ratio i.e. non-linear. So, in the limitation of volume, increasing the tails' diameter is a good way to achieve higher thrust force. The results compared with previous research [Demir and Yesilyurt \(2017\)](#) as shown in Fig. 4.33.

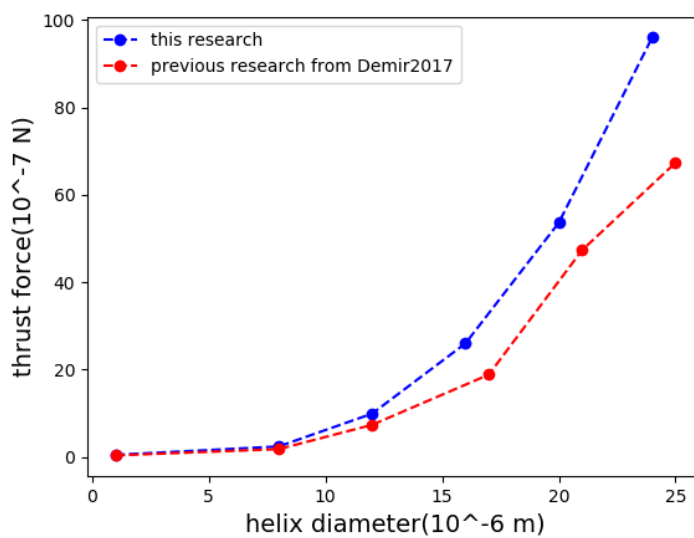


Fig. 4.33 thrust force vs. tails diameter Comparison

From Fig. 4.33, it can be seen that both cases have the same trend but the thrust force of this research is higher than previous research from Demir and Yesilyurt (2017). It illustrates that greater thrust force has been generated by the double helix flagella structure.

Resistance force analysis

The resistance forces of an object moving in the fluid can be divided into three categories: parasitic drag, pressure difference resistance and wave-making resistance.

In this case, the object is emerging in fluid, so wave-making resistance does have an important role. So, the components of resistance forces, in this case, includes parasitic drag and pressure difference resistance, where parasitic drag is the main part of the resistance force. The parasitic drag is mainly caused by wet surface area and dynamic viscosity.

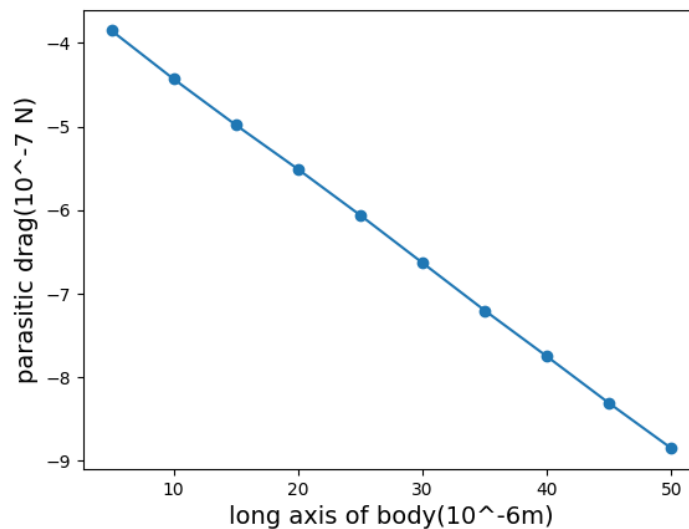


Fig. 4.34 relationship between parasitic drag and wet surface area

Fig. 4.34 shows the relationship between the resistance force and the length of the long axis of the body. The change of the short axis of the body creates more variables such as the Coanda Effect. So, only the longitude of the long axis of the body set as the independent variable. The change of the long axis of the body leads to wet surface area change which creates bigger parasitic drag. So, a decreased value of the longitude of the long axis of the body can significantly decrease the resistance force.

Another factor namely dynamic viscosity of fluid depends on the application environment. However, it is not discussed in this case.

The relation of this research to existing work on human blood-vessel robots are summarising in table 4.3.

Table 4.3 The relation of this research to existing work on human blood-vessel robots

Parameters	Zhang et al. (2009b)	Demir and Yesilyurt (2017)	Case 2 in this research
Tails geometry	helical ribbon	helical rod	helical filaments
Wavelength, λ	7.89	1	9.6
Amplitude, R	1	0.1	1.3
Radius, a	-	0.04	0.1
Thrust force	3.0×10^{-12}	6.1×10^{-6}	8.8×10^{-6}

4.4 Summary

This chapter presents the process, settings and results of the simulation for this research. Two cases have been conducted i.e. pipe inspection robot and a human vessel robot. All the settings and parameters given in details and the results demonstrated too. The shape design, experiment and optimisation have been achieved with these simulation results. The following chapter presents experimentation and its results relevant to the simulations.

Chapter 5

Experiments and Analysis

5.1 Introduction

In the previous chapter, the method of numerical simulation is utilised to analyse the micro-swimming robot and to calculate the change of the swimmer's status and the surrounding flow field. To verify whether the numerical simulation method can be applied to the micro-robot, an appropriate experimental platform with similar numerical simulation conditions must be developed. For this reason, an experimental system has been designed to meet the simulation conditions. It is also necessary to verify if the double helix propeller can be applied to improve the performance in low Reynolds number fluid with experimental conditions. Because of the limitation of fabrication technology, the micro-scale robot cannot be developed at the current stage. So, only the pipe inspection robot is developed to verify the double helix propeller design. The experimental system consists of two parts: pipeline-inspection robot prototype and experimental device. The robot is the main focus of the experimental study. Its function is to carry out the swimming experiment according to the theoretical guidance to realise the motor function and various manoeuvring performances. The experimental device is an indispensable component for the experiment, mainly as a measurement and other physical quantity monitoring device. The functions of the experimental device are to collect the measurement data and monitor the working status of the micro-robot. Also, it is responsible for photographing the movements of micro-swimming robots and for performing trajectory analysis. The main purpose of this experiment is to study the relationships between the velocity and the related factors.

5.2 Prototype design and fabrication

5.2.1 Prototype Design

Experimental pipeline detection robot is mainly composed of three parts: a DC micro-motor, energy supply i.e. battery and tail thruster as shown in Fig.5.1. Micromotors and battery are installed in the housing of the robot body. The double helix propeller forms the tail of the robot. The head material of the robot is plastic. The tail is made by rapid prototyping, the material is photosensitive resin, which is connected to the main body and provides propulsion. Since the external power supply will affect the robot trajectory and force, this design uses a built-in battery. There is a wireless control chip also contained in the body.

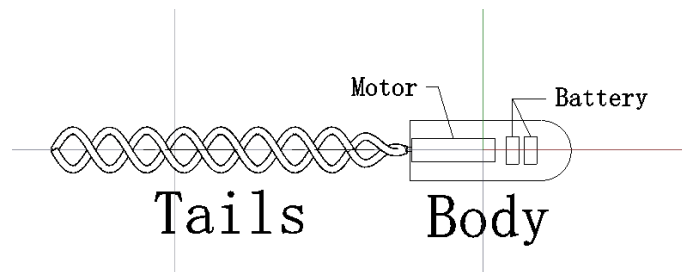


Fig. 5.1 Prototype structure

After optimisation based on the simulation results, the proposed optimised structure is shown in Fig. 5.2.

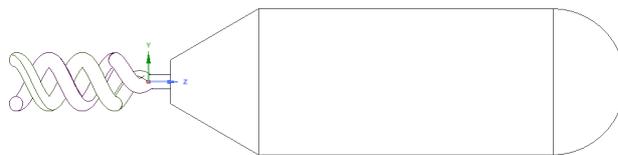


Fig. 5.2 The Optimised structure

5.2.2 Prototype fabrication

Based on the prototype design, the next step is to realise or implement the design. The prototype fabrication is an extremely challenging task for this research. The process includes components selection matching, assembling, and testing.

The components include the motor, battery and wireless controller. Firstly, the motor type needs to be decided. There are several choices such as DC motor, servo motor, step motor etc. To achieve the simplest structure and reduce the weight of the robot, a core-less DC motor is selected. Other types need more control chip, driven chip etc, and will increase the size and complexity of robot. The motor length and diameter are shown in Fig. 5.3 and Fig. 5.4, respectively. The Key features of the motor are shown in table 5.1. To match the size of the robot, a cell battery model GPA76 is selected. A miniature wireless controller is selected for the un-tethered control.

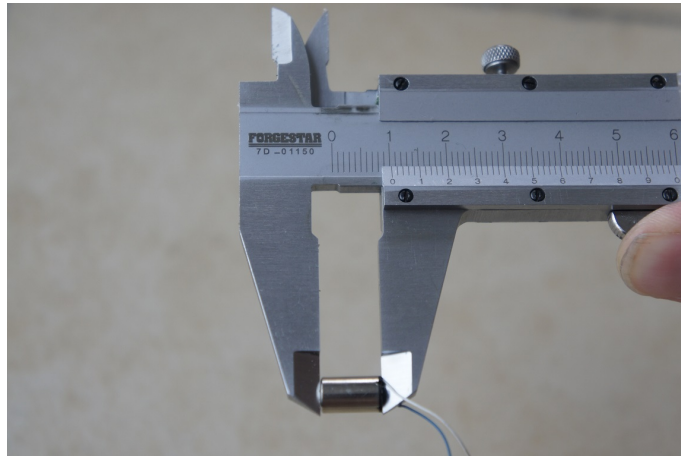


Fig. 5.3 The length of the DC Motor

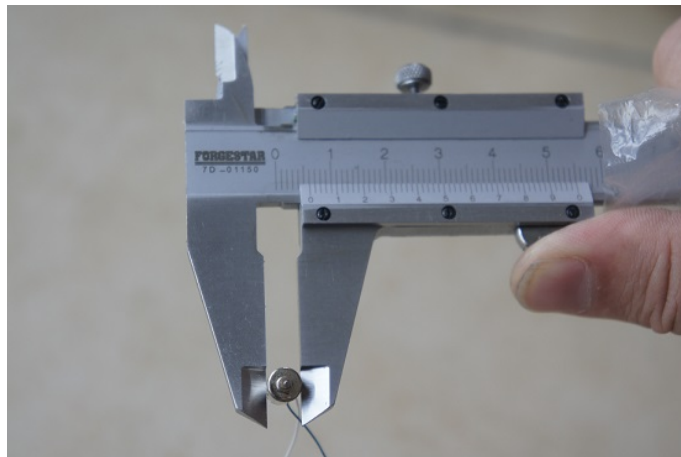


Fig. 5.4 The Diameter of the DC Motor

The Key features of the motor show in table 5.1.

Fig. 5.5 shows the wireless control chip and compares it with a one-pound coin.

Table 5.1 Key features of the chosen motor

Name	Value
Body Diameter:	6 mm
Body Length:	10.1 mm
Typical N/L Current:	32 mA
Typical Power Consumption:	145 mW
Rated Voltage:	3 V
Rated Torque:	0.01 mNm
Min. Rated Speed:	2,200 rpm
Lead Length:	45 mm
Lead Wire Gauge:	32 AWG



Fig. 5.5 Wireless control chip compare to coin

The tails are produced by 3-Dimensional(3D) printing technology. 3D printing is a rapid prototyping technology which is based on the digital model. It uses powdery metal or plastic and other adhesive materials and builds objects layer by layer. In general, getting an item through 3D printing requires four major phases of modelling, layering, printing, and post-processing. In the course of this research, three sets of spiral tails based on digital models are generated by Auto-CAD three-dimensional modelling software. The models are cut into layers by the professional software provided by the 3D printer. The thickness of each slice is determined by the sprayed material attributes and printer specifications, and then the 3D printer prints layer by layer into the three-dimensional space to build the

structure of the spiral tail entity. After the completion of the print process on a physical surface, some of the rough parts are treated e.g. curing, peeling, dressing, colouring etc. to complete the production of the spiral tail. The tails length and diameter are shown in Fig. 5.6 and Fig. 5.7, respectively. The dimensions of tails shown in table 5.2

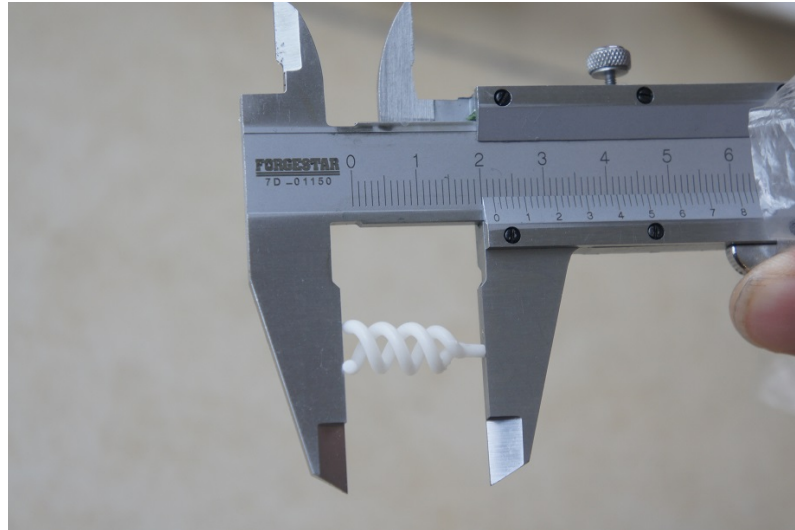


Fig. 5.6 The length of the original tails

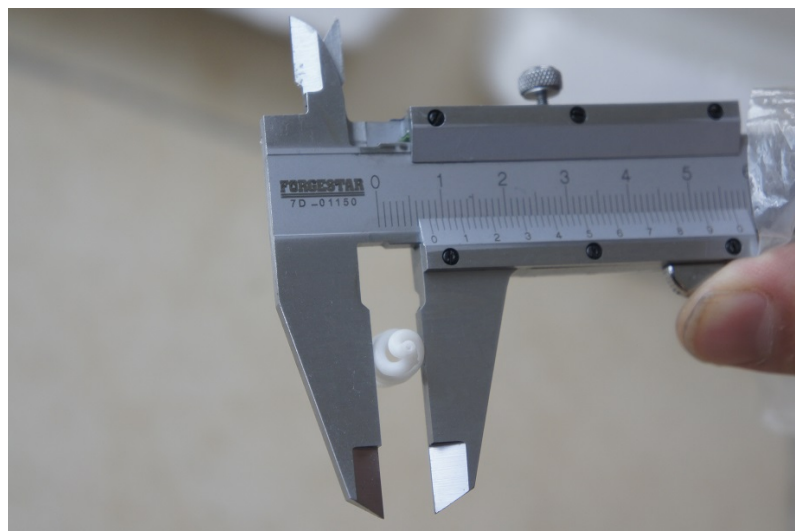


Fig. 5.7 The diameter of the original tails

Table 5.2 Tails Dimensions

Dimensions	Value
Amplitude(2R)	6 mm
Length	20 mm
Helix pitch	8 mm
Filament radius	2 mm

5.3 Experiment Facilities

5.3.1 Experiment Platform

The experimental device consists of an experimental bench, oil tank (shown in Fig. 5.8), velocity measurement system, camera and a computer. The experimental tank is a 170mm high, 220mm long, 130mm wide with glass slot providing a liquid environment for the entire experiment. The camera and computer together form the experimental video capture and data acquisition system for further detailed study and experimental rules to provide a feasibility analysis. The velocity measurement device is a key component of this experiment which is explained in the following section.



Fig. 5.8 The oil tank for the experiment

To reduce wall affections from front and back of the robot, as well as to increase wall affections from sides, a PMMA pipe is prepared and fulfilled with silicon oil. Fig. 5.9

shows the PMMA pipe. It provides a realistic environment and enough moving space for the robot.



Fig. 5.9 The PMMA pipe

5.3.2 Measuring Device

The current measurement methods for the experiment can be divided into two types: direct and indirect measurement methods. Besides, according to the structure of the velocity measurement, there are also two types: contact and non-contact.

As the contact measurement of the micro-robot movement has some certain impacts, and the measurement accuracy is not ideal, it cannot be applied to the robot's velocity measurement. Therefore, non-contact measurement has become the preferred measurement structure. The direct measurement method is executed through a measurement principle to obtain the amount of velocity, such as Doppler tachometer, space filter speed etc. directly. The biggest advantage of this method is the fast response as it can measure the instantaneous velocity. However, it has some drawback e.g. the measurement accuracy is not ideal, the measurement range is limited, and the measurement environment has certain requirements.

Indirect measurement method measures the moving distance and time of the target, through the calculation of the amount of velocity, such as photoelectric velocity, raster velocity, magnetic velocity and image velocity measurement. The biggest advantage of this method is simple and flexible and other benefits include high measurement accuracy, it can measure the average velocity etc. However, it has some problems e.g. the measurement range is quite different, the measurement environment has different requirements, it cannot measure the instantaneous velocity of the object etc. Recently, due to the development of

target recognition and target tracking technologies, image velocity has been widely used. The target recognition technique is a feature pattern recognition of the image. Its basic principle is to describe and model the target characteristics to be identified in detail.

In this experiment, the indirect measurement method has been used to measure the velocity of the microrobot. The average velocity of the robot's advancement during a period is obtained by measuring the time taken by the micro-swimming robot to travel a certain distance. The distance travelled by the robot has been measured in accordance with the design to meet the accuracy of the data, the time using infrared photoelectric system measurement as shown in Fig. 5.10. The practise has proved that this method produces a small error, high reliability. The velocity measuring device is composed of a swimming guide channel and an electronic time system circuit as shown in Fig. 5.11. The principle is to measure the travel time to move a certain distance for the microrobot and then solving the unit time or average velocity. So, the device setup can only measure the average velocity, and cannot measure the instantaneous velocity.



Fig. 5.10 Infrared radiation device

The measuring circuit is composed of an infrared light-emitting circuit, an infrared ray receiving circuit, a time-measuring device and a swimming channel as shown in Fig. 5.11. $A - A_0, B - B_0$ are two groups of two infrared photoelectric pairs of tubes. A, B are the infrared emission devices, A_0, B_0 are the infrared receivers, and normally open infrared photoelectric on the tube and become open when infrared light is received. When there is no obstruction between the launch tube and the receiving tube, the infrared-sensitive diode is closed due to infrared radiation, and the output level is high. When there is an obstruction between the launch tube and the receiving tube, the infrared sensor is turned on and the output level is low. The use of its level of output can be very easy to determine

whether there is an obstacle between the infrared tubes. Infrared receiver tubes A_0 and B_0 are connected in parallel and are then connected to the timer to form a timer circuit. When the object moves through to trigger the infrared photoelectric tube once, the timer will record this time.

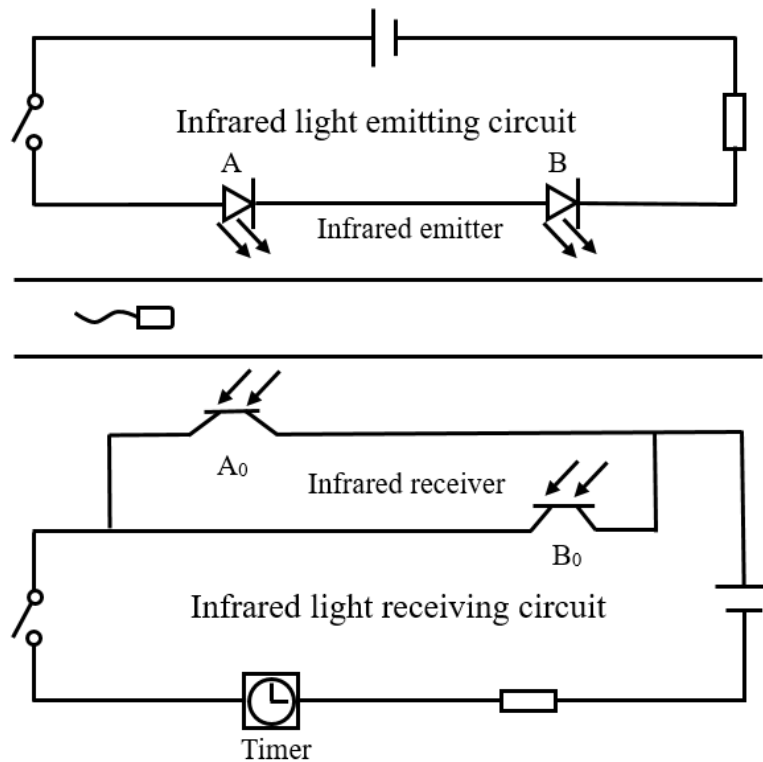


Fig. 5.11 Measurement device structure

Initially, the receiving channel A_0 and B_0 are open. These become closed when the infrared rays emitted from the infrared emitting tubes A and B are received and the circuit is open, and the timer is zero. When the micro-robot travels to position A, the infrared light from the infrared emission tube is blocked, A_0 cannot receive infrared light and so, it is turned on and the circuit is closed. The timer circuit is turned on and it is triggered to start timing. When the microrobot reaches position B, the infrared light emitted from the infrared emission tube B is blocked, and the receiver B_0 does not receive the infrared light. So, the timing circuit is triggered again, and the timer stops counting. At this point, the timer records the time taken for the microrobot to travel from A to B.

5.4 Experiment scheme, results and analysis

5.4.1 Experiment scheme

Due to the time limitation and the experimental conditions, this experiment mainly studies the advancing velocity of the micro-swimming robot, and analyses the related factors e.g. average velocity. The velocity is the distance travelled per unit time and can also be expressed as the time it takes for the moving unit distance. In this experiment, it is a given distance to measure the time spent by the micro-swimming robot, to get the average velocity of the robot. The effects of different tail structures on the propulsion velocity of the robot are studied for the same liquid.

One structure is traditional single helix tail robot and other two use double helix tails which be named as double tails original robot and double tails optimised robot in this study. The experiments for these two types of structures are conducted with the same conditions. The prototype of a single tail robot is depicted in Fig. 5.12. The prototype of double tails original, double tails optimised is shown in Fig. 5.6 and Fig. 5.13, respectively.

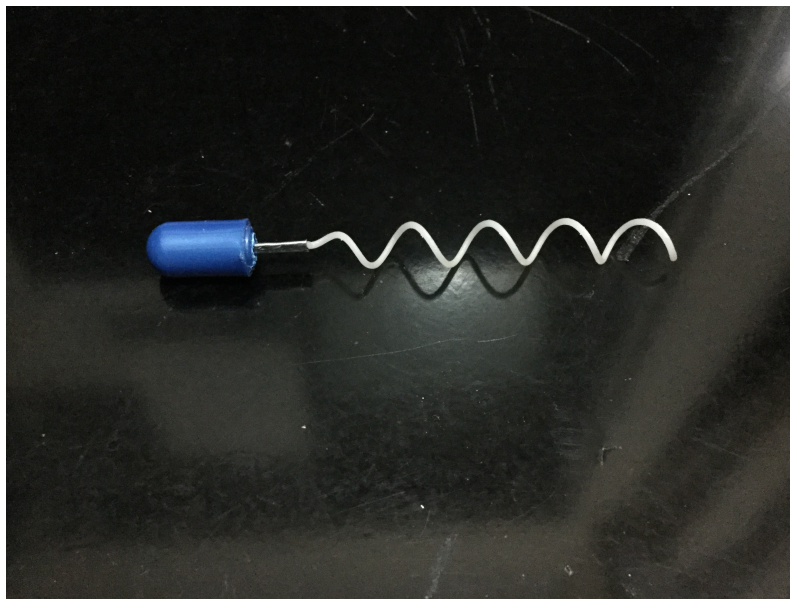


Fig. 5.12 The single tail robot

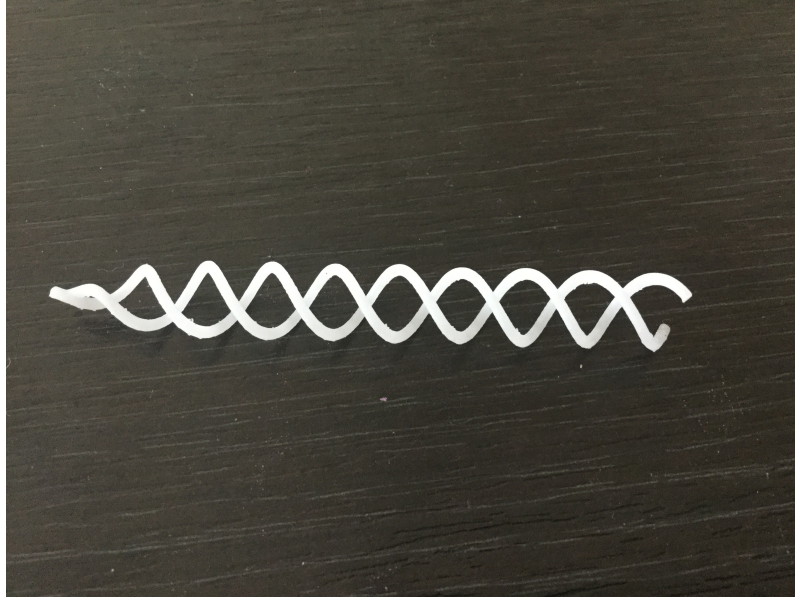


Fig. 5.13 The structure of double tails optimised

This experiment schemes into two parts:

The first part is to determine the effect of different tails structures on robot moving performance. As shown in Fig. 5.12, 5.13 and Fig. 5.6, this experiment uses 3D printing technology to process the spiral tails for three different sets of structures. These sets of the structure are separately tested in the experiment and compared to each other.

The second part is to identify the effects of different helical tail rotative velocity on the straight velocity of the optimised double tails robot.

The experimental set-up is shown in Fig. 5.14.



Fig. 5.14 The experimental set-up

5.4.2 Experiment results

The experiment results for the single helix robot focus on the propulsion velocity. For the limitation of the velocity measurement device, average velocity and maximum velocity is recorded. The maximum velocity of a single tail robot and double tail optimised robot is 44mm/s and 82mm/s, respectively as shown in Fig. 5.15.

In the first part of the experiment, three sets of tails with 2200r/min rotative velocity-driven swimming robot moving straightly. The robot movement times are recorded and Fig. 5.15 shows a set of v-t curve. The graphs correspond to three scheme respectively. The final steady-state velocity of each curve is taken as the straight-line velocity of the robot and the difference is calculated. For each robot 5 readings have been taken and the experimental results are given in Table 5.3.

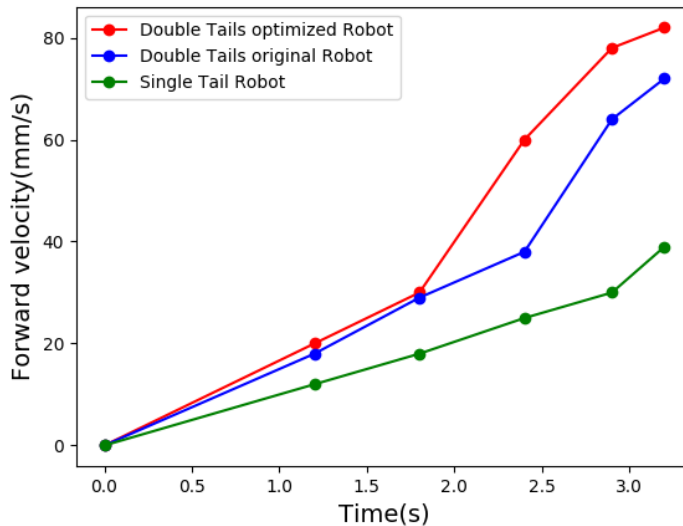


Fig. 5.15 v-t curve of double tails original, optimised and single tail robot

According to the data given in Table 5.3, a maximum velocity of 82 mm/s is achieved by the swimming robot.

The results have proven that the double tails design can achieve much higher velocity in the same conditions. The design is valuable for further development.

Through the use of different batteries, the motor rotative velocity is changed. Based on the different rotative velocity of the tail, the different moving velocity is obtained. Fig. 5.16 shows the experimental results. It can be seen from the figure that with the increase of the helical tail rotative velocity, the straight velocity of all three swimming robots increases gradually followed by a rapidly decreasing trend. This phenomenon is explained in section 5.4.3.

Table 5.3 Experiment results of different tail design

No.	a/mm	λ /mm	h/mm	Maximum Velocity(mm/s)
1	2.16	2.64	1.31	82
2	3	2.64	1.51	72
3	2.16	2.64	1.31	42

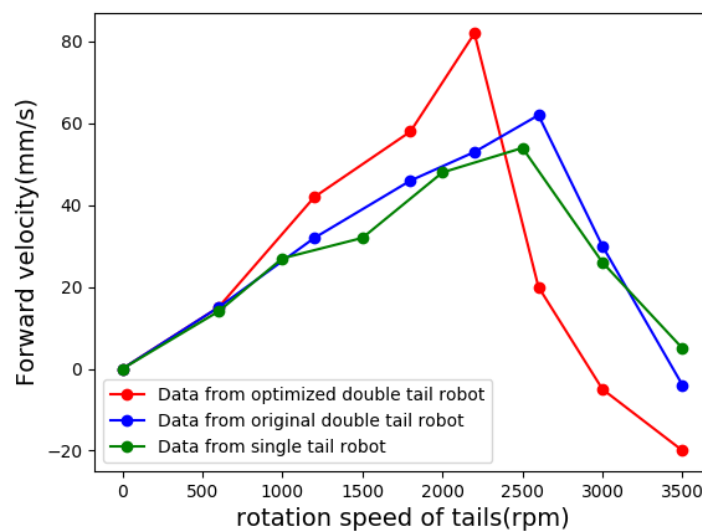


Fig. 5.16 The robot velocity change with tail rotative velocity

From Fig. 5.16, it is also clear that even the rotative velocity increases, the straight velocity of the single tail robot only can achieve a maximum of around 50mm/s. On the other hand, the velocities of double tail and optimised double tail robots achieve maximum values of a 60mm/s and beyond 80mm/s, respectively. The advantage of the double tail structure i.e. double tail and optimised double tail is observed clearly.

5.4.3 Experiment results comparison with numerical simulation

The experiment results are largely consistent with the numerical simulation results obtained in chapter 4 and the comparison can be found in Fig. 5.17. However, some conspicuous differences between experiment and numerical simulation are noted. The difference may be caused by a set of factors as explained in the following sentence. In addition to the above-mentioned structural dimensions and swimming parameters, the other major factors include the micro-robot itself, the liquid density and the viscosity, and factors that affect

the velocity and propulsion of the micro-swimming robot e.g. near-wall effect and so on. These factors in some cases will have a certain impact on the movement of the robot.

The resonance is a factor which affects the motion of the robot. When the resonance phenomenon occurs, the robot's tail swing or micro-motor rotation frequency gets close to the robot's natural frequency and the robot's swimming velocity slows down. Although the tail still does rotary motion, the robot's head does the vibration movement that offsets a part of the tail of the propulsion, so the velocity declines.

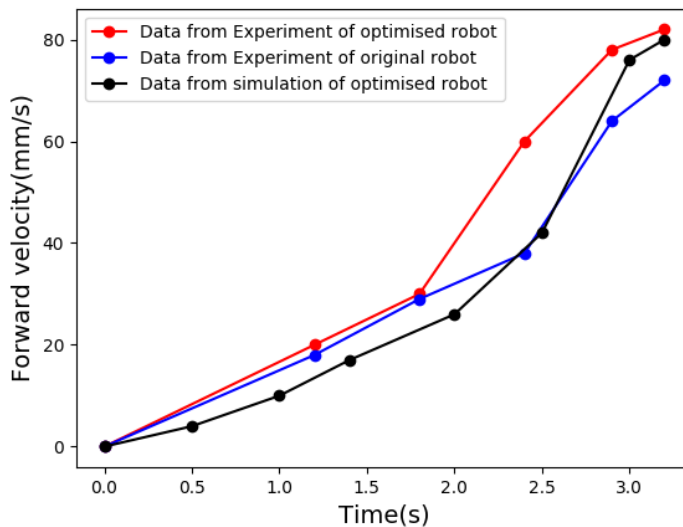


Fig. 5.17 V-t curve comparison between simulation and experiment for the double tail optimised robot

Comparing the above experimental data with the simulation results in section 4.2.6, it is found that the measured direct velocity of the swimming robot is generally larger than the simulated value. This is because the robot is not completely in the liquid when it is moving in the experiments. This means that the robot experiences a decrease in viscous resistance and so, the straight velocity becomes larger. Besides, due to the human error in the experiment and the accuracy of the grids, the results between the two methods have some differences. However, for the relationship between the parameters of the helical tail on the robot's straight velocity, the conclusion of the two methods is the same.

Comparison between experiment and simulation about relationship of velocity and rotative velocity

The relationship between velocity and rotative velocity are compared for experiment results and simulation of the optimised robot are shown in Fig. 5.18.

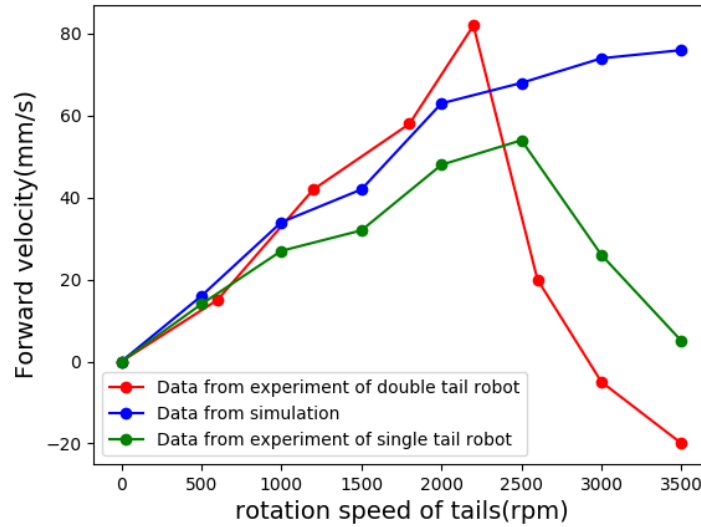


Fig. 5.18 Velocity to rotative velocity comparison between simulation and experiment

It can be found that where the value of ω is small e.g. 0-2000 rpm, the experimental result of velocity change is similar to the numerical calculation shown in Fig. ???. However, when ω value continues to increase; the experimental data and simulation results appear different and the robot straight velocity reaches a certain fixed value followed by a significantly drop.

This may due to the high-velocity movement of the spiral tails which causes the liquid flow state change from the laminar into a turbulent flow. This makes the pressure from the robot body side much higher than pressure from the tail side until the propulsion force generated by spiral tails can be ignored. On the other hand, for the case of simulation, the calculation model is set to a fixed model i.e. it does not present the flow state change. So, the simulation does not show the same phenomenon.

When a spiral tail of robot rotates at high velocity in a liquid-filled pipeline, the pressure and velocity of the liquid change with time and the pulsation is stronger that leads vorticity to increase. The flow around the tail changes to turbulent flow. It can be presented by the eddy-viscosity model using the Reynolds averaging method as given below.

$$-\rho \overline{V_i' V_j'} = \mu_t \left(\frac{\partial V_i}{\partial x_j} + \frac{\partial V_j}{\partial x_i} \right) - \frac{2}{3} (\rho \kappa + \mu_t \frac{\partial V_i}{\partial x_i}) \delta_{ij} \quad (5.1)$$

where the $\delta_{ij} = \begin{cases} 1 & i=j \\ 0 & i \neq j \end{cases}$, κ is the turbulent kinetic energy.

Another explanation is the cavity flow theory. A cavity occurs based on continuous destruction of the liquid medium and is the result of reduced pressure. When the pressure

in a liquid drops below a certain critical value, the liquid vaporises. A radial direction, it is known from the energy conservation theory that the energy to expand the cavitation is equal to the initial kinetic energy of the water flow. The momentum relation is given below.

$$E_k = \frac{1}{4}\pi\mu\rho U_\infty^2 \left(\frac{dr^2}{dx}\right)^2|_{x=0} = \frac{D}{k} \quad (5.2)$$

where $D = \frac{1}{2}C_J\rho\pi R^2U_\infty^2$ is cavitation resistance; ρ is the density of fluid; C_J is the cavitation resistance when there is no cavity; coefficient $k = 0.96 \sim 1$; $\mu = \ln\frac{\lambda}{\sqrt{e}}$.

The near-wall affection is another important factor which affects the performance of robot mobility. The so-called near-wall effect happens when the swimming object is close to the wall and the wall has an impact on its swimming state. When the robot is away from the wall, the swimming state is significantly different. The influence of the near-wall effect on the swimming stage of the micro-robot is mainly reflected in its influence on the velocity of the swimming and the smoothness of the swimming propulsion. When the micro-robot is in the vicinity of the wall forward swimming, the swimming velocity will be reduced due to the impact of the near-wall effect. When a micro swimming robot operates far away from the walls, its swimming stability is significantly improved.

5.5 Summary

This chapter conducts experiments to verify the design of double helix and its simulation results. The experiment works are divided into three parts: prototype, experiment facilities and experiment conduction. The experiment results present a similar performance when compared to simulation results. However, some differences have been noticed which are discussed.

Chapter 6

Conclusion and Future Work

6.1 Main work of this thesis

The movement of micro-swimming beings in the low Reynolds number liquid environment is the inspiration for the development of the micro-swimming robot. The researches relevant to the forms and mechanisms of single-celled organisms such as flagellates and the bionic designs have become hot topics in recent years. In this study, a new type of symmetric double helix propulsion structure has been proposed and the bionic mechanism and motion characteristics are studied utilising theoretical analysis, numerical simulation and experimental measurement. The main research results and works are as follows.

(1) Based on a brief introduction of micro-hydrodynamics, five most widely used theories and methods for flagella propulsion—slender body theory, resistance theory, immersion boundary theory, boundary element theory and method of regularised Stokes—have been discussed. It is found that the slender body theory is suitable for the calculation of the elongated flagellum propulsion, and the calculation accuracy is high, but the closed solution is very difficult to obtain, and the ability to calculate the fluid effect of the bacterial head is poor. The boundary element theory is suitable for any flagellum for bacteria, and the result is the most accurate. However, the disadvantage of BEM include difficult theoretical operation, complicated calculation, and the analytical solution of the flow field around the bacteria cannot be obtained. The calculation accuracy of the resistance theory depends on the choice of the pressure coefficient. In the case of normal precision requirements, for its calculation process is very simple and easy to operate, which is applied to most of the helix propulsion researches.

(2) To increase the movement performance of a swimming micro-robot, a novel double-helix design is proposed. The design is composed of a cone connection part and cylinder-shaped main tail part. In the same environment and robot condition, the double helix design has better stability and more than 20% higher velocity. This may have

benefited from the symmetrical structure which brings balance and generate higher thrust force for the whole robot.

(3) Based on the computational fluid dynamics, the direct motion of the spiral propulsion robot with the symmetrical double helix propulsion structure has been simulated by CFD analysis software Fluent. The numerical results show that the main factors affecting the straight speed of the swimming robot are the number of the whole wave of the spiral tail, followed by the section thickness and the pitch and the effect of the cross-section width is the smallest. Moreover, the faster the rotation of the helical tail is, the greater the speed at which the robot can reach. Besides, the straight speed of the robot increases linearly with the density of the liquid medium and decreases with the increase of the dynamic viscosity coefficient.

(4) A measurement system based on vision is established, and a kinematic parameter measurement method based on infrared detection switch is established for the swimming robot. Based on the experimental platform and the measurement methods, the effects of the helical tail structure parameters, the liquid environmental parameters and the helical end kinematic parameters on the straight speed of the robot are studied experimentally. The experimental data show that the relationships between the above parameters and the straight speed of the robot are in good agreement with the simulation results. After more than a certain speed, the experimental results are different from the simulation results.

In this thesis, the non-destructive micro-swimming robot is studied and it is expected to be applied in the small pipeline of industrial environment and medical field. A new structure design scheme of the micro-swimming robot is proposed, and the dynamic equation of spiral robot in the liquid pipeline is established. And the operating parameters (liquid density, liquid viscosity, pipe diameter, eccentricity, bending pipe, shell speed, internal shaft speed, internal and external surface) of the spiral robot are obtained by using computational fluid dynamics method. The fluid flow field speed and the speed of the robot are also inspected on the robot performance issues (including the axial propulsion force, the maximum pressure of the pipe wall, and the liquid on the bearing capacity of the robot).

6.2 Future Works

In this study, the micro-swimming robot is studied only in terms of velocity, and only the experiment of the forward direction is carried out. In future experiments, the propulsion force, the resistance, the acceleration and the eddy current effect lifting, retreat and other functions can be studied.

In this study, only the shape of the tail side of the micro-swimming robot is discussed and experimented, and its thickness and cross-sectional shape are not discussed. This makes the efficiency of the robot relatively low; manoeuvrability is also relatively poor. These should be considered in future theoretical analysis and experimental researches.

The spiral robot proposed in this thesis is small in size, simple in structure and can realise the advance and retreat in the straight pipe. However, its direction change is a difficult problem. Adding a reasonable steering device will be an upgrade for the flexible operation of the robot. The simple structure decreases the difficulty of fabrication, which can promote the possibility of realising autonomous swimming patrol robot. The future works should include exploration in this field.

In the numerical calculation, some assumptions and simplifications are made in the thesis, and the material and volume of the robot affect the gravity and buoyancy of the robot. So, it will affect the numerical calculation. These factors need further consideration. The robot is not only straight tube, but more of the situation is also an elbow, the precise positioning of the robot and motion control can be the focuses of future researches.

References

- Abbott, J. J., Ergeneman, O. O. O., Kummer, M. P., Hirt, A. M., and Nelson, B. J. (2007). Modeling magnetic torque and force for controlled manipulation of soft-magnetic bodies. *IEEE Transactions on Robotics*, 23(6):1247–1252.
- Abbott, J. J., Peyer, K. E., Lagomarsino, M. C., Zhang, L., Dong, L., Kaliakatsos, I. K., and Nelson, B. J. (2009). How Should Microrobots Swim? *The International Journal of Robotics Research*, 28(11-12):1434–1447.
- Ahmed, D., Baasch, T., Blondel, N., Läubli, N., Dual, J., and Nelson, B. J. (2017). Neutrophil-inspired propulsion in a combined acoustic and magnetic field. *Nature Communications*, 8(1):770.
- Ainley, J., Durkin, S., Embid, R., Boindala, P., and Cortez, R. (2008). The method of images for regularized Stokeslets. *Journal of Computational Physics*, 227(9):4600–4616.
- Ajdari, A., Golestanian, R., and Ajdari, A. (2008). Analytic results for the three-sphere swimmer at low Reynolds number. *Physical Review E - Statistical, Nonlinear, and Soft Matter Physics*, 77(3):7.
- Alexander, G. P., Pooley, C. M., and Yeomans, J. M. (2009). Hydrodynamics of linked sphere model swimmers. *Journal of physics. Condensed matter : an Institute of Physics journal*, 21(20):204108.
- Aranson, I. S., Sokolov, A., Kessler, J. O., and Goldstein, R. E. (2007). Model for dynamical coherence in thin films of self-propelled microorganisms. *Physical Review E - Statistical, Nonlinear, and Soft Matter Physics*, 75(4):040901.
- Avron, J. E., Gat, O., and Kenneth, O. (2004). Optimal swimming at low reynolds numbers. *Physical Review Letters*, 93(18).
- Baranes, A. and Oudeyer, P. Y. (2013). Active learning of inverse models with intrinsically motivated goal exploration in robots. *Robotics and Autonomous Systems*, 61(1):49–73.
- Baskaran, A. and Marchetti, M. C. (2009). Statistical mechanics and hydrodynamics of bacterial suspensions. *Proceedings of the National Academy of Sciences of the United States of America*, 106(37):15567–15572.
- Batchelor, G. K. (1970). Slender-body theory for particles of arbitrary cross-section in Stokes flow. *Journal of Fluid Mechanics*, 44(03):419.
- Baudry, J., Roper, M. L., Fermigier, M., Stone, H. A., Dreyfus, R., Baudry, J., Roper, M. L., Fermigier, M., Stone, H. A., and Bibette, J. (2005). Microscopic artificial swimmers. *Nature*, 437(7060):862–865.

- Becker, F., Minchenya, V., Zimmermann, K., and Zeidis, I. (2012). Single Piezo Actuator Driven Micro Robot for 2-Dimensional Locomotion. *Micromechanics and Microactuators*, pages 1–10.
- Becker, L. E., Koehler, S. a., and Stone, H. a. (2003). On self-propulsion of micro-machines at low Reynolds number: Purcells three-link swimmer. *Journal of Fluid Mechanics*, 490(1):15–35.
- Behkam, B. and Sitti, M. (2004). E. coli inspired propulsion for swimming microrobots. In *Proceedings of IMECE International Mechanical Engineering Conference*, pages 13–19.
- Behkam, B. and Sitti, M. (2005). Modeling and Testing of a Biomimetic Flagellar Propulsion Method for Microscale Biomedical Swimming Robots. In *Proceedings, 2005 IEEE/ASME International Conference on Advanced Intelligent Mechatronics.*, pages 37–42. IEEE.
- Behkam, B. and Sitti, M. (2006). Design Methodology for Biomimetic Propulsion of Miniature Swimming Robots. *Journal of Dynamic Systems, Measurement, and Control*, 128(1):36.
- Berg, H. C. (1974). Dynamic properties of bacterial flagellar motors. *Nature*, 249(5452):77–79.
- Berg, H. C. and Anderson, R. a. (1973). Bacteria swim by rotating their flagellar filaments. *Nature*, 245(5425):380–382.
- Berke, A. P., Turner, L., Berg, H. C., and Lauga, E. (2008). Hydrodynamic attraction of swimming microorganisms by surfaces. *Physical Review Letters*, 101(3):38102.
- Blake, J. (1971). Self propulsion due to oscillations on the surface of a cylinder at low Reynolds number. *Bulletin of the Australian Mathematical Society*, 5(02):255.
- Blake, J. (1972). A model for the micro-structure in ciliated organisms. *Journal of Fluid Mechanics*, 55(01):1.
- Block, S. M., Blair, D. F., and Berg, H. C. (1989). Compliance of bacterial flagella measured with optical tweezers. *Nature*, 338(6215):514–518.
- Blum, J. J. and Lubliner, J. (1973). Biophysics of flagellar motility. *Annual review of biophysics and bioengineering*, 2(02):181–219.
- Bouzarh, E. L., Layton, A. T., and Young, Y. N. (2011). Modeling a semi-flexible filament in cellular Stokes flow using regularized Stokeslets. *International Journal for Numerical Methods in Biomedical Engineering*, 27(12):2021–2034.
- Bouzarh, E. L. and Minion, M. L. (2010). A multirate time integrator for regularized Stokeslets. *Journal of Computational Physics*, 229(11):4208–4224.
- Brennen, C. and Winet, H. (1977). Fluid Mechanics of Propulsion by Cilia and Flagella. *Annual Review of Fluid Mechanics*, 9(1):339–398.
- Broersma, S. (1960). Viscous Force Constant for a Closed Cylinder. *The Journal of Chemical Physics*, 32(6):1632.

- Brokaw, B. Y. C. J. and Brokaw, C. J. (1965). Non-sinusoidal bending waves of sperm flagella. *The Journal of experimental biology*, 43(1):155–169.
- Brokaw, C. J. (1974). Movement of the flagellum of some marine invertebrate spermatozoa. In *Cilia and Flagella*. Academic Press.
- Brokaw, C. J. (1979). Calcium-induced asymmetrical beating of triton-demembrated sea urchin sperm flagella. *Journal of Cell Biology*, 82(2):401–411.
- Burri, J. T., Vogler, H., Munglani, G., Laubli, N. F., Grossniklaus, U., and Nelson, B. J. (2019). A Microrobotic System for Simultaneous Measurement of Turgor Pressure and Cell-Wall Elasticity of Individual Growing Plant Cells. *IEEE Robotics and Automation Letters*, 4(2):641–646.
- Byun, D., Choi, J., Cha, K., Park, J.-o. O., and Park, S. (2011). Swimming microrobot actuated by two pairs of Helmholtz coils system. *Mechatronics*, 21(1):357–364.
- Chen, B., Jiang, S., Liu, Y., Yang, P., and Chen, S. (2010). Research on the kinematic properties of a sperm-like swimming micro robot. *Journal of Bionic Engineering*, 7(SUPPL.):S123–S129.
- Chen, B., Liu, Y.-d. D., Chen, S., Jiang, S.-r. R., and Wu, H.-t. T. (2008). A Biomimetic Spermatozoa Propulsion Method for Interventional Micro Robot. *Journal of Bionic Engineering*, 5(SUPPL.):106–112.
- Chen, X., Zeng, L., Wu, Y., Gao, Y., and Zhao, Y. (2017a). Swimming characteristics of gyrotactic microorganisms in low-Reynolds-number flow: *Chlamydomonas reinhardtii*. *Energy, Ecology and Environment*, 2(5):289–295.
- Chen, X.-Z., Hoop, M., Mushtaq, F., Siringil, E., Hu, C., Nelson, B. J., and Pané, S. (2017b). Recent developments in magnetically driven micro- and nanorobots. *Applied Materials Today*, 9:37–48.
- Clarke, R., Jensen, O. E., Billingham, J., Williams, P. M., Clarke, B. R. J., Jensen, O. E., Billingham, J., and Williams, P. M. (2006). Three-dimensional flow due to a microcantilever oscillating near a wall: an unsteady slender-body analysis. *Proceedings of the Royal Society A: Mathematical, Physical and Engineering Sciences*, 462(2067):913–933.
- Cohen, N. and Boyle, J. H. (2010). Swimming at low Reynolds number: a beginners guide to undulatory locomotion. *Contemporary Physics*, 51(2):103–123.
- Cortez, R. (2001). The Method of Regularized Stokeslets. *SIAM Journal on Scientific Computing*, 23(4):1204–1225.
- Cortez, R., Fauci, L., Medovikov, A., and Introduction, I. (2005). The method of regularized Stokeslets in three dimensions: Analysis, validation, and application to helical swimming. *Physics of Fluids*, 17(3):031504.
- Cosson, J., Huitorel, P., and Gagnon, C. (2003). How spermatozoa come to be confined to surfaces. *Cell Motility and the Cytoskeleton*, 54(1):56–63.
- Cox, R. G. (1971). The motion of long slender bodies in a viscous fluid. Part 2. Shear flow. *Journal of Fluid Mechanics*, 45(04):625.

- Crowdy, D., Lee, S., Samson, O., Lauga, E., and Hosoi, a. E. (2010). A two-dimensional model of low-Reynolds number swimming beneath a free surface. *Journal of Fluid Mechanics*, 681:24–47.
- Daneshmand, M., Bilici, O., Bolotnikova, A., and Anbarjafari, G. (2017). Medical robots with potential applications in participatory and opportunistic remote sensing: A review. *Robotics and Autonomous Systems*, 95:160–180.
- Davies, C. (1975). Low reynolds number hydrodynamics, with special applications to particulate media. *Journal of Aerosol Science*, 6(3-4):273.
- Davis, A. M. J. and Lauga, E. (2009a). Geometric transition in friction for flow over a bubble mattress. *Physics of Fluids*, 21(1):011701.
- Davis, A. M. J. and Lauga, E. (2009b). The friction of a mesh-like super-hydrophobic surface. *Physics of Fluids*, 21(11):1–8.
- Davis, A. M. J. and Lauga, E. (2010). Hydrodynamic friction of fakir-like super-hydrophobic surfaces. *Journal of Fluid Mechanics*, 661:402–411.
- Davis, R. O. and Katz, D. F. (1989). Computer-aided sperm analysis (CASA): image digitization and processing. *Biomaterials, artificial cells, and artificial organs*, 17(1):93–116.
- Demir, E. and Yesilyurt, S. (2017). Low Reynolds number swimming of helical structures in circular channels. *Journal of Fluids and Structures*, 74:234–246.
- Desimone, F. A. A. and Zoppello, L. G. M. (2017). Purcell magneto-elastic swimmer controlled by an external magnetic field. *IFAC-PapersOnLine*, 50(1955):4120–4125.
- Dillon, R. H., Fauci, L. J., Illon, R. O. H. D., and Auci, L. I. S. A. J. F. (2000). An integrative model of internal axoneme mechanics and external fluid dynamics in ciliary beating. *Journal of theoretical biology*, 207(3):415–430.
- Dillon, R. H., Fauci, L. J., Omoto, C., and Yang, X. (2007). Fluid dynamic models of flagellar and ciliary beating. *Annals of the New York Academy of Sciences*, 1101:494–505.
- Dombrowski, C., Cisneros, L., Chatkaew, S., Goldstein, R. E., and Kessler, J. O. (2004). Self-concentration and large-scale coherence in bacterial dynamics. *Physical Review Letters*, 93(9):2–5.
- Dreyfus, R., Baudry, J., and Stone, H. a. (2005). Purcell's "rotator": Mechanical rotation at low Reynolds number. *European Physical Journal B*, 47(1):161–164.
- Eckl, R., Gumprecht, J. D. J., Strauss, G., Hofer, M., Dietz, a., and Lueth, T. C. (2010). Comparison of manual steering and steering via joystick of a flexible rhino endoscope. *2010 Annual International Conference of the IEEE Engineering in Medicine and Biology Society, EMBC'10*, 2010:1234–1237.
- Edelmann, J., Petruska, A. J., and Nelson, B. J. (2018). Estimation-Based Control of a Magnetic Endoscope without Device Localization. *Journal of Medical Robotics Research*, 03(01):1850002.
- Elfring, G. J. and Lauga, E. (2009). Hydrodynamic phase locking of swimming microorganisms. *Physical Review Letters*, 103(8):1–4.

- Elfring, G. J. and Lauga, E. (2011). Passive hydrodynamic synchronization of two-dimensional swimming cells. *Physics of Fluids*, 23(1):011902.
- ELFRING, G. J. and LAUGA, E. (2011). Synchronization of flexible sheets. *Journal of Fluid Mechanics*, 674:163–173.
- Elfring, G. J., Pak, O. S., and Lauga, E. (2009). Two-dimensional flagellar synchronization in viscoelastic fluids. *Journal of Fluid Mechanics*, 646:505.
- Evans, A. a. and Lauga, E. (2010). Propulsion by passive filaments and active flagella near boundaries. *Physical Review E - Statistical, Nonlinear, and Soft Matter Physics*, 82(4):1–12.
- Fauci, L. J. and McDonald, a. (1995). Sperm motility in the presence of boundaries. *Bulletin of mathematical biology*, 57(5):679–699.
- Felderhof, B. U. (2006). The swimming of animalcules. *Physics of Fluids*, 18(6):063101.
- Flores, H., Lobaton, E., Méndez-Diez, S., Tlupova, S., and Cortez, R. (2005). A study of bacterial flagellar bundling. *Bulletin of Mathematical Biology*, 67(1):137–168.
- For, A., Gonzalez, O., Graf, a. B. a., and Maddocks, J. H. (2004). Dynamics of a rigid body in a Stokes fluid. *Journal of Fluid Mechanics*, 519:133–160.
- Foster, K. W. (2009). Analysis of the ciliary/flagellar beating of *Chlamydomonas*. *Methods in cell biology*, 91:173–239.
- Fujita, T. and Kawai, T. (2001). Optimum Shape of a Flagellated Microorganism. *Transactions of the Japan Society of Mechanical Engineers Series B*, 67(655):753–758.
- Fukuda, T., Kawamoto, a., Arai, F., and Matsuura, H. (1994). Mechanism and swimming experiment of micro mobile robot in water. *Proceedings IEEE Micro Electro Mechanical Systems An Investigation of Micro Structures, Sensors, Actuators, Machines and Robotic Systems*, pages 273–278.
- Fusco, S., Huang, H.-W., Peyer, K. E., Peters, C., Häberli, M., Ulbers, A., Spyrogianni, A., Pellicer, E., Sort, J., Pratsinis, S. E., Nelson, B. J., Sakar, M. S., and Pané, S. (2015). Shape-Switching Microrobots for Medical Applications: The Influence of Shape in Drug Delivery and Locomotion. *ACS Applied Materials & Interfaces*, page 150318150452001.
- Garner, L. J., Wilson, L. N., Lagoudas, D. C., and Rediniotis, O. K. (2000). Development of a shape memory alloy actuated biomimetic vehicle. *Smart Materials and Structures*, 9(5):673–683.
- Gauger, E. and Stark, H. (2006). Numerical study of a microscopic artificial swimmer. *Physical Review E - Statistical, Nonlinear, and Soft Matter Physics*, 74(2):21907.
- Ghanbari, A. and Bahrami, M. (2011). A novel swimming microrobot based on artificial cilia for biomedical applications. *Journal of Intelligent and Robotic Systems: Theory and Applications*, 63(3-4):399–416.
- Ghosh, A., Fischer, P., Ghost, A., and Fischer, P. (2009). Controlled propulsion of artificial magnetic nanostructured propellers. *Nano Letters*, 9(6):2243–2245.

- Gilbert, A. D., Ogrin, F. Y., Petrov, P. G., and Winlove, C. P. (2011). Theory of Ferromagnetic Microswimmers. *The Quarterly Journal of Mechanics and Applied Mathematics*, 64(3):239–263.
- Gillies, E., Cannon, R., Green, R., and a.a. Pacey (2009). Hydrodynamic propulsion of human sperm. *Journal of Fluid Mechanics*, 625(April):445.
- Golestanian, R. (2008). Three-sphere low-Reynolds-number swimmer with a cargo container. *European Physical Journal E*, 25(1):1–4.
- Golestanian, R., Liverpool, T. B., and Ajdari, a. (2007). Designing phoretic micro- and nano-swimmers. *New Journal of Physics*, 9(5):126–126.
- Gonzalez-Rodriguez, D. and Lauga, E. (2009). Reciprocal locomotion of dense swimmers in Stokes flow. *Journal of physics. Condensed matter : an Institute of Physics journal*, 21(20):204103.
- Gorini, S., Quirini, M., Mencias, a., Pernorio, G., Stefanini, C., Dario, P., Superiore, S., and Anna, S. (2006). A novel SMA-based actuator for a legged endoscopic capsule. In *Proceedings of the First IEEE/RAS-EMBS International Conference on Biomedical Robotics and Biomechanics, 2006, BioRob 2006*, volume 2006, pages 443–449. IEEE.
- Goto, T., Matsuda, S., Terada, K., and Takano, Y. (2001). Comparison between Observation and Boundary Element Analysis for Bacterium Swimming Motion. *Transactions of the Japan Society of Mechanical Engineers Series B*, 67(654):330–335.
- Gray, J., Hancock, G. J., Gray, B. Y. J., and Hancock, G. J. (1955). The Propulsion of Sea-Urchin Spermatozoa. *Journal of Experimental Biology*, 32(4):802–814.
- Gueron, S. and Levit-Gurevich, K. (1998). Computation of the internal forces in cilia: application to ciliary motion, the effects of viscosity, and cilia interactions. *Biophysical journal*, 74(4):1658–1676.
- Gueron, S., Levit-Gurevich, K., Liron, N., Blum, J. J., Ueron, S. H. A. Y. G., Urevich, K. O. L. E., Iron, N. A. L., and Lum, J. A. J. B. (1997). Cilia internal mechanism and metachronal coordination as the result of hydrodynamical coupling. *Proceedings of the National Academy of Sciences of the United States of America*, 94(12):6001–6006.
- Guo, S., Fukuda, T., and Asaka, K. (2003). A new type of fish-like underwater microrobot. *IEEE/ASME Transactions on Mechatronics*, 8(1):136–141.
- Guo, S., Ge, Y., Li, L., and Liu, S. (2006). Underwater swimming micro robot using IPMC actuator. In *2006 IEEE International Conference on Mechatronics and Automation, ICMA 2006*, volume 2006, pages 249–254. IEEE.
- Guo, S., Shi, L., Xiao, N., and Asaka, K. (2012). A biomimetic underwater microrobot with multifunctional locomotion. *Robotics and Autonomous Systems*, 60(12):1472–1483.
- Hancock, G. J. (1953). The Self-Propulsion of Microscopic Organisms through Liquids. *Proceedings of the Royal Society A: Mathematical, Physical and Engineering Sciences*, 217(1128):96–121.
- Hassanzadeh, P., Atyabi, F., and Dinarvand, R. (2019). The significance of artificial intelligence in drug delivery system design. *Advanced Drug Delivery Reviews*.

- Hata, N., Neubach, Z., Shoham, M., Kósa, G., Jakab, P., Hata, N., Jólesz, F., Neubach, Z., Shoham, M., Zaaroor, M., and Székely, G. (2008). Flagellar swimming for medical micro robots: Theory, experiments and application. In *Proceedings of the 2nd Biennial IEEE/RAS-EMBS International Conference on Biomedical Robotics and Biomechatronics, BioRob 2008*, pages 258–263. IEEE.
- Higdon, B. J. J. L. and Higdon, J. J. L. (1979). A hydrodynamic analysis of flagellar propulsion. *Journal of Fluid Mechanics*, 90(04):685.
- Higdon, J. J. L., Mathematics, A., and Physics, T. (1979). The hydrodynamics of flagellar propulsion: helical waves. *Journal of Fluid Mechanics*, 94(02):331.
- Holwill, M. E. J. and Holwill, M. E. J. (1966). Physical Aspects of Flagellar Movement. *Physiological Reviews*, 46(4):698–785.
- Honda, T., Arai, K., and Ishiyama, K. (1996). Micro swimming mechanisms propelled by external magnetic fields. *IEEE Transactions on Magnetics*, 32(5):5085–5087.
- Hsu, C. Y. and Dillon, R. (2009). A 3D motile rod-shaped monotrichous bacterial model. *Bulletin of Mathematical Biology*, 71(5):1228–1263.
- Hu, B. and Tu, Y. (2013). Coordinated Switching of Bacterial Flagellar Motors in a Single *E. Coli*. *Bulletin of the American Physical Society*.
- Hyon, Y., Marcos, Powers, T. R., Stocker, R., and Fu, H. C. (2012). The wiggling trajectories of bacteria. *Journal of Fluid Mechanics*, 705(1977):58–76.
- Ishikawa, T., Giacche, D., Giacché, D., and Ishikawa, T. (2010). Hydrodynamic interaction of two unsteady model microorganisms. *Journal of Theoretical Biology*, 267(2):252–263.
- Ishikawa, T., Sekiya, G., Imai, Y., and Yamaguchi, T. (2007). Hydrodynamic interactions between two swimming bacteria. *Biophysical journal*, 93(6):2217–2225.
- Ishiyama, K., Sendoh, M., and Arai, K. I. (2002). Magnetic micromachines for medical applications. *Journal of Magnetism and Magnetic Materials*, 242-245(PART I):41–46.
- Ishiyama, K., Sendoh, M., Yamazaki, a., and Arai, K. I. (2001a). Swimming micro-machine driven by magnetic torque. *Sensors and Actuators, A: Physical*, 91(1-2):141–144.
- Ishiyama, K., Sendoh, M., Yamazaki, A., Inoue, M., and Arai, K. (2001b). Swimming of magnetic micro-machines under a very wide-range of Reynolds number conditions. *IEEE Transactions on Magnetics*, 37(4):2868–2870.
- Itoh, A. (2000). Motion control of protozoa for bio MEMS. *IEEE/ASME Transactions on Mechatronics*, 5(2):181–188.
- Jager, E. W. H. (2000). Microrobots for Micrometer-Size Objects in Aqueous Media: Potential Tools for Single-Cell Manipulation. *Science*, 288(5475):2335–2338.
- Jahn, T. L. and Votta, J. J. (1972). Locomotion of Protozoa. *Annual Review of Fluid Mechanics*, 4(1):93–116.
- Johnson, R. E. and Brokaw, C. J. (1979). Flagellar hydrodynamics. A comparison between resistive-force theory and slender-body theory. *Biophysical Journal*, 25(1):113–27.

- Kamamichi, N., Yamakita, M., Asaka, K., and Zhi-Wei Luo (2006). A snake-like swimming robot using IPMC actuator/sensor. In *Proceedings 2006 IEEE International Conference on Robotics and Automation, 2006. ICRA 2006.*, number May, pages 1812–1817. IEEE.
- Kang, D., Martinez, R. V., Whitesides, G. M., and Tearney, G. J. (2013). Miniature grating for spectrally-encoded endoscopy. *Lab on a Chip*, 13(9):1810.
- Kantsler, V., Dunkel, J., Polin, M., and Goldstein, R. E. (2013). Ciliary contact interactions dominate surface scattering of swimming eukaryotes. *Proceedings of the National Academy of Sciences of the United States of America*, 110(4):1187–92.
- Katz, D. F., Blake, J. R., and Paveri-Fontana, S. L. (1975). On the movement of slender bodies near plane boundaries at low Reynolds number. *Journal of Fluid Mechanics*, 72(03):529.
- Keaveny, E. E. and Maxey, M. R. (2008). Interactions between comoving magnetic microswimmers. *Physical Review E - Statistical, Nonlinear, and Soft Matter Physics*, 77(4):041910.
- Khaderi, S. N., Baltussen, M. G. H. M., Anderson, P. D., Den Toonder, J. M. J., Onck, P. R., Toonder, J. M. J. D., and Onck, P. R. (2010). Breaking of symmetry in microfluidic propulsion driven by artificial cilia. *Physical Review E - Statistical, Nonlinear, and Soft Matter Physics*, 82(2):1–4.
- Khaderi, S. N., Craus, C. B., Hussong, J., Schorr, N., Belardi, J., Westerweel, J., Prucker, O., Rhe, J., den Toonder, J. M. J., and Onck, P. R. (2011). Magnetically-actuated artificial cilia for microfluidic propulsion. *Lab on a chip*, 11(12):2002–2010.
- Kim, B., Lee, M. G., Lee, Y. P., Kim, Y., and Lee, G. (2006). An earthworm-like micro robot using shape memory alloy actuator. *Sensors and Actuators A: Physical*, 125(2):429–437.
- Kim, M., Bird, J. C., Parys, A. J. V., Breuer, K. S., Powers, T. R., Van Parys, A. J., Breuer, K. S., and Powers, T. R. (2003). A macroscopic scale model of bacterial flagellar bundling. *Proceedings of the National Academy of Sciences of the United States of America*, 100(26):15481–15485.
- Kim, S. (1991). *Microhydrodynamics: Principles and Selected Applications*. Dover Publications.
- Kirkman-Brown, J. C. and Smith, D. J. (2011). Sperm motility: Is viscosity fundamental to progress? *Molecular Human Reproduction*, 17(8):539–544.
- Ko, Y., Na, S., Lee, Y., Cha, K., Ko, S. Y., Park, J., and Park, S. (2012). A jellyfish-like swimming mini-robot actuated by an electromagnetic actuation system. *Smart Materials and Structures*, 21(5):057001.
- Ksa, G., Shoham, M., and Zaaroor, M. (2005). Propulsion of a swimming micro medical robot. In *Proceedings - IEEE International Conference on Robotics and Automation*, volume 2005, pages 1327–1331. IEEE.
- Ksa, G., Shoham, M., and Zaaroor, M. (2006). Analysis of a swimming micro robot. *Proceedings of the First IEEE/RAS-EMBS International Conference on Biomedical Robotics and Biomechatronics, 2006, BioRob 2006*, 2006:130–134.

- Kósa, G., Shoham, M., Zaaroor, M., Member, A., and Zaaroor, M. (2007). Propulsion method for swimming microrobots. *IEEE Transactions on Robotics*, 23(1):137–150.
- Läubli, N. F., Shamsudhin, N., Vogler, H., Munglani, G., Grossniklaus, U., Ahmed, D., and Nelson, B. J. (2019). 3D Manipulation and Imaging of Plant Cells using Acoustically Activated Microbubbles. *Small Methods*, 3(3):1800527.
- Lauga, E. (2007a). Continuous breakdown of Purcell’s scallop theorem with inertia. *Physics of Fluids*, 19(6):061703.
- Lauga, E. (2007b). Floppy swimming: Viscous locomotion of actuated elastica. *Physical Review E - Statistical, Nonlinear, and Soft Matter Physics*, 75(4):23.
- Lauga, E. (2007c). Propulsion in a viscoelastic fluid. *Physics of Fluids*, 19(8):083104.
- Lauga, E. (2011). Enhanced diffusion by reciprocal swimming. *Physical Review Letters*, 106(17):1–4.
- Lauga, E. and Bartolo, D. (2008). No many-scallop theorem: Collective locomotion of reciprocal swimmers. *Physical Review E - Statistical, Nonlinear, and Soft Matter Physics*, 78(3):2–5.
- Lauga, E. and Davis, A. M. J. (2012). Viscous Marangoni propulsion. *Journal of Fluid Mechanics*, 705(Batchelor 1972):120–133.
- Lauga, E., DiLuzio, W. R., Whitesides, G. M., and Stone, H. A. (2006). Swimming in circles: motion of bacteria near solid boundaries. *Biophysical journal*, 90(2):400–412.
- Lauga, E. and Powers, T. R. (2008). The hydrodynamics of swimming microorganisms. *Reports on Progress in Physics*, 72(9):96601.
- Leal, L. (2007). *Advanced transport phenomena: fluid mechanics and convective transport processes*. Cambridge University Press, 1 edition.
- Lee, P. and Wolgemuth, C. W. (2012). An immersed boundary method for two-phase fluids and gels. *cims.nyu.edu*, pages 1–10.
- Lee, S., Kim, S., Kim, S., Kim, J.-Y., Moon, C., Nelson, B. J., and Choi, H. (2018). A Capsule-Type Microrobot with Pick-and-Drop Motion for Targeted Drug and Cell Delivery. *Advanced Healthcare Materials*, 7(9):1700985.
- Leshansky, a. M. (2009). Enhanced low-Reynolds-number propulsion in heterogeneous viscous environments. *Physical Review E - Statistical, Nonlinear, and Soft Matter Physics*, 80(5):51911.
- Lighthill, J. (1975). *Mathematical Biofluidynamics (Google eBook)*. Philadelphia:Society for Industrial and Applied Mathematics.
- Lighthill, J. (1976). Flagellar Hydrodynamics. *SIAM Review*, 18(2):161.
- Lim, S., Ferent, A., Wang, X. S., and Peskin, C. S. (2008). Dynamics of a Closed Rod with Twist and Bend in Fluid. *SIAM Journal on Scientific Computing*, 31(1):273–302.
- Lim, S. and Peskin, C. S. (2004). Simulations of the Whirling Instability by the Immersed Boundary Method. *SIAM Journal on Scientific Computing*, 25(6):2066–2083.

- Liu, B. (2012). Helical swimming in viscoelastic and porous media. *Bulletin of the American Physical Society*.
- Lo, C., Bhardwaj, K., and Marculescu, R. (2017). Towards cell-based therapeutics: A bio-inspired autonomous drug delivery system. *Nano Communication Networks*, 12:25–33.
- Lobatón, E. J. and Bayen, A. M. (2009). Modeling and optimization analysis of a single-flagellum micro-structure through the method of regularized stokeslets. *IEEE Transactions on Control Systems Technology*, 17(4):907–916.
- Lopez-Sanchez, J., Miribel-Catala, P., Montane, E., Puig-Vidal, M., Bota, S., Samitier, J., Simu, U., and Johansson, S. (2001). High accuracy piezoelectric-based microrobot for biomedical applications. In *ETFA 2001. 8th International Conference on Emerging Technologies and Factory Automation. Proceedings (Cat. No.01TH8597)*, volume 2, pages 603–609. IEEE.
- Ludwig, W. (1930). Zur Theorie der Flimmerbewegung (Dynamik, Nutzeffekt, Energiebilanz). *Zeitschrift für Vergleichende Physiologie*, 13(3):397–504.
- Machin, B. Y. K. E., Modes, T. H. E., Wave, O. F., Along, P., and Machin, K. E. (1958). Wave propagation along flagella. *The Journal of experimental biology*, 35(May):796–806.
- Macnab, R. M. (1977). Bacterial flagella rotating in bundles: a study in helical geometry. *Proceedings of the National Academy of Sciences of the United States of America*, 74(1):221–225.
- Maniyeri, R. and Kang, S. (2012). Numerical study on the rotation of an elastic rod in a viscous fluid using an immersed boundary method. *Journal of Mechanical Science and Technology*, 26(5):1515–1522.
- Maniyeri, R., Kweon, Y., Kang, S., Jun, M., Suh, Y. K., Kang, S., and Kim, M. J. (2012). Numerical study on the propulsion of a bacterial flagellum in a viscous fluid using an immersed boundary method. *Computers and Fluids*, 62:13–24.
- Mathieu, J.-b. B., Beaudoin, G., and Martel, S. (2006). Method of propulsion of a ferromagnetic core in the cardiovascular system through magnetic gradients generated by an MRI system. *IEEE Transactions on Biomedical Engineering*, 53(2):292–299.
- Maude, a. D. (1963). Non-Random Distribution of Bull Spermatozoa in a Drop of Sperm Suspension. *Nature*, 200:381.
- Mayne, R., Whiting, J. G., Wheway, G., Melhuish, C., and Adamatzky, A. (2017). Particle sorting by Paramecium cilia arrays. *BioSystems*, 156-157:46–52.
- McMillen, T. and Holmes, P. (2006). An elastic rod model for anguilliform swimming. *Journal of Mathematical Biology*, 53(5):843–886.
- Menciassi, A., Valdastrì, P., Harada, K., and Dario, P. (2011). Single and Multiple Robotic Capsules for Endoluminal Diagnosis and Surgery. In *Surgical Robotics*, pages 313–354. Springer US, Boston, MA.
- Mettot, C. and Lauga, E. (2011). Energetics of synchronized states in three-dimensional beating flagella. *Physical Review E - Statistical, Nonlinear, and Soft Matter Physics*, 84(6):1–14.

- Michelin, S. and Lauga, E. (2010). The long-time dynamics of two hydrodynamically-coupled swimming cells. *Bulletin of Mathematical Biology*, 72(4):973–1005.
- Michelin, S. and Lauga, E. (2011). Optimal feeding is optimal swimming for all Péclet numbers. *Physics of Fluids*, 23(10):101901.
- Microbiology, R., Thormann, K. M., and Paulick, A. (2010). Tuning the flagellar motor. *Microbiology*, 156(5):1275–1283.
- Montenegro-Johnson, T. D., Gagnon, D. A., Arratia, P. E., and Lauga, E. (2016). Flow analysis of the low Reynolds number swimmer *C. elegans*. *Physical Review Fluids*, 1(5):053202.
- Morandotti, M. (2012). Self-propelled micro-swimmers in a Brinkman fluid. *Journal of Biological Dynamics*, 6(sup1):88–103.
- Muldowney, G. P. and Higdon, J. J. L. (1995). A spectral boundary element approach to three-dimensional Stokes flow. *Journal of Fluid Mechanics*, 298(-1):167.
- Najafi, A. and Golestanian, R. (2004). Simple swimmer at low Reynolds number: Three linked spheres. *Physical Review E - Statistical, Nonlinear, and Soft Matter Physics*, 69(6 1):1–4.
- Nelson, B. J., Kaliakatsos, I. K., and Abbott, J. J. (2010). Microrobots for minimally invasive medicine. *Annual review of biomedical engineering*, 12(April):55–85.
- Niedermayer, T., Eckhardt, B., and Lenz, P. (2008). Synchronization, phase locking, and metachronal wave formation in ciliary chains. *Chaos*, 18(3):037128.
- Nourmohammadi, H. and Keighobadi, J. (2014). *Design, modelling and control of a manoeuvrable swimming micro-robot*, volume 19. IFAC.
- O’Malley, S. and Bees, M. a. (2012). The Orientation of Swimming Biflagellates in Shear Flows. *Bulletin of Mathematical Biology*, 74(1):232–255.
- Ogrin, F. Y., Petrov, P. G., and Winlove, C. P. (2008). Ferromagnetic microswimmers. *Physical Review Letters*, 100(21):1–4.
- Okada, T., Guo, S., Member, S., and Yamauchi, Y. (2011). A wireless microrobot with 3 DOFs in pipe for medical applications. In *2011 IEEE/ICME International Conference on Complex Medical Engineering, CME 2011*, pages 79–84. IEEE.
- Olson, S. D., Lim, S., and Cortez, R. (2013). Modeling the dynamics of an elastic rod with intrinsic curvature and twist using a regularized Stokes formulation. *Journal of Computational Physics*, 238:169–187.
- Olson, S. D., Suarez, S. S., and Fauci, L. J. (2011). Coupling biochemistry and hydrodynamics captures hyperactivated sperm motility in a simple flagellar model. *Journal of Theoretical Biology*, 283(1):203–216.
- Or, Y. and Murray, R. M. (2009). Dynamics and stability of a class of low Reynolds number swimmers near a wall. *Physical Review E - Statistical, Nonlinear, and Soft Matter Physics*, 79(4):45302.

- Or, Y., Zhang, S., and Murray, R. M. (2011). Dynamics and Stability of Low-Reynolds-Number Swimming Near a Wall. *SIAM Journal on Applied Dynamical Systems*, 10(3):1013–1041.
- Özkale, B., Parreira, R., Bekdemir, A., Pancaldi, L., Özelçi, E., Amadio, C., Kaynak, M., Stellacci, F., Mooney, D. J., and Sakar, M. S. (2019). Modular soft robotic microdevices for dexterous biomanipulation. *Lab on a Chip*, 19(5):778–788.
- Pak, O. S. and Lauga, E. (2009). The transient swimming of a waving sheet. *Proceedings of the Royal Society A: Mathematical, Physical and Engineering Sciences*, 466(2113):107–126.
- Park, C., Hall, G., Angeles, L., Two, D. P., Hall, S., and Hill, C. (2007). Challenges in Image-Guided Therapy System Design. *NeuroImage*, 37:1–28.
- Parker, G. H. (1911). The mechanism of locomotion in gastropods. *Journal of Morphology*, 22(1):155–170.
- Pawashe, C., Floyd, S., and Sitti, M. (2008). Dynamic modeling of stick slip motion in an untethered magnetic microrobot. *Robotics: Science and Systems*.
- Pawashe, C., Floyd, S., and Sitti, M. (2013). Multiple magnetic microrobot control using electrostatic anchoring Multiple magnetic microrobot control using electrostatic anchoring. *Applied Physics Letters*, 164108(2009):1–4.
- Pedley, T. (1992). Hydrodynamic Phenomena In Suspensions Of Swimming Microorganisms. *Annual Review of Fluid Mechanics*, 24(1):313–358.
- Peskin, C. S. (1972). Flow patterns around heart valves: A numerical method. *Journal of Computational Physics*, 10(2):252–271.
- Peskin, C. S. (1977). Numerical analysis of blood flow in the heart. *J. Comp. Phys.*, 25:220.
- Peskin, C. S. (2002). The immersed boundary method. *Acta Numer.*, 11:479–517.
- Petter, H., Mardal, L. K.-a., Winther, R., Langtangen, H. P., Mardal, K.-A., and Winther, R. (2002). Numerical methods for incompressible viscous flow. *Advances in Water Resources*, 25(8-12):1125–1146.
- Peyer, K. E., Tottori, S., Qiu, F., Zhang, L., and Nelson, B. J. (2013). Magnetic helical micromachines. *Chemistry - A European Journal*, 19(1):28–38.
- Phan-Thien, N., Tran-Cong, T., and Ramia, M. (1987). A boundary-element analysis of flagellar propulsion. *Journal of Fluid Mechanics*, 184(-1):533.
- Phuyal, K. and Kim, M. J. (2013). Mechanics of swimming of multi-body bacterial swimmers using non-labeled cell tracking algorithm. *Physics of Fluids*, 25(1).
- Pickl, K., Götz, J., Iglberger, K., Pande, J., Mecke, K., Smith, A. S., and Rüde, U. (2012). All good things come in threes-Three beads learn to swim with lattice Boltzmann and a rigid body solver. *Journal of Computational Science*, 3(5):374–387.
- Polin, M., Tuval, I., Drescher, K., Gollub, J. P., and Goldstein, R. E. (2009). Chlamydomonas swims with two "gears" in a eukaryotic version of run-and-tumble locomotion. *Science (New York, N.Y.)*, 325(5939):487–490.

- Pooley, C. M., Alexander, G. P., and Yeomans, J. M. (2007). Hydrodynamic interaction between two swimmers at low Reynolds number. *Physical Review Letters*, 99(22):228103–.
- Powers, T. R. (2002). Role of body rotation in bacterial flagellar bundling. *Physical Review E - Statistical, Nonlinear, and Soft Matter Physics*, 65(4):3–6.
- Pozrikidis, C. (2011). Introduction to Theoretical and Computational Fluid Dynamics [Hardcover]. *Physics Today*, page 1296.
- Purcell, E. M. (1977). Life at low Reynolds number. *American Journal of Physics*, 45(1):3–11.
- Purcell, E. M. (1997). The efficiency of propulsion by a rotating flagellum. *Proceedings of the National Academy of Sciences*, 94(21):11307–11311.
- Qiu, T., Lee, T. C., Mark, A. G., Morozov, K. I., Münster, R., Mierka, O., Turek, S., Leshansky, A. M., and Fischer, P. (2014). Swimming by reciprocal motion at low Reynolds number. *Nature Communications*, 5(May):1–8.
- Rediniotis, O. K., Lagoudas, D. C., Mashio, T., Garner, L. J., and Qidwai, M. A. (1997). Theoretical and experimental investigations of an active hydrofoil with SMA actuators. pages 277–289.
- Riedel, I. H., Kruse, K., and Howard, J. (2005). A self-organized vortex array of hydrodynamically entrained sperm cells. *Science (New York, N.Y.)*, 309(5732):300–303.
- Rodenborn, B., Chen, C.-H., Swinney, H. L., Liu, B., and Zhang, H. P. (2013). Propulsion of microorganisms by a helical flagellum. *Proceedings of the National Academy of Sciences of the United States of America*, 110(5):E338–47.
- Roggo, C. and van der Meer, J. R. (2017). Miniaturized and integrated whole cell living bacterial sensors in field applicable autonomous devices. *Current Opinion in Biotechnology*, 45:24–33.
- Roper, M., Dreyfus, R., Baudry, J., Fermigier, M., Bibette, J., and Stone, H. a. (2008). Do magnetic micro-swimmers move like eukaryotic cells? *Proceedings of the Royal Society A: Mathematical, Physical and Engineering Sciences*, 464(2092):877–904.
- Rosen, J., Hannaford, B., and Satava, R. M. (2011). Surgical robotics: Systems applications and visions. In Rosen, J., Hannaford, B., and Satava, R. M., editors, *Surgical Robotics: Systems Applications and Visions*, pages 1–819. Springer US, Boston, MA.
- Saffman, P. G. (1956). On the motion of small spheroidal particles in a viscous liquid. *Journal of Fluid Mechanics*, 1(05):540.
- Saintillan, D. and Shelley, M. J. (2007). Orientational order and instabilities in suspensions of self-locomoting rods. *Physical Review Letters*, 99(5):1–4.
- Saintillan, D. and Shelley, M. J. (2008). Hydrodynamic fluctuations and instabilities in ordered suspensions of self-propelled particles. *Physics of Fluids*, 20(12):123304.
- Sareh, S., Conn, a. T., Rossiter, J. M., Ieropoulos, I., and Walters, P. (2010). <title>Optimization of bio-inspired multi-segment IPMC cilia</title>. In Bar-Cohen, Y., editor, *Proc. SPIE 7642, Electroactive Polymer Actuators and Devices (EAPAD)*, volume 7642, pages 76421S–76421S–11.

- Sayar, E. and Farouk, B. (2011). Multifield Analysis Of A Piezoelectric Valveless Micropump. In *IMECE2011-65021*, pages 1–9.
- Schuster, S. C. and Khan, S. (1994). The bacterial flagellar motor. *Annual review of biophysics and biomolecular structure*, 23:509–539.
- Shi, L., Guo, S., Mao, S., Yue, C., Li, M., and Asaka, K. (2013). Development of an amphibious turtle-inspired spherical mother robot. *Journal of Bionic Engineering*, 10(4):446–455.
- Sleigh, M. a., Blake, J. R., and Liron, N. (1988). The propulsion of mucus by cilia. *The American review of respiratory disease*, 137(3):726–741.
- Smith, D. J. (2010). A boundary element regularised Stokeslet method applied to cilia and flagella-driven flow. *Proceedings of the Royal Society A: Mathematical, Physical and Engineering Sciences*, 465(2112):20.
- Sokolov, I. L., Cherkasov, V. R., Tregubov, A. A., Buiuclic, S. R., and Nikitin, M. P. (2017). Smart materials on the way to theranostic nanorobots: Molecular machines and nanomotors, advanced biosensors, and intelligent vehicles for drug delivery. *Biochimica et Biophysica Acta - General Subjects*, 1861(6):1530–1544.
- Spagnolie, S. E. and Lauga, E. (2011). Comparative hydrodynamics of bacterial polymorphism. *Physical Review Letters*, 106(5).
- Spagnolie, S. E. and Lauga, E. (2012). Hydrodynamics of self-propulsion near a boundary: predictions and accuracy of far-field approximations. *Journal of Fluid Mechanics*, 700:105–147.
- Suzumori, K., Endo, S., Kanda, T., Kato, N., and Suzuki, H. (2007). A Bending Pneumatic Rubber Actuator Realizing Soft-bodied Manta Swimming Robot. In *Proceedings 2007 IEEE International Conference on Robotics and Automation*, number April, pages 4975–4980. IEEE.
- Swan, J. W., Brady, J. F., Moore, R. S., Dooling, L., Hoh, N., Choi, J., and Zia, R. (2011). Modeling hydrodynamic self-propulsion with Stokesian Dynamics. Or teaching Stokesian Dynamics to swim. *Physics of Fluids*, 23(7):071901.
- Swee-Leong, K., Mohamad, N., David Fook Weng, Y., Soo Kien, C., and Chang Fu, D. (2011). Multi-frequency energy harvesting using thick-film piezoelectric cantilever. In *International Conference on Electrical, Control and Computer Engineering 2011 (InECCE)*, number 2, pages 420–423. IEEE.
- Tabak, A. F. and Yesilyurt, S. (2014). Computationally-validated surrogate models for optimal geometric design of bio-inspired swimming robots: HELICAL swimmers. *Computers and Fluids*, 99:190–198.
- Taheri, A., Mohammadi-amin, M., and Moosavy, S. H. S. (2009). A Numerical Strategy to Design Maneuverable Micro-Biomedical Swimming Robots Based on Biomimetic Flagellar Propulsion. *Akademik.Unsri.Ac.Id*, pages 500–504.
- Tam, D. and Hosoi, a. E. (2007). Optimal Stroke patterns for Purcell’s three-link swimmer. *Physical Review Letters*, 98(6).

- Tanaka, Y. and Fujita, H. (2015). Fluid driving system for a micropump by differentiating iPS cells into cardiomyocytes on a tent-like structure. *Sensors and Actuators, B: Chemical*, 210:267–272.
- Taylor, G. (1951). Analysis of the swimming of microscopic organisms. *Proceedings of the Royal Society of London. Series A. Mathematical and Physical Sciences*, 209(1099):447–461.
- Taylor, G. (1969). Motion of axisymmetric bodies in viscous fluids. In *Problems of Hydrodynamics and Continuum Mechanics*, pages 718–724.
- Terzopoulou, A., Hoop, M., Chen, X.-Z., Hirt, A. M., Charilaou, M., Shen, Y., Mushtaq, F., del Pino, A. P., Logofatu, C., Simonelli, L., de Mello, A. J., Doonan, C. J., Sort, J., Nelson, B. J., Pané, S., and Puigmartí-Luis, J. (2019). Mineralization-Inspired Synthesis of Magnetic Zeolitic Imidazole Framework Composites. *Angewandte Chemie International Edition*, 58(38):13550–13555.
- Thaokar, R. M. (2008). Hydrodynamic interaction between two rotating tori. *European Physical Journal B*, 61(1):47–58.
- Tillett, J. P. K. (1970). Axial and transverse Stokes flow past slender axisymmetric bodies. *Journal of Fluid Mechanics*, 44(03):401.
- Tottori, S. and Nelson, B. J. (2018). Controlled Propulsion of Two-Dimensional Microswimmers in a Precessing Magnetic Field. *Small*, 14(24):1800722.
- Tran-Cong, T. and Phan-Thien, N. (1986). Boundary element solution for half-space elasticity or stokes problem with a no-slip boundary. *Computational Mechanics*, 1(4):259–268.
- Tran-Cong, T. and Phan-Thien, N. (1988). Three-dimensional study of extrusion processes by Boundary Element Method. - II. Extrusion of a viscoelastic fluid. *Rheologica Acta*, 27(6):639–648.
- Tran-Cong, T., Zheng, R., and Phan-Thien, N. (1990). Boundary element method for finite elasticity. *Computational Mechanics*, 6(3):205–219.
- Tuck, E. O. (1964). Some methods for flows past blunt slender bodies. *Journal of Fluid Mechanics*, 18(04):619.
- Turner, L., Ryu, W. S., and Berg, H. C. (2000). Real-time imaging of fluorescent flagellar filaments. *Journal of Bacteriology*, 182(10):2793–2801.
- Ullrich, F., Lussi, J., Chatzopoulos, V., Michels, S., Petruska, A. J., and Nelson, B. J. (2018). A Robotic Diathermy System for Automated Capsulotomy. *Journal of Medical Robotics Research*, 03(01):1850001.
- Vaccari, L., Molaei, M., Niepa, T. H., Lee, D., Leheny, R. L., and Stebe, K. J. (2017). Films of bacteria at interfaces. *Advances in Colloid and Interface Science*, 247(July):561–572.
- Wang, Z., Hang, G., Li, J., Wang, Y., and Xiao, K. (2008). A micro-robot fish with embedded SMA wire actuated flexible biomimetic fin. *Sensors and Actuators, A: Physical*, 144(2):354–360.
- Waters, C. M. (2013). Bacterial wheel locks: Extracellular polysaccharide inhibits flagellar rotation. *Journal of Bacteriology*, 195(3):409–410.

- Webb, G., Wilson, L., Lagoudas, D., and Rediniotis, O. (2000). Adaptive Control of Shape Memory Alloy Actuators for Underwater Biomimetic Applications. *AIAA Journal*, 38(2):325–334.
- Williams, B. J., Anand, S. V., Rajagopalan, J., and Saif, M. T. A. (2014). A self-propelled biohybrid swimmer at low Reynolds number. *Nature communications*, 5:3081.
- Winet, H., Bernstein, G. S., and Head, J. (1984). Observations on the response of human spermatozoa to gravity, boundaries and fluid shear. *Journal of reproduction and fertility*, 70(2):511–523.
- Wu, T. Y. (1977). Hydrodynamics of swimming at low Reynolds numbers. *Fortschritte der Zoologie*, 24(2-3):149–169.
- Wu, T. Y.-T. (1961). Swimming of a waving plate. *Journal of Fluid Mechanics*, 10(03):321.
- Yang, C., Chen, C., Ma, Q., Wu, L., and Song, T. (2012). Dynamic Model and Motion Mechanism of Magnetotactic Bacteria with Two Lateral Flagellar Bundles. *Journal of Bionic Engineering*, 9(2):200–210.
- Yang, X., Wang, T., Liang, J., Yao, G., and Liu, M. (2015). Survey on the novel hybrid aquatic-aerial amphibious aircraft: Aquatic unmanned aerial vehicle (AquaUAV). *Progress in Aerospace Sciences*, 74:131–151.
- Yang, Y., Elgeti, J., and Gompper, G. (2008). Cooperation of sperm in two dimensions: Synchronization, attraction, and aggregation through hydrodynamic interactions. *Physical Review E - Statistical, Nonlinear, and Soft Matter Physics*, 78(6):061903.
- Yates, G. T. (1986). How Microorganisms Move through Water: The hydrodynamics of ciliary and flagellar propulsion reveal how microorganisms overcome the extreme effect of the viscosity of water. *American Scientist*, 74(4):358–365.
- Ye, X. F., Su, Y. D., and Guo, S. X. (2009). An IPMC Actuated 3D Swimming Microrobot and its Propulsive Efficiency Analysis. *Key Engineering Materials*, 419-420:785–788.
- Youngren, G. K. and Acrivos, a. (1975). Stokes flow past a particle of arbitrary shape: a numerical method of solution. *Journal of Fluid Mechanics*, 69(02):377.
- Yu, T. S., Lauga, E., and Hosoi, a. E. (2006). Experimental investigations of elastic tail propulsion at low Reynolds number. *Physics of Fluids*, 18(9):91701.
- Zargar, R., Najafi, A., and Miri, M. (2009). Three-sphere low-Reynolds-number swimmer near a wall. *Physical Review E - Statistical, Nonlinear, and Soft Matter Physics*, 80(2):26308.
- Zhang, L., Abbott, J. J., Dong, L., Kratochvil, B. E., Bell, D., and Nelson, B. J. (2009a). Artificial bacterial flagella: Fabrication and magnetic control. *Applied Physics Letters*, 94(6):064107.
- Zhang, L., Abbott, J. J., Dong, L., Peyer, K. E., Kratochvil, B. E., Zhang, H., Bergeles, C., and Nelson, B. J. (2009b). Characterizing the swimming properties of artificial bacterial flagella. *Nano Letters*, 9(10):3663–3667.
- Zhang, L., Petit, T., Lu, Y., Kratochvil, B. E., Peyer, K. E., Pei, R., Lou, J., and Nelson, B. J. (2010). Controlled propulsion and cargo transport of rotating nickel nanowires near a patterned solid surface. *ACS Nano*, 4(10):6228–6234.

-
- Zhang, Y., Yue, M., Guo, D., Wang, D., Yu, H., Jiang, S., and Zhang, X. (2009c). Characteristics of spatial magnetic torque of an intestine capsule micro robot with a variable diameter.

Appendix A

Physical properties of prototype's material

A.1 DSM Somos Resin Properties

Durable, opaque, white, translucent waterproof resin. Suitable for (355nm) SLA solid laser molding systems description

A.1.1 Description

DSM Somos Resin is a low viscosity liquid photosensitive resin that can be used to make rugged, hard and waterproof functional parts. Parts made with Somos 14120 resin material are opaque white, similar to engineering plastics. application

A.1.2 Applications

The Somos resin material provides performance similar to traditional engineering plastics, including ABS and PBT. It can be ideally applied to sample production of automotive, medical devices and consumer electronics products as well as water flow analysis, RTV models, durable concept models, duct testing and rapid casting models.

The physical properties of DSM Somos is show in table Tab. [A.1](#).

The mechanical properties of DSM Somos is show in table Tab. [A.2](#)

Table A.1 Physical properties of DSM Somos

Name	Value
Appearance:	Opaque white, translucent
Viscosity:	~260cps (25°C)
Density:	~1.12g/cm ³ (25°C)

Table A.2 Mechanical Properties of DSM Somos

Name	Value
Tensile Strength:	45~54MPa
Breaking Elongation:	11~20%
Tensile Elongation at Yield Point:	3~5%
elasticity modulus:	2500~3000MPa
bending strength:	60~75MPa
bending modulus:	1900~2500MPa
specific water absorption:	0.35%
glass state temperature:	39~50°C
Heat Deflection Temperature:	46~60°C